Beyond Axisymmetry in Tokamak Plasmas

Michail-Savvas ANASTOPOULOS-TZANIS

DOCTOR OF PHILOSOPHY

UNIVERSITY OF YORK

PHYSICS

September 2019

UNIVERSITY OF YORK

Abstract

Physics

PhD on Plasma Science & Fusion Energy

Beyond Axisymmetry in Tokamak Plasmas

by Michail-Savvas ANASTOPOULOS-TZANIS

H-mode tokamak plasmas are characterised by quasi-periodic instabilities, called edge localised modes (ELMs), driven by unstable peeling-ballooning modes inside the pedestal region. For large scale tokamaks, like ITER, the resulting particle and heat fluxes are predicted to be unacceptable and ELM control methods are required. One promising method relies on the application of 3D resonant magnetic perturbations (MPs), where typically $B_N/B_0 \sim 10^{-3}$, and ELM mitigation or even complete suppression is observed. A computational framework is presented that aims to understand the effect of MPs on both plasma equilibria and stability. The ELITE stability code is used to find the linearised plasma response, i.e. the 3D part of the equilibrium, and compute the axisymmetric peeling-ballooning eigenmodes. This information is used to calculate the 3D stability under a perturbative and a variational formulation of the MHD energy principle. In practice, the axisymmetric peeling-ballooning modes are used as trial functions for the minimisation of the 3D energy functional. The symmetry breaking of the toroidal geometry leads to the coupling of toroidal modes which has a direct impact on the linear growth rates of unstable peeling-ballooning modes. This mechanism results in the modification of the plasma stability above a critical value of the applied MP field and field-line localisation of the peeling-ballooning eigenmode. It is observed that intermediate to high n ballooning modes are in general destabilised by the applied MP field, while external peeling-ballooning modes reorganise to an internal ballooning structure. In addition, extrema in the growth rate spectrum, due to low n kink modes, are observed to be strongly destabilised as predicted by perturbation theory. This work provides proof of principle examination of the 3D peeling-ballooning instability as well as a framework for the optimisation of MP coil configuration.

Contents

List of Tables

List of Figures

Acknowledgements

I would like to thank my PhD supervisors Dr. Christopher Ham and Prof. Howard Wilson for the realisation of this project.

I am grateful to Prof. Howard Wilson for introducing me to the ELITE ideal MHD stability code. He provided constant support and information regarding the operation of ELITE, as well as helpful discussions regarding physics, allowing the faster progress and realisation of this project. I am thankful to Dr. Christopher Ham for the fruitful discussions regarding the obtained results and physics, together with his insight regarding the progress and goals of this project. Both of them were a constant source of enthusiasm and inspiration, encouraging me to further expand my knowledge. Moreover, I would like to express my gratitude to Prof. C.C Hegna for allowing me to visit the University of Madison-Wisconsin and collaborate with him for two months, providing me with knowledge on numerical techniques and plasma physics. Finally, I would like to thank Dr. Ben Dudson for his support with the operation of BOUT++ as well as Dr. David Ryan and Dr. Samuli Saarelma for their contribution in the benchmark study between ELITE and MARS.

Last but not least, I am thankful to my family for their constant support throughout my education career, without whom the completion of my degrees would be impossible. Furthermore, I would like to thank my friends and PhD colleagues Laszlo Horvath and Siobhan Smith for their company and support in this PhD journey. Finally, I would like to thank my friends Skye, Giovani, Manu, Juan, Paul, Michele, Cindy and Merry for welcoming me in Oxford and sharing together happy memories.

Declaration of Authorship

I declare that this thesis is a presentation of original work and I am the sole author. This work has not previously been presented for an award at this, or any other, University. All sources are acknowledged as References.

I declare that this work is my own except where indicated by appropriate citation and with the exceptions given below:

- Where I have consulted the published work of others, this is always clearly attributed.
- Where I have quoted from the work of others, the source is always given. With the exception of such quotations, this thesis is entirely my own work.
- The 3D magnetic field using ERGOS for a MAST geometry in Chapter 4 was provided by Dr C.J. Ham.
- The model plasma equilibria used in Chapter 4 were provided by Dr P.B. Snyder.
- The AUG plasma equilibrium and plasma response using MARS in Chapter 4 was provided by Dr D. Ryan and S. Saarelma.
- I have acknowledged all main sources of help.

The research presented in this thesis is published or currently being written up in preparation to submit it to the following journals:

- Part of the research presented in Chapters 3 and 4 is published in Nuclear Fusion, titled "Non-Axisymmetric Equilibrium and Stability using the ELITE Stability Code", and can be found in https://doi.org/10.1088/1741-4326/ab40ef.
- Part of the research presented in Chapters 3 and 4 is being prepared for journal publication.

Additionally, this research has been presented at the following conferences:

- Part of the research in Chapters 3 and 4 was presented as a poster at the European Fusion Theory Conference 2017.
- Part of the research in Chapters 3 and 4 was presented as a poster at the KSTAR Conference 2018.
- Part of the research in Chapters 3 and 4 was presented as a poster at the European Physical Society Plasma Physics Conference 2018 and 2019.
- Part of the research in Chapter 3 and 4 was presented as an oral at the Institute of Physics Plasma Physics Conference 2019.

Chapter 1

Introduction

1.1 Fusion Energy

There is worldwide demand for a modern lifestyle, specifically from people in developing countries, as well as a rapid population growth that means increased energy consumption. Therefore, it is imperative that energy production methods continuously improve their efficiency. According to Fig.1.1 the vast majority of energy from 1971 to 2015 was supplied by fossil fuels (coal,

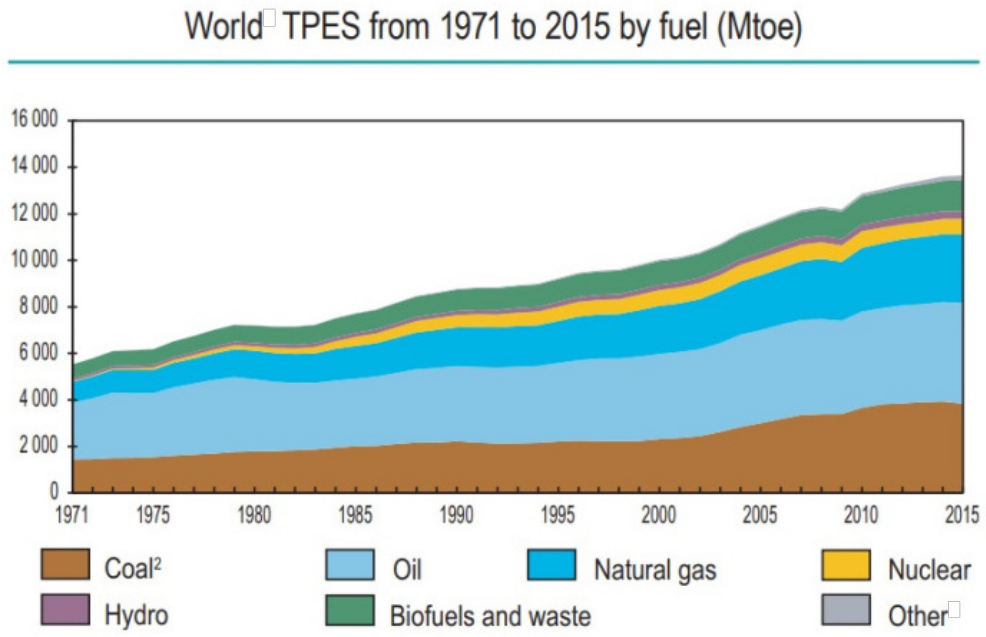

FIGURE 1.1: World total primary energy by fuel from 1971 and 2015 measured in million tonnes of oil equivalent (Mtoe). [1]

gas and oil). However, fossil fuels are responsible for serious environmental pollution and greenhouse effects [2]. There is growing awareness among the general public of climate change and the importance of finding new low carbon energy sources. In addition, studies on the amount of available resources suggest that fossil fuels will be depleted in the end of the century [3]. Currently, alternative sources of energy (nuclear and renewable sources) have a minor contribution to the global energy production process. Renewable sources of energy are somewhat unreliable, i.e. wind does not blow or sun does not shine, unless significant technological progress is made with respect to power storage. In addition, due to geographical limitations certain sources are not available and their efficiency still depends on uncontrollable phenomena. As a result, other sources of energy have to be addressed to resolve an upcoming energy crisis.

Nuclear power is a candidate for the solution of the problem. Over the last 70 years, nuclear reactors have operated using the decay of enriched uranium to lighter and more stable elements. This process is called fission, it is an exothermic process and involves the splitting of a heavy nucleus into two lighter elements of higher binding energy. Unfortunately, fission power plants hide many hazards as the fuel is intrinsically radioactive. Errors in the operation can potentially result in radiation leakage that has severe consequences for the environment and the nearby population. In addition, the

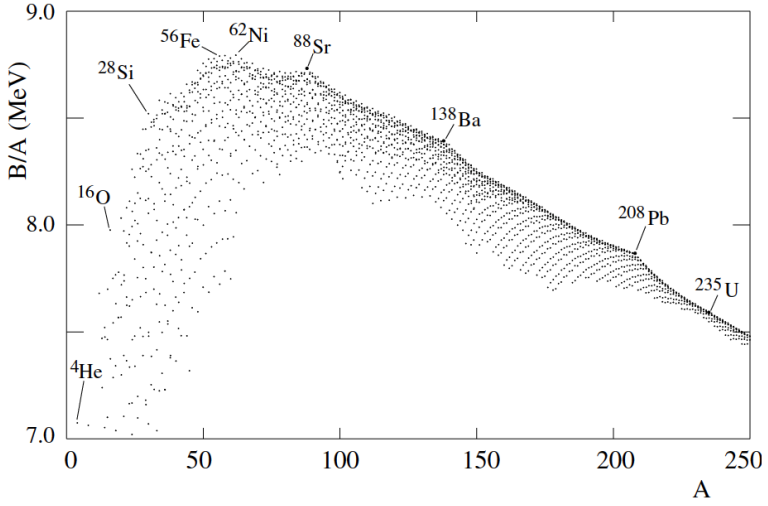

FIGURE 1.2: Binding energy per nucleon B/A MeV as a function of total nucleon number A. [4]

reactor produces long-lived nuclear wastes ($\mathcal{O}(10^4)$ years) that have to be stored and disposed off in some way.

An alternative nuclear process is fusion. For similar reasons to fission, fusion is an exothermic process as well, but involves the combination of two light nuclei into a single heavier nucleus of higher binding energy. The dependence of the binding energy on the total number of nucleons is illustrated in Fig.1.2. Iron, ^{56}Fe, has the maximum binding energy, so moving uphill from the left or the right results in energy release. If two light nuclei come close enough, such that nuclear forces become dominant, fusion will occur. Although, it cannot happen spontaneously like fission, due to the Coulomb repulsion of the nucleons. A way to overcome this Coulomb barrier is to heat the fuel to the point where the thermal speed of some of the particles can overcome the barrier.

The candidate reactions involve hydrogen isotopes. The most promising in terms of required temperature and energy release is the D-T reaction between deuterium ^2D and tritium ^3T at temperature $T \sim 100$ keV as can be seen from Fig.1.3. Deuterium is abundant in nature as it consists 0.0153% of seawater. On the other hand, very little tritium exists because it has a half life of 12.5 years and it is not naturally produced in bulk quantities. It can be bred from lithium via neutron capture and again lithium is very abundant in soil and oceans (natural lithium consists of 7.5% ^6Li and 92.5% ^7Li).

$$^2D +^3 T \rightarrow \ ^4He + n + 17.6 \text{ MeV} \tag{1.1}$$

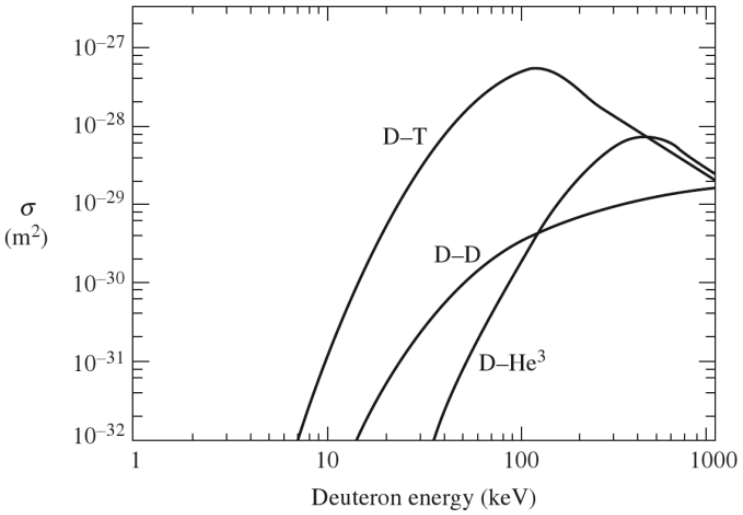

FIGURE 1.3: Reaction rate for the different isotope reactions of hydrogen. [5]

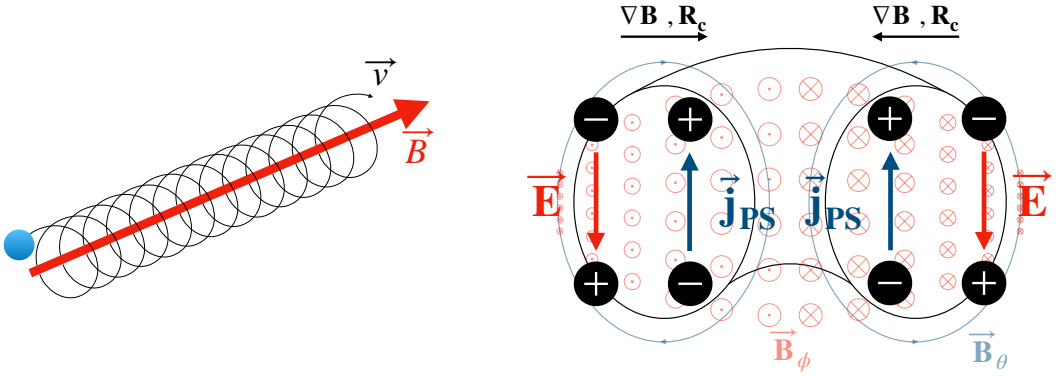

(A) (B)

FIGURE 1.4: Schematic of (A) a particle moving in a uniform magnetic field and (B) electromagnetic fields produced in a toroidal magnetic chamber.

$$^{6}Li + n \rightarrow ^{3}T + ^{4}He + 4.8\,\text{MeV} \tag{1.2a}$$

$$^{7}Li + n \rightarrow ^{3}T + ^{4}He + n - 2.5\,\text{MeV} \tag{1.2b}$$

Temperature of $T \sim 30$ keV is sufficient to produce a significant fusion rate in a macroscopic scale due to quantum tunnelling effects. At such temperatures matter is fully ionised in a plasma state and is susceptible to electromagnetic fields.

1.2 Magnetic Confined Fusion

The dominant mechanism proposed for the realisation of fusion is magnetic confinement of the plasma using helical magnetic fields. Magnetic confinement of charged particles stems from the intrinsic property of the magnetic field to restrict particle motion perpendicular to its field line as illustrated in Fig.1.4a. The toroidal magnetic field $\boldsymbol{B}_t$ is beneficial since the periodic geometry prohibits particle end losses. However, the existence of magnetic inhomogeneity $\nabla \boldsymbol{B}$ and curvature $\boldsymbol{R}_c$ due to the toroidal geometry, leads to charge separation and creation of an electric field $\boldsymbol{E}$ that drifts particles outwards from the torus, as depicted in Fig.1.4b. In particular, any force $\boldsymbol{F}$ leads to drift motion perpendicular to the magnetic field $\boldsymbol{B}$, such that $\boldsymbol{v}_d = (\boldsymbol{F} \times \boldsymbol{B})/(eB^2)$. Since $\boldsymbol{F}_{\nabla \boldsymbol{B}} = \nabla B K_{\perp}/B$ and $\boldsymbol{F}_{\boldsymbol{R}_c} = 2\nabla B K_{||}/B$ are independent of charge, where $K_{\perp} = mv_{\perp}^2/2$ and $K_{||} = mv_{||}^2/2$, positive and negative charges

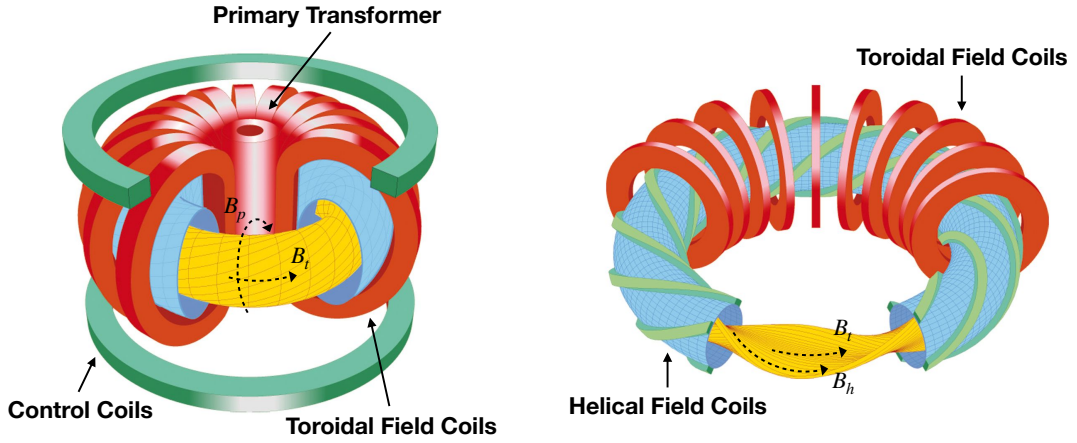

(A) (B)

FIGURE 1.5: Schematic of (A) tokamak configuration and (B) stellarator configuration.

drift in opposite directions and as a result an electric field $\boldsymbol{E}$ is established. This electric field leads to an additional force $\boldsymbol{F_E} = e\boldsymbol{E}$ that depends on charge and so the $\boldsymbol{E} \times \boldsymbol{B}$ drift motion is in the same radially outward direction for both positive and negative charges. Those drifts can be fully compensated by the introduction of a poloidal magnetic field $\boldsymbol{B}_p$ that on average cancels the charge separation. In such a way particles are restricted to move along nested toroidal flux surfaces that prohibit cross-field transport.

A tokamak is a reactor that provides such a magnetic configuration as illustrated by Fig.1.5a. The toroidal field is produced via poloidal current carrying coils and the plasma current is inductively driven by an increasing voltage in a primary transformer, where the plasma serves as the secondary transformer. As the voltage cannot increase indefinitely the tokamak operates in a pulsed mode. Although, non-inductive current drive is possible either due to the establishment of a steep pressure gradient or using for example neutral beams or radio-frequency waves, allowing steady state operation. An alternative to the tokamak is called the stellarator, where the helical magnetic field is provided by carefully shaped current coils removing the limitation of pulsed operation as depicted in Fig.1.5b. However, the tokamak is the most developed concept.

In a tokamak, the temperature inside the plasma is raised initially by ohmic heating from the plasma current induced by the primary winding up to $T \sim 1$ KeV. Additional heating by particle-beams or electromagnetic waves can raise

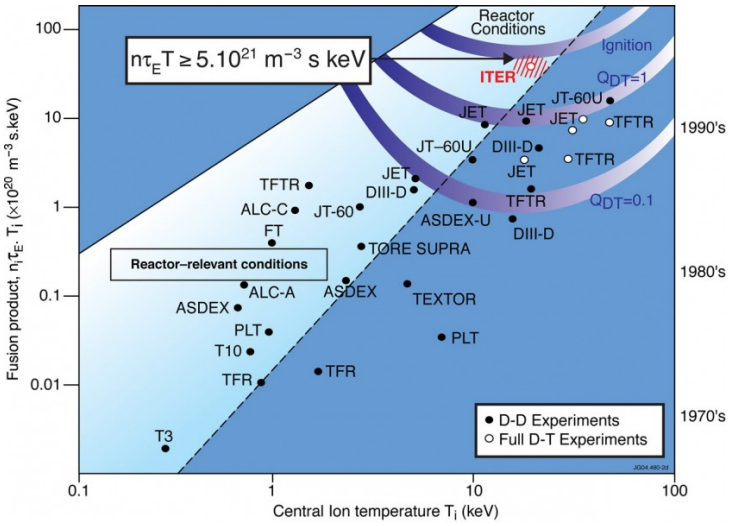

FIGURE 1.6: Fusion triple product $n\tau_E T$ as a function of temperature T from different tokamaks for the period 1985-1997 for D-D (black dots) and D-T (white dots) experiments. [8]

the plasma temperature to sufficiently high levels. In addition, the DT fusion process itself contributes to plasma heating. The α-particle He^4 is released with an energy $E_\alpha \approx 3.5$ MeV. This energy is transferred to the plasma as α-particle heating via collisions and could even sustain the DT reaction. Taking into account the power balance of the system, a burning or self-sustaining plasma is such that the α-particle heating power P_α balances the power losses P_L due to radiation and transport. The Lawson criterion [6] defines a relation between the energy confinement time $\tau_E = W/P_L$ in steady state, where W is the stored thermal energy, the plasma density n and temperature T required to achieve burning plasma conditions and Fig.1.6 illustrates the historical development of tokamak performance. In the 1980s two large tokamaks TFTR and JET reached $T \sim 30$ keV for a plasma current I = 3 MA and confinement time of about a second [5]. The highest efficiency of $Q = P_\alpha/P_{in} = 0.62$ for D-T reactions was obtained at JET in 1999 [7].

Clearly for power plant scales, tokamaks have to improve energy confinement time. The next step is the International Experimental Thermonuclear Reactor (ITER) that is under construction in France. ITER will be 2 times larger in linear dimensions than JET and aims for larger power output and confinement time reaching a quality factor of $Q \sim 10$. However, magnetic confinement requires a delicate plasma operation. Fluctuations in the plasma parameters that will occur on the process can lead to turbulent and fluid instabilities. Those instabilities can pose serious limiting factors in the maximum pressure achieved

and could severely damage the plasma facing components (PFCs) of a concept reactor. A better understanding for the cause and control of such instabilities is necessary to reach higher temperature, density and energy confinement time in the future.

1.3 H-mode & Edge Localised Modes

1.3.1 H-mode

Below a certain input power threshold, the plasma pressure is characterised by a mild gradient at the plasma edge, called the low confinement mode (L-mode), due to the existence of high levels of turbulence facilitating heat and particle transport from the hot core to the cold edge. A major step in the realisation of commercial fusion power was the discovery of high confinement mode (H-mode) in ASDEX [9], that lead to improved energy confinement time τ_E and an increase of plasma pressure by a factor of 2. This was achieved by the introduction of a divertor magnetic configuration instead of a limiter one. The limiter is a physical object that protrudes from the wall holding the plasma edge away from the wall. However, the interaction between the hot plasma and the limiter results in a turbulent state and the production of impurities that radiate heat and degrade the energy confinement time. The divertor configuration separates the equilibrium magnetic field into regions of closed and open field lines. The divertor geometry is made by placing a current carrying coil to produce a magnetic X-point. The open field lines serve as a guide leading the plasma to the divertor plates. As such, control of impurities is achievable leading to increased plasma performance and above an input power threshold H-mode operation is achieved. A schematic of those two magnetic configurations as well as typical pressure radial profiles in L/H mode can be seen in Fig.1.7.

The main observation is the identification of edge radial electric field E_r and sheared flows associated with $\boldsymbol{E} \times \boldsymbol{B}$ drifts, which nonlinearly interact with the increased edge turbulence [10],[11] in a narrow region typically a few centimetres inside the last closed flux surface (LCFS). Fluctuations in the perpendicular flow arising from turbulence lead to non-vanishing Reynolds

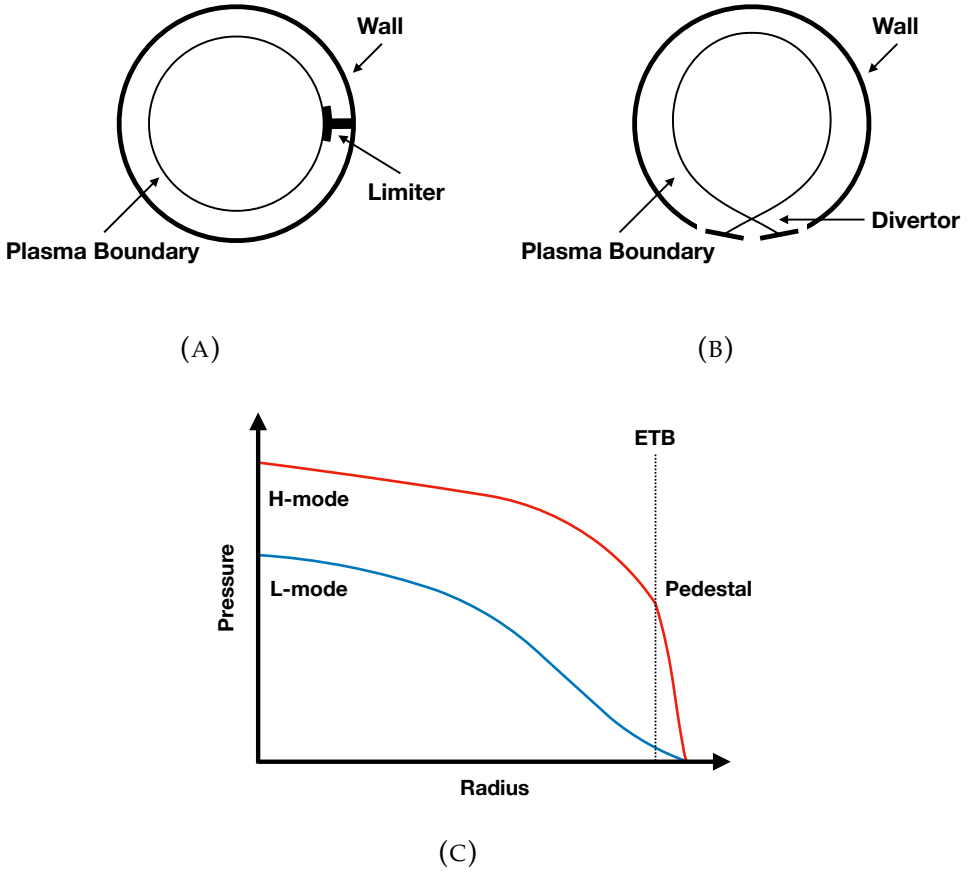

FIGURE 1.7: Schematic of (A) limiter configuration, (B) divertor configuration and L/H pressure profiles.

stress and together with the anisotropy that the magnetic field introduces, zonal flows lead eventually to the suppression of edge turbulence [12]. The formation of an edge transport barrier (ETB) leads to the development of a pedestal where the core plasma pressure increases significantly. This pedestal region is further supported from the $\nabla p \times \boldsymbol{B}$ flow driven from the establishment of steep pressure gradient [13] at the plasma edge. An additional advantage of the creation of steep pressure gradients is the significant increase of the bootstrap current (neoclassical and pressure gradient driven current) that naturally facilitates the creation of poloidal magnetic field at the plasma edge, necessary for efficient confinement of charged particles in a toroidal geometry. Due to its improved confinement, H-mode is planned to be the baseline operational mode for ITER [14].

1.3.2 ELM Phenomenology

The existence of steep pressure gradient and large current density at the plasma edge during H-mode operation, leads to excess free energy that can eventually destabilise macroscopic magnetohydrodynamic (MHD) instabilities that are manifested in the nonlinear phase as quasi-periodic bursts of edge localised modes (ELMs). During an ELM the pedestal profiles collapse to shallower gradients, for the external heating to rebuild the pedestal, leading to a cyclic behaviour. On average around $\sim 10 - 20\%$ of the energy stored in the pedestal is expelled within a timescale of the order of hundreds of microseconds leading to large transient heat and particle loads to PFCs. However, a benefit of those transients is the expulsion of impurities maintaining a clean plasma. Experimentally, ELMs are observed from the D_α line emission of Deuterium recombination and excitation on the divertor tiles of the tokamak, from current-voltage measurements from probes at the divertor or from direct imaging techniques that allowed the identification of their field-aligned filamentary structure. Fig.1.8 illustrates the D_α emission from an ELM burst in JET and a visible camera snapshot of ELM filaments as observed in the MAST spherical tokamak.

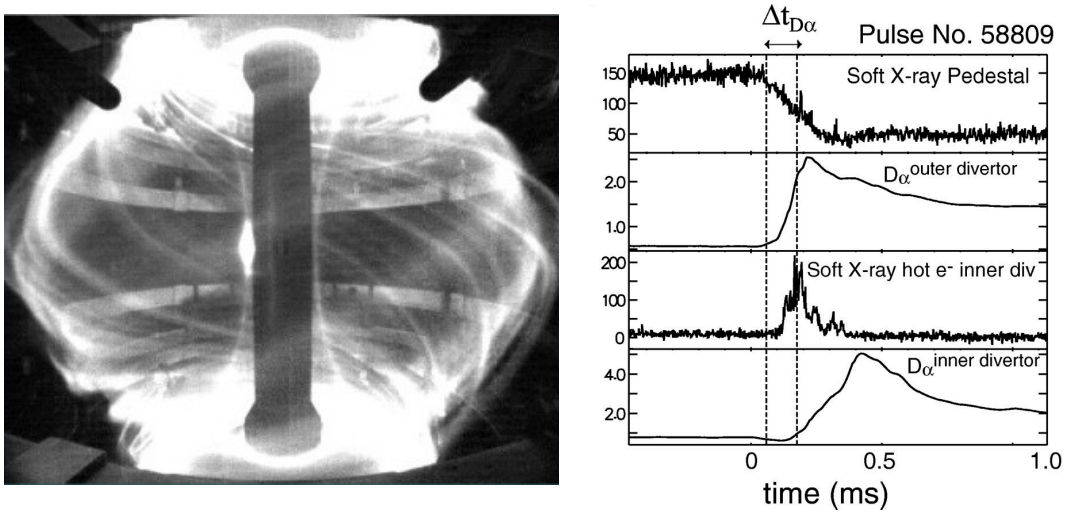

(A) (B)

FIGURE 1.8: (A) Type I ELM as observed through the visible fast camera system in MAST [15] and (B) the D_α emission as observed in the divertor [16] in JET.

The onset of ELMs is experimentally observed to be close to global MHD stability limits and the growth rate of the event is of the order of hundred Alfven

times $\sim \mathcal{O}(100)\ \tau_A$ suggesting that MHD events could explain the phenomenon. ELMs are classified in different types depending on plasma parameters and an overview of ELM phenomenology can be found in [17],[18],[19]. The main classification is based on the dependence of ELM frequency f_{ELM} to input power, the existence of a magnetic precursor and MHD stability considerations.

- **Type-I ELMs:** Also referred to as large or giant, type-I ELMs are observed in H-mode high input power plasmas. They are typically observed as distinct bursts in the D_α emission with an occurrence frequency of $\sim\ \mathcal{O}(10 - 100)$ Hz and their frequency increases with input heating power. Through magnetic measurements a $n \lesssim 10$ magnetic precursor is observed below a collisionality ν_e^* threshold [20], where n is the toroidal mode number. They result in the largest energy loss ΔW_{ELM} reaching up to $\sim 20\%$ of the pedestal energy [21]. For large scale fusion burning plasmas those transients are extrapolated to produce heat loads above the melting point of the divertor and PFCs [22],[23] so their active control becomes imperative.

- **Type-II ELMs:** Type-II ELMs are observed in a narrow window at high density and highly shaped plasmas, in terms of elongation and triangularity. In comparison to type-I ELMs, type-II ELMs have a higher frequency resulting in lower energy loss ΔW_{ELM} such that confinement is not dramatically affected. In addition, through magnetic measurements magnetic turbulence is observed in the inter-ELM phase [24]. Type-II ELMs offer good confinement maintaining a clean plasma and facilitating steady-state operation. However, they often coexist with type-I ELMs.

- **Type-III ELMs:** Also referred to as small, type-III ELMs are usually observed at the early stage of the H-mode when edge resistivity/temperature is high/low. The ELM frequency f_{ELM} decreases with input power and is found to be much higher than that of other types of ELMs leading to significantly lower energy loss per ELM. However, the operational regime in which they occur is restricted to low edge temperatures and density leading overall to low energy confinement time.

Alternative regimes that maintain good confinement, where ELMs are absent, have been experimentally identified. The QH-mode (quiescent H-mode)

[25],[26],[27] is one example, although the exact physics mechanism is poorly understood. One explanation is attributed to the existence of strong rotational shear at the edge of plasma which allows the saturation of edge MHD modes that lead to enhanced particle transport and allow an ELM-free operation [28]. One other example is the EDA (enhanced D_α emission) H-mode [29] observed for moderate shaping and low plasma current where edge fluctuations allow a continuous energy transport and good impurity recycling. Finally, the I-mode [30] obtained for a wide range of parameters shows the characteristic of a temperature transport barrier but no existence of a density transport barrier is observed allowing for an ELM-free regime.

1.3.3 Theoretical Understanding of type-I ELMs

The onset of large type-I ELMs is believed to be linked with unstable ideal MHD modes formed close to the ETB. The ideal MHD nature of the event is attributed to the Alfvenic timescale of the instability. The Alfvenic timescale is the characteristic time of ions oscillating in response to restoring magnetic field-line tension [31]. Over the last two decades analytical and computational work has identified two types of ideal MHD instabilities as the main mechanism for driving such edge modes. Those instabilities are driven by the pressure gradient and magnetic curvature, i.e. ballooning modes, and from the parallel current density, i.e. kink/peeling modes. H-mode operation naturally leads to the coupling of those two instabilities, to the so called peeling-ballooning modes [32],[33], due to the fact that steep pressure gradients are naturally accompanied by large edge bootstrap current density. However, these edge modes are quite complex phenomena as the bootstrap current, pressure gradient as well as magnetic shear play dual roles of stabilising and destabilising the plasma equilibrium.

1.4 ELM Control

1.4.1 ELM Control Methods

In ITER the main operational mode is expected to have type-I ELMs, unless controlled. As discussed in previous sections, the corresponding particle and heat losses of ELMs are extrapolated to surpass the melting point of PFCs and ELM control methods have to be applied to ensure safe operation together with high performance. Although plasma shaping can provide a way to enhance the MHD stability of the plasma, in large devices type-I ELMs are almost always present in high β_N operation. As such, active ELM control methods are required and three main strategies are experimentally examined. The first aims at the dispersion of the ELM front by radiation before it reaches the PFCs. The second focuses on further destabilisation of ELMs leading to increase in ELM frequency f_{ELM} and therefore decrease of the instantaneous ELM energy loss ΔW_{ELM} leading to mitigation. The third and final approach aims to achieve complete suppression of ELMs by accurate control and maintenance of pedestal characteristics below the peeling-ballooning stability boundary.

Radiating dispersion through impurity gas seeding either in the SOL or the divertor region is considered as the primary technique to minimise heat loads in PFCs during the inter-ELM cycle [34]. However, the reduction of transient heat loads is observed to be below the desirable level and further increase of the impurity seeding rate causes degradation of the pedestal leading to type-III ELMs [35],[36] and strong reduction in confinement time. As such additional mitigation/suppression techniques have to be applied. One ELM mitigation technique uses vertical kicks [37],[38] to trigger ELMs at a frequency which is locked with the kick. In practise the motion of the plasma induces currents at the plasma surface that are postulated to drive peeling modes leading to an ELM crash. However, experimental comparison between devices revealed controversial results [39] that question this assumption and the triggering mechanism is still not understood. Another mitigation technique is based on pellet pace-making of ELMs [40],[41],[42]. Experimentally this technique has been applied in a number of devices and ELMs were successfully triggered to frequencies even above the pellet injection rate. However, for ITER relevant scenarios much higher repetition rate needs to be achieved

for efficient mitigation of heat loads without over fuelling the plasma and decreasing confinement. Finally, one promising method to actively control ELMs uses external non-axisymmetric resonant magnetic perturbations (MPs). This method has been successfully applied in various devices and active ELM control was obtained allowing mitigation [43],[44],[45],[46], complete suppression [47],[48],[49],[50] and even triggering of ELMs [51]. However, the exact mechanisms that allow the existence of the distinct operational states with MPs are not fully understood. Resonant MPs are planned to be the main active ELM control method in ITER and therefore understanding the plasma response to external non-axisymmetric fields becomes crucial.

1.4.2 Resonant Magnetic Perturbations

External non-axisymmetric MPs are produced by in-vessel magnetic coils or external error field correction coils (EFCC). The main feature of those fields δB_{MP} is their relative size to the axisymmetric background equilibrium field B_0, typically $\delta B_{MP}/B_0 \sim 10^{-4} - 10^{-3}$. Although, two distinct operational plasma states occur where either ELM mitigation or complete ELM suppression is observed. A typical coil configuration of in-vessel coils is given in Fig.1.9. The coils can produce a magnetic perturbation of a primary toroidal harmonic N and by changing the relative current phase $\Delta\phi$ between the upper and lower row of coils, a range of resonant and non-resonant magnetic perturbations can be applied.

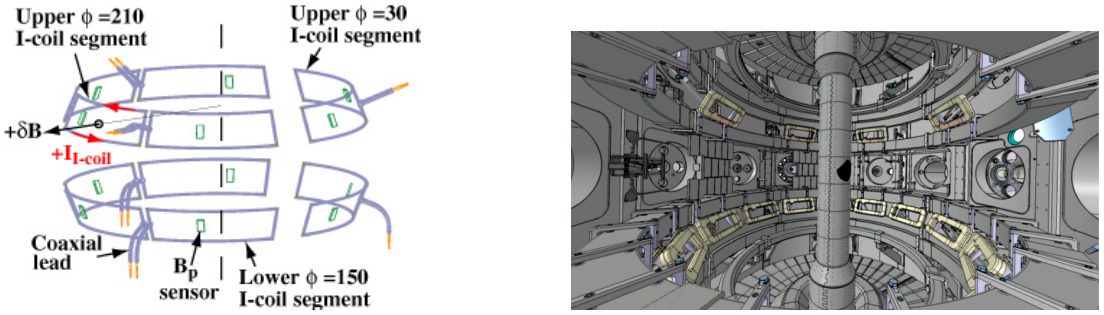

(A) (B)

FIGURE 1.9: A) The resonant MP coil configuration in DIII-D comprises six segments above the equatorial plane and six segments below [52]. B) The resonant MP coil configuration of MAST comprises of 6 segments above the equatorial plane and 12 segments below.

The first demonstration of ELM suppression was performed in DIII-D experiments using an $N = 3$ resonant MP field in a narrow window of q_{95} as illustrated in Fig.1.10a from the D_α emission. For ITER similar shape (ISS) plasmas, in high collisionality ELMs were replaced by sporadic events [52], while in low collisionality no activity is observed [47]. Recent similarity experiments from AUG also demonstrated complete ELM suppression [50] with an example of such a shot depicted in Fig.1.10b from probe measurements. However, the conditions necessary to reach suppression exhibit differences. A plasma density limit is observed in AUG below which suppression is established and a much larger q_{95} window is observed. In addition, although plasma flow seems to have an impact on DIII-D [53], this is not the case on AUG. In high density/collisionality ISS plasmas, ELM suppression has been achieved in a number of devices including EAST [48] and KSTAR [49] for a variety of applied toroidal mode numbers and coil phase.

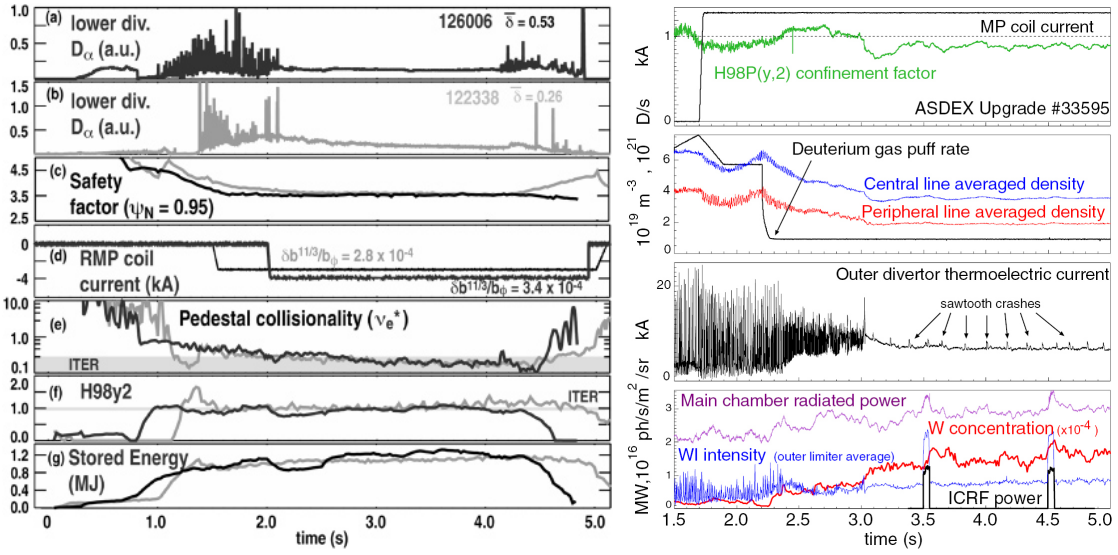

(A) (B)

FIGURE 1.10: A) Experimental measurements from DIII-D showing the D_α emission form the lower divertor, the safety factor, collisionality and H-factor for a high triangularity ISS and low triangularity plasma [47]. B) Experimental data from AUG depicting the H-factor, average line density, thermoelectric current and tungsten accumulation [50].

Although, complete ELM suppression occurs in a narrow window of the parameter space, ELM mitigation is routinely achieved by the application of MPs and Fig.1.11 mitigated cases from JET and MAST. In JET [45], efficient ELM mitigation using $N = 1$ and $N = 2$ field applied from the EFCC resulted

in a significant increase of the ELM frequency f_{ELM} reducing the energy loss ΔW_{ELM} below the noise level of the diagnostic. Similar observations are found in MAST [44] using a variety of applied toroidal modes and DIII-D [43] plasmas at cases where a resonant condition is not met or the applied field is below the suppression threshold. A common feature of all efficient ELM mitigated discharges is the strong increase of density pump-out (loss of plasma density). However, measurements of the electron temperature show a slow increase that under certain conditions can compensate for the loss in the pressure. Finally, RMPs have also been used to trigger ELMs in MAST [54] and NSTX [51] experiments and this could provide a mechanism for density control and avoidance of impurity accumulation.

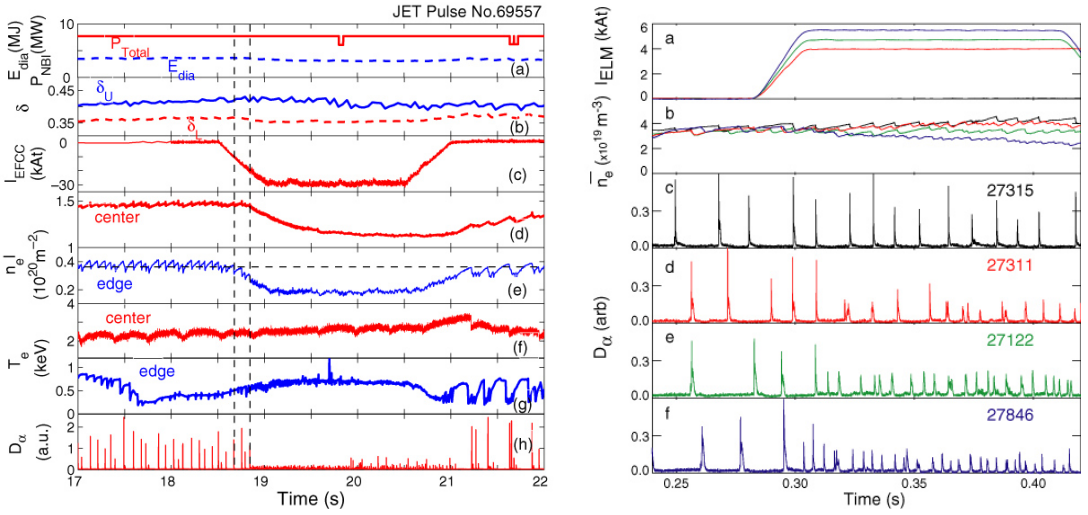

(A) (B)

FIGURE 1.11: Efficient ELM mitigated H-mode plasmas as observed in (A) JET [45] using the EFCC system and (B) in MAST [44] with increasing current in the In-Vessel Coil system.

Apart from the benefits that the MPs offer as a flexible method to actively control ELMs, their application hides operational hazards. One of the most important drawbacks of the application of MPs is a potential rotational braking [55],[56],[57]. In general, plasma rotation allows stabilisation of MHD instabilities, like Resistive-Wall modes [58] and Neoclassical Tearing modes [59], that pose serious limitation in plasma performance. Moreover, density pump-out can pose a limitation and degradation of achievable performance. Although, gas puffing can be used to compensate for the lost density, stored magnetic energy is not guaranteed to be restored while the risk of entering to a small ELM regime exists. Finally, it is still unclear whether MP coils are

compatible with a DEMO reactor due to neutron activation and damage of the coil components.

1.4.3 Current Understanding & Open Questions

ELM suppression using resonant MPs is achieved for low collisionality, low density plasmas and similarity experiments are successfully being performed between DIII-D and AUG. The main outcome of those campaigns is the observation of increased particle transport [60],[61],[62], i.e. density pump out, and broadband turbulence [63],[64]. A suppressed state seems to require low plasma density [50] but from existing experimental data it is not clear whether the density or pressure is important, or what is the role of edge collisionality. The use of resonant MPs can lead to formation of magnetic islands [65] that increased transport at the top of the pedestal allowing the relaxation of the pedestal below MHD stability limits. However, no reduction in the electron temperature is usually observed experimentally questioning the existence of island structures [43]. Plasma flow and MP induced shielding currents, which exist in the pedestal region, can prevent magnetic reconnection and the formation of magnetic islands [66].

Recent analytical investigation based on nonlinear two-fluid theory identified three regimes of magnetic reconnection [67],[68], where shielding depends on an offset velocity from the $\mathbf{E} \times \mathbf{B}$ drift rather than the perpendicular electron velocity $\mathbf{v}_{\perp e}$ that linear two-fluid theory suggests. An important implication of this theory is the coexistence of static or suppressed island regimes where bifurcation strongly depends on plasma flow and could provide insight into experimental observations. Recent results from DIII-D and AUG suggest that the perpendicular electron velocity in general does not vanish close to rational surfaces at the top of the pedestal. The $\mathbf{E} \times \mathbf{B}$ drifts are observed to vanish close to the top of the pedestal [50], [53] due to the electric field established from the ETB. Although, since no conclusive outcome can be drawn, the validity of the island transport model is questionable and remains an active area of research.

Furthermore, the establishment of a 3D equilibrium state can have a direct impact on MHD plasma stability. Local 3D MHD stability analysis reveals the significant impact of 3D geometry on local MHD instabilities. In particular, infinite n or local ballooning theory suggests that specific field-lines are further

destabilised due to the 3D field [69],[70],[71], where n is the toroidal mode number of the unstable mode. This feature of ballooning stability could provide an explanation for the observed increase in particle transport. However, intermediate n modes are responsible for the occurrence of ELMs and a global 3D analysis is needed, but has not yet been applied to an MP ELM control scenario. Such an investigation has been performed computationally by nonlinear visco-resistive MHD codes [72],[73],[74],[75], but conclusions regarding the linear stability of an ideal MHD plasma are not straightforwardly inferred due to transport processes. Moreover, analytic investigation using perturbation theory to examine the impact of shielding current sheets driven by MPs on axisymmetric unstable MHD modes, revealed that MPs can have a significant impact on global stability [76]. The main outcome of such studies is the observation of strong coupling of toroidal modes with increasing applied MP field that affects the linear growth rate of unstable peeling-ballooning modes as well as their nonlinear dynamics.

In conclusion, the equilibrium geometry itself is observed to play a crucial role in achieving suppression suggesting the importance of MHD stability. In similarity experiments between DIII-D and AUG, ELM suppression occurred at higher triangularity, suggesting increased stability for peeling-ballooning modes. A recent investigation of experimental data indicates the change of peeling-ballooning stability due to density pump-out and surface corrugation [77], where the occurrence of mitigation or suppression is attributed to the competence of degraded stability due to 3D effects and stabilisation due to reduced density/pressure. Last but not least, ELM suppression has not been achieved in connected double null (CDN) configuration or in spherical tokamaks like MAST. Especially for spherical tokamaks, due to their unique plasma parameters and shape, it is still an open question whether different conditions need to be met in order to achieve an ELM-free operation using MPs.

1.5 Thesis Goal & Outline

As discussed in the above section, the physics mechanism that leads to reliable ELM suppression using MPs is not yet well understood. Better understanding is required in the MP field penetration process and island formation under

plasma flows, the correct 3D equilibrium that is established as well as its impact to stability and transport. This thesis discusses the impact of MPs on ideal MHD modes and in particular the peeling-ballooning stability of the tokamak plasma. Little literature exists regarding the 3D peeling-ballooning stability of the plasma since existing 3D stability codes (TERPSICHORE [78], CAS3D [79], CASTOR3D [80], PB3D [81], etc) are not typically used for intermediate to high n modes, where n is the toroidal harmonic of the perturbation. In this thesis, the 3D stability of the plasma is examined using axisymmetric stability codes, which are routinely used for the stability of intermediate to high n modes. Through analytical theory, the plasma response, i.e. the 3D part of the equilibrium, and axisymmetric normal modes can be used to approximate the stability of the 3D system. In particular, axisymmetric stability codes provide the axisymmetric peeling-ballooning eigenfunctions (mode structure), which are used as basis-functions within a perturbative and variational representation of the extended energy principle, and the linearised plasma response in marginal stability. As such a computational framework can be developed based on some axisymmetric stability code suitable for all ranges of toroidal modes. In this work the code under consideration was the low n ELITE eigenvalue linear stability code [82], [83].

The thesis is separated in the next four chapters. Chapter2 introduces the mathematical means used to examine the plasma, introducing the ideal MHD model and the extended energy principle used to study plasma stability. In addition it introduces and discusses the main MHD instabilities that lead to the ELM onset, i.e. ballooning and external kink/peeling modes. In Chapter3 the procedure under which ELITE is used to produce a linearised 3D equilibrium is explained. Furthermore, the perturbative and variational formulation of the energy principle is described in detail and the computation of the additional 3D energy terms that emerge are presented. In Chapter4, results are presented regarding the linear plasma response as produced by ELITE and benchmarks are presented using the BOUT++ fluid code [84] and the MARS-F eigenvalue code [85]. Moreover, results are presented regarding the linear 3D MHD stability using large aspect ratio circular and D-shaped H-mode plasmas. Finally, Chapter5 discusses the results using the above techniques in comparison to current theoretical and experimental understanding, as well as summarises the thesis.

Chapter 2

Plasma Description

2.1 Ideal MHD Model

A tokamak reactor is a device that uses magnetic coils to produce a toroidal magnetic field and the poloidal magnetic field is produced by driving a toroidal current into the plasma. The motion of charged particles inside such a field is described by the Lorentz force. In principle the plasma can be described in the most fundamental level by evolving the canonical positions and momenta of all particles. However, this particle description is impractical due to the immense number of particles. The first simplification arises from the consideration of a generalised statistical distribution f_s for the species s, that describes the amount of particles occupying a volume in the phase space (generalised position-momentum space) at all times. The evolution of such a statistical distribution is given by the Boltzmann transport equation [86],

$$\mathrm{d}_t f_s = \{\partial_t + \boldsymbol{v}_s \cdot \nabla_{\boldsymbol{x}} + \boldsymbol{a}_s \cdot \nabla_{\boldsymbol{v}}\} f_s \equiv \sum_{s'} C_{ss'} + S_s \tag{2.1}$$

where $\boldsymbol{v}_s$ is the species velocity, $\boldsymbol{a}_s$ is the species acceleration, $C_{ss'}$ represents usually species collisions and S_s represents species sources and sinks. The acceleration is obtained from the Lorentz force such that $\boldsymbol{a}_s = \frac{eZ_s}{m_s}(\boldsymbol{E} + \boldsymbol{v}_s \times \boldsymbol{B})$, where $\boldsymbol{E}$ and $\boldsymbol{B}$ are the electric and magnetic field respectively, e the electric charge, Z_s the species atomic number and m_s the species mass.

The Boltzmann transport equation represents a partial differential equation in a 6-dimensional phase space. Even with today's most powerful supercomputers

the numerical investigation of such systems is impractical if not impossible. For that reason further analytical reduction is needed to solve practical problems. Most plasma phenomena can still be studied in a macroscopic level considering the fluid properties of the plasma. For a fluid description to be valid, particles must collide frequently. Although the parallel collisional mean-free path $\lambda_{||}$ is large in hot magnetised plasmas, the magnetic field creates a much shorter effective mean free path in the perpendicular direction due to the very small gyro-radius. As such, in general the fluid condition $\lambda_{\perp}\nabla f \ll f$ is met for perpendicular dynamics [87] which are usually under consideration.

The fluid description is mathematically equivalent to the velocity moments of the distribution function at each point in space. These moments are given by [88],

$$\partial_t \rho_s + \nabla \cdot (\rho_s \boldsymbol{v}_s) = 0 \tag{2.2a}$$

$$\partial_t(\rho_s \boldsymbol{v}_s) + \nabla \cdot (\rho_s \boldsymbol{v}_s \boldsymbol{v}_s) = -\nabla p_s - \nabla \cdot \boldsymbol{\pi}_s + \frac{eZ_s\rho_s}{m_s}(\boldsymbol{E} + \boldsymbol{v}_s \times \boldsymbol{B}) + \boldsymbol{R}_{ss'} \tag{2.2b}$$

$$\partial_t(\rho_s e_s) + \nabla \cdot (\rho_s e_s \boldsymbol{v}_s) = -p_s \nabla \cdot \boldsymbol{v}_s - \nabla \cdot \boldsymbol{q}_s + \boldsymbol{\pi}_s : \nabla \boldsymbol{v}_s + Q_{ss'} \tag{2.2c}$$

where ρ_s is the density, $\boldsymbol{v}_s$ the fluid velocity, e_s the energy density and p_s the pressure of an ideal gas. Additional transport quantities that arise refer to $\boldsymbol{\pi}$ the viscous stress, $\boldsymbol{q}_s$ the heat flux, $\boldsymbol{R}_{ss'}$ the collisional force and $Q_{ss'}$ the collisional heat transfer. The system described by Eqn.2.2 is closed by relating the pressure to the energy density $p_s = (\Gamma_s - 1)\rho_s e_s$, where Γ_s is the adiabatic index, and using Maxwell's equations Eqn.2.3 that relate the electromagnetic field to the density and flow. A simplification on the electromagnetic-matter coupling is possible considering the speed of light $c \to \infty$ to be infinite. This condition assumes displacement currents are neglected and the system is limited to low frequency phenomena. This results in a reduced system given by,

$$\nabla \cdot \boldsymbol{E} = \sum eZ_s n_s = \frac{\rho_c}{\epsilon_0} \tag{2.3a}$$

$$\nabla \times \boldsymbol{B} = \mu_0 \sum eZ_s n_s \boldsymbol{v}_s = \mu_0 \boldsymbol{J} \tag{2.3b}$$

$$\nabla \cdot \boldsymbol{B} = 0 \tag{2.3c}$$

$$\partial_t \boldsymbol{B} = -\nabla \times \boldsymbol{E} \tag{2.3d}$$

where ϵ_0 and μ_0 are the permittivity and permeability of free space respectively. As a result of Eqn.2.3 a certain charge density ρ_c remains unchanged $\partial_t \rho_c \rightarrow 0$, guaranteeing the quasi-neutrality condition of the plasma $\rho_c = 0$ at all times. However, we will restrict consideration to plasma phenomena which are restrained to frequencies much smaller than the electron plasma frequency $\omega << \omega_{pe} = (e/m_e)\sqrt{\rho_e/\epsilon_0}$ and length scales much larger than the Debye length $L \gg \lambda_D = v_{T_e}/\omega_{pe}$, where $v_T = \sqrt{k_B T/m}$ the thermal speed.

The complete multi-fluid visco-resistive plasma described above is still complicated and computationally expensive. Nevertheless, further simplification is possible by considering a two-fluid electron-ion plasma which is in thermal equilibrium between the two species, such that $T_i = T_e$. First of all, the quasi-neutrality of the plasma relates the electron and ion density such that $n_e = Z n_i$. In addition, the plasma current is related to the relative motion of electrons and ions, such that $\boldsymbol{J} = e n_e (\boldsymbol{v}_i - \boldsymbol{v}_e)$. Moreover, the plasma phenomena studied in this thesis are Alfvenic and their dynamics are much faster than any resistive or dissipative mechanism within the plasma. Therefore, for the examination of linearised Alfvenic dynamics, visco-resistive terms are considered negligible. Electron inertia is also considered negligible since $m_e \ll m_i$. Those assumptions lead to a significant simplification of our mathematical model, leading to a conservative system called the ideal MHD model,

$$\partial_t \rho + \nabla \cdot (\rho \boldsymbol{v}) = 0 \tag{2.4a}$$

$$\partial_t (\rho \boldsymbol{v}) + \nabla \cdot (\rho \boldsymbol{v}\boldsymbol{v}) = -\nabla p + \boldsymbol{J} \times \boldsymbol{B} \tag{2.4b}$$

$$\frac{1}{\Gamma - 1}[\partial_t p + \nabla \cdot (p \boldsymbol{v})] = -p \nabla \cdot \boldsymbol{v} \tag{2.4c}$$

$$\partial_t \boldsymbol{B} = \nabla \times (\boldsymbol{v} \times \boldsymbol{B}) \tag{2.4d}$$

In this model, the plasma is treated as an ideal conductor. It can be proven that the magnetic field is locked with the fluid motion and changes in the magnetic topology are forbidden within this model.

2.2 MHD Equilibrium

2.2.1 Equilibrium Configuration

The ideal MHD system described above in Eqn.2.4 can be naturally used to derive equilibrium conditions for the plasma dynamics. Typically the coordinate system under consideration will be such that the plasma is static, i.e. $\boldsymbol{v} = 0$. An equilibrium state is such that quantities are not evolving in time, i.e. time derivatives are neglected $\partial/\partial t \to 0$. This leads to a force balance between the Lorentz force and the fluid pressure as given by:

$$\boldsymbol{J} \times \boldsymbol{B} = \nabla p \tag{2.5}$$

Important properties arise from Eqn.2.5 that are widely used in the determination of a field aligned coordinate system as well as the plasma stability and dynamics. In an equilibrium configuration no magnetic field exists parallel to pressure gradient, since $\boldsymbol{B} \cdot \nabla p = \boldsymbol{B} \cdot (\boldsymbol{J} \times \boldsymbol{B}) = 0$. In addition, no current density can exist parallel to the pressure gradient for similar reasons, $\boldsymbol{J} \cdot \nabla p = \boldsymbol{J} \cdot (\boldsymbol{J} \times \boldsymbol{B}) = 0$. As such the magnetic field and current density lie on surfaces of constant pressure. This implies that those surfaces are surfaces of constant poloidal magnetic flux and are typically used as the normal coordinate of the system. In a tokamak configuration those pressure contours define nested toroidal surfaces and are characterised by the twist of the magnetic field, called the safety factor q. This quantity is topologically a flux quantity that measures the ratio of toroidal $\Delta\Phi$ to poloidal $\Delta\Psi$ flux variation. Geometrically, it is a measure of the poloidal winding of the magnetic field lines over a toroidal revolution. Special surfaces exist for safety factors that are rational, which are called rational or resonant surfaces. On those surfaces magnetic field lines are close back to themselves after a complete toroidal revolution. Those surfaces resonate with harmonic waves of distinct poloidal m and toroidal n mode numbers exhibiting interesting stability properties. For non-rational surfaces, field lines cover those surfaces ergodically.

Reformulation of Eqn.2.5 reveals the significance of balancing magnetic curvature with the total pressure gradient, i.e. magnetic and fluid pressure

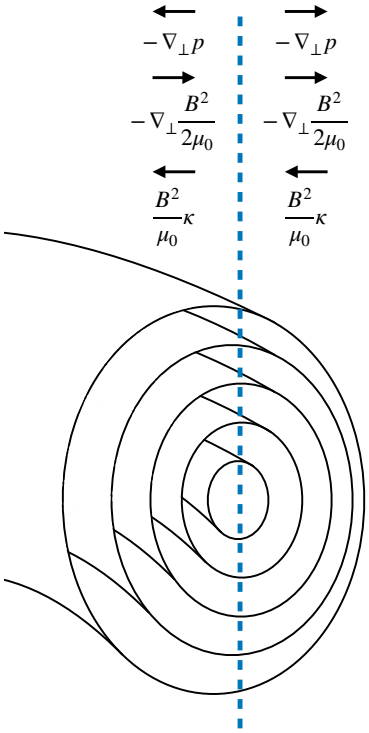

FIGURE 2.1: Schematic of the force resulted from fluid pressure $-\nabla_\perp p$, magnetic pressure $-\nabla_\perp B^2/(2\mu_0)$ and magnetic field line tension $(B^2/\mu_0)\boldsymbol{\kappa}$.

gradient. An alternative representation of the perpendicular force balance can be derived with respect to the magnetic curvature $\boldsymbol{\kappa} = \boldsymbol{b} \cdot \nabla \boldsymbol{b}$ with $\boldsymbol{b} = \boldsymbol{B}/|\boldsymbol{B}|$,

$$\frac{B^2}{\mu_0}\boldsymbol{\kappa} = \nabla_\perp (p + \frac{B^2}{2\mu_0}) \tag{2.6}$$

The magnetic field provides additional pressure $B^2/2\mu_0$ and together with the fluid pressure p are balanced by field line tension or the curvature of the magnetic field. Therefore, on a flux surface magnetic field lines try to acquire minimum length. A schematic of the different forces is illustrated in Fig2.1. At the outboard side of the torus the magnetic curvature balances the total (fluid + magnetic) pressure, while in the inboard side the magnetic pressure balances the fluid pressure and curvature. The balance between total pressure and magnetic curvature plays a crucial role in the stability of tokamak plasmas.

2.2.2 Orthogonal & Straight Field Line Toroidal Coordinates

In this thesis the coordinate system used is based on orthogonal axisymmetric toroidal coordinates. As discussed in the above section, the toroidal and poloidal magnetic flux creates toroidal nested surfaces, which can be used to represent the normal vector $\boldsymbol{n}$ with respect to the axisymmetric magnetic field $\boldsymbol{B}_0$. Typically in tokamak plasmas the gradient of the poloidal magnetic flux $\nabla\psi$ is used to represent the normal vector $\boldsymbol{n}$. The poloidal-like angle coordinate $\nabla\theta$ is chosen to be parallel to the tangent vector of the flux surface, while the toroidal angle coordinate $\nabla\phi$ follows the axis of symmetry. The coordinate system $\{\psi, \theta, \phi\}$ is illustrated in Fig.2.2

The contravariant metrics $\{g^{\psi\psi}, g^{\theta\theta}, g^{\phi\phi}\}$ and jacobian $\mathcal{J}$ of the coordinate system can be obtained from the poloidal magnetic flux ψ and the toroidal coordinate $\nabla\phi$. The poloidal magnetic flux defines the stream function of the magnetic field through a poloidal cross-section of the torus. Considering the solenoid nature of the magnetic field $\nabla \cdot \boldsymbol{B}_0 = 0$, the poloidal magnetic flux is related to B_R and B_Z,

$$RB_R = -\partial_Z\psi \;\; ; \;\; RB_Z = \partial_R\psi \tag{2.7}$$

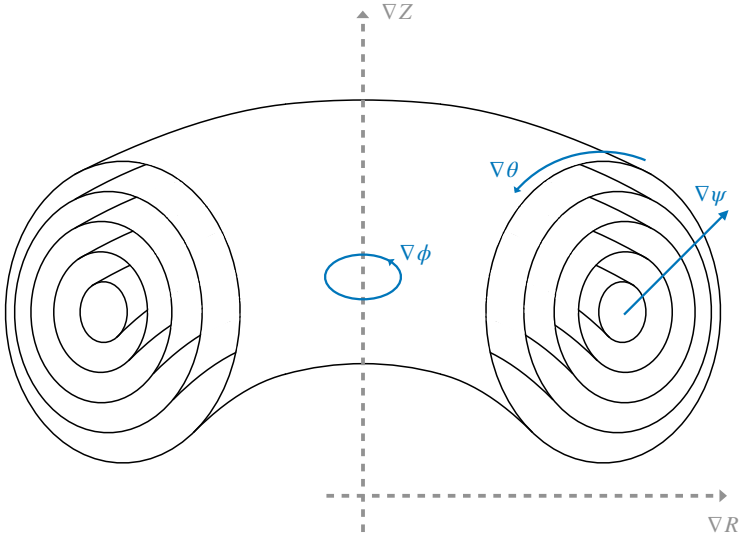

FIGURE 2.2: Schematic of the orthogonal coordinate system of a tokamak plasma.

Considering the magnitude of the gradient of the poloidal flux $|\nabla\psi| = RB_p$, where $B_p = \sqrt{B_R^2 + B_Z^2}$, the metric of the normal coordinate $g^{\psi\psi} = |\nabla\psi|^2$ is obtained. Moreover, the metric of the toroidal angle is $g^{\phi\phi} = |\nabla\phi|^2 = R^{-2}$, since the radius of curvature of a circle is its distance from its axis. The metric of the poloidal like angle can be obtained using the local pitch angle of the magnetic field $\nu = (\boldsymbol{B}_0 \cdot \nabla\phi)/(\boldsymbol{B}_0 \cdot \nabla\theta)$. A quick algebraic manipulation results in $g^{\theta\theta} = |\nabla\theta|^2 = (B_t/\nu B_p)^2 R^{-2}$, where B_t is the toroidal magnetic field. Furthermore, the jacobian needs to be evaluated to complete the knowledge of the metric system under consideration. This can be done by considering its relation to the contravariant metrics $\mathcal{J} = [\nabla\psi \cdot (\nabla\theta \times \nabla\phi)]^{-1} = \nu R^2/B_\phi$, where $B_\phi = RB_t$. Eqn.2.8 summarises the representation of quantities for the axisymmetric orthogonal coordinate system and equilibrium magnetic field:

$$\begin{pmatrix} g^{\psi\psi} & 0 & 0 \\ 0 & g^{\theta\theta} & 0 \\ 0 & 0 & g^{\phi\phi} \end{pmatrix} = \begin{pmatrix} g_{\psi\psi}^{-1} & 0 & 0 \\ 0 & g_{\theta\theta}^{-1} & 0 \\ 0 & 0 & g_{\phi\phi}^{-1} \end{pmatrix} = \begin{pmatrix} (RB_p)^2 & 0 & 0 \\ 0 & (JB_p)^{-2} & 0 \\ 0 & 0 & R^{-2} \end{pmatrix} \tag{2.8a}$$

$$\mathcal{J} = \frac{1}{\nabla\psi \cdot (\nabla\theta \times \nabla\phi)} = \frac{\nu R^2}{B_\phi} \tag{2.8b}$$

$$\boldsymbol{B}_0 = \nabla\psi \times (\nu\nabla\theta - \nabla\phi) = \frac{1}{\mathcal{J}}(g_{\theta\theta}\nabla\theta + \nu g_{\phi\phi}\nabla\phi) \tag{2.8c}$$

Finally, the poloidal-like angle θ can be mapped in the straight field line angle θ^*, where the magnetic field lines appear as "straight" on the $\{\theta^*, \phi\}$ plane with a fixed slope equal to the safety factor q. This allows the efficient decomposition of quantities in Fourier harmonics with distinct mode number. In a straight field line system the magnetic pitch becomes constant and equivalent to the safety factor q. This implies that $\mathrm{d}\theta^* = H(\psi,\theta)\mathrm{d}\theta$, where $H(\psi,\theta) = \nu/q$. In this coordinate system, the coordinates defining the poloidal plane are not orthogonal anymore and the metric system needs alternation. Considering the normal gradient of the straight field line angle θ^* the nonorthogonal contravariant metric,

$$g^{\psi\theta^*} = g^{\theta^*\psi} = (RB_p)^2 \int_0^\theta \partial_\psi H \, \mathrm{d}\theta \tag{2.9}$$

Since the poloidal plane coordinates are still orthogonal to the toroidal coordinate the $g^{\psi\phi} = g^{\theta^*\phi} = 0$. The jacobian of this coordinate system can be obtained in a similar way to the orthogonal system considering that $q = (\boldsymbol{B}_0 \cdot \nabla\phi)/(\boldsymbol{B}_0 \cdot \nabla\theta^*)$. Eqn.2.10 summarises the representation of quantities for the axisymmetric straight field line coordinate system and equilibrium magnetic field.

$$\begin{pmatrix} g^{\psi\psi} & g^{\psi\theta^*} & 0 \\ g^{\theta^*\psi} & g^{\theta^*\theta^*} & 0 \\ 0 & 0 & g^{\phi\phi} \end{pmatrix} = \begin{pmatrix} (RB_p)^2 & I(RB_p)^2 & 0 \\ I(RB_p)^2 & (IRB_p)^2 + (\mathcal{J}B_p)^{-2} & 0 \\ 0 & 0 & R^{-2} \end{pmatrix} \tag{2.10a}$$

$$\begin{pmatrix} g_{\psi\psi} & g_{\psi\theta^*} & 0 \\ g_{\theta^*\psi} & g_{\theta^*\theta^*} & 0 \\ 0 & 0 & g_{\phi\phi} \end{pmatrix} = H^2 \begin{pmatrix} (I\mathcal{J}B_p)^2 + (1/RB_p)^2 & -I(\mathcal{J}B_p)^2 & 0 \\ -I(\mathcal{J}B_p)^2 & (\mathcal{J}B_p)^2 & 0 \\ 0 & 0 & R^2 \end{pmatrix} \tag{2.10b}$$

$$\mathcal{J} = \frac{1}{\nabla\psi \cdot (\nabla\theta^* \times \nabla\phi)} = \frac{qR^2}{B_\phi} \tag{2.10c}$$

$$\boldsymbol{B}_0 = \nabla\psi \times (q\nabla\theta^* - \nabla\phi) = \frac{1}{\mathcal{J}}(g_{\theta\theta}\nabla\theta^* + qg_{\phi\phi}\nabla\phi) \tag{2.10d}$$

2.3 MHD Stability & Energy Principle

2.3.1 Linear Exponential Stability

Plasma stability is a crucial topic since instabilities lead to enhanced transport and disruptions, that degrade confinement and can damage PFCs. When an equilibrium is established the main question that arises is whether this equilibrium configuration leads to a stable or unstable system, when subject to small perturbations. In practise this means that if the equilibrium is displaced will this result in forces that enhance or counter the change and Fig.2.3 illustrates some examples of stable and unstable systems. Non-linear stability theory treats the behaviour of finite perturbations and can provide metastable

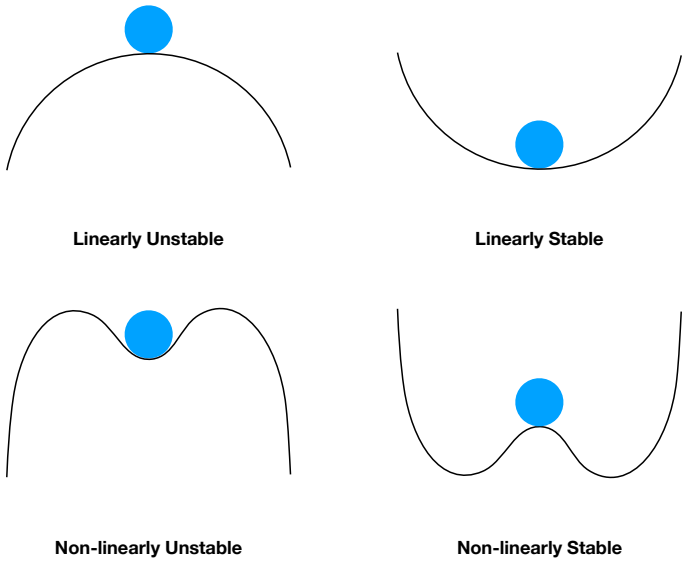

FIGURE 2.3: Schematic of different states where a system can be linear stable or unstable and nonlinearly stably or unstable.

or saturated solutions for a system. However, such analysis is usually complex and impractical, usually requiring expensive numerical calculations. A simpler but robust method is linear stability theory that treats the behaviour of infinitesimal perturbations around an equilibrium point. Linear theory often allows analytical treatment leading to the calculation of approximate stability limits that provide information on the drive of instabilities that need to be avoided.

Therefore, the first step is the linearisation of the MHD equation. A certain quantity $\tilde{F}$ can be expressed as a superposition of an equilibrium component F and a first order perturbation δF, such that $\tilde{F} = F + \delta F$. Since those perturbations are infinitesimal they are much smaller $\delta F \ll F$ than any equilibrium quantity. As such second order perturbed quantities are negligible and omitted from the analysis. Assuming no initial flow, i.e. $\boldsymbol{v} = 0$, the linearisation to first order of Eqn.2.4 results in,

$$\partial_t \delta\rho = \nabla \cdot (\rho \boldsymbol{\delta v}) \tag{2.11a}$$

$$\rho \partial_t \boldsymbol{\delta v} = -\nabla \delta p + \boldsymbol{\delta J} \times \boldsymbol{B} + \boldsymbol{J} \times \boldsymbol{\delta B} \tag{2.11b}$$

$$\partial_t \delta p = -\boldsymbol{\delta v} \cdot \nabla p - \Gamma p \nabla \cdot \boldsymbol{\delta v} \tag{2.11c}$$

$$\partial_t \boldsymbol{\delta B} = \nabla \times (\boldsymbol{\delta v} \times \boldsymbol{B}) \tag{2.11d}$$

Considering that the unperturbed system is axisymmetric and displaced by $\boldsymbol{\delta\xi}$, from Eqn.2.11 a similar linearised non-axisymmetric equilibrium component arises by balancing the perturbed linear forces. Noting that acceleration is zero in equilibrium $\partial_t \boldsymbol{\delta v} = 0$, $\nabla \delta p = \boldsymbol{\delta J} \times \boldsymbol{B} + \boldsymbol{J} \times \boldsymbol{\delta B}$. Once again the perturbed pressure gradient $\nabla \delta p$ is balanced by the perturbed magnetic pressure and curvature provided from the magnetic field $\boldsymbol{\delta B}$ and current density $\boldsymbol{\delta J}$ perturbations. This linearised equilibrium can provide a non-axisymmetric equilibrium component as a perturbation on the axisymmetric equilibrium. This approach allows axisymmetric stability codes to provide the 3D equilibrium part at marginal stability, i.e. $\partial_t \rightarrow 0$, if an appropriate boundary condition is applied to the plasma-vacuum interface.

The stability of Eqn.2.11 can be studied by numerically evolving the system for certain displaced equilibrium conditions and observing a convergence or divergence from the original equilibrium configuration. However, this method can be computationally expensive for multi-dimensional systems or for instabilities close to marginal stability. An alternative and powerful method to study the linear stability of an equilibrium state is its exponential stability, where the convergence or divergence is determined by the eigenvalues of the linear system. This method guarantees that if a system is displaced from its equilibrium configurations will converge/diverge at least/most at a certain defined rate. In the case where a certain equilibrium is stable, exponential stability is also equivalent to asymptotic stability, where the displaced system always returns to its original equilibrium configuration.

These features indicate a certain functional form for the time dependence of a perturbed quantity, such that $\delta f(\boldsymbol{x}, t) \equiv \delta f(\boldsymbol{x}) e^{i\omega t}$. Inserting this form into Eqn.2.11 and taking into account $\boldsymbol{\delta v} = i\omega \boldsymbol{\delta\xi}$, where $\boldsymbol{\delta\xi}$ is the plasma displacement, and $\partial_t = i\omega$ results in a time-invariant system,

$$-\omega^2 \rho \boldsymbol{\delta\xi} = \boldsymbol{F}(\boldsymbol{\delta\xi}) = -\nabla \delta p + \boldsymbol{\delta J} \times \boldsymbol{B} + \boldsymbol{J} \times \boldsymbol{\delta B} \tag{2.12a}$$

$$\delta\rho = \nabla \cdot (\rho \boldsymbol{\delta\xi}) \tag{2.12b}$$

$$\delta p = -\boldsymbol{\delta\xi} \cdot \nabla p - \Gamma p \nabla \cdot \boldsymbol{\delta\xi} \tag{2.12c}$$

$$\boldsymbol{\delta B} = \nabla \times (\boldsymbol{\delta\xi} \times \boldsymbol{B}) \tag{2.12d}$$

The stability of Eqn.2.12 depends on the eigenvalues $-\omega^2$. An important detail of exponential stability is the existence of a discrete set of eigenvalues. Although this is not in general true, ideal MHD unstable modes always form a discrete spectrum [89] allowing the use of exponential stability theory for the unstable part of the spectrum. An additional feature of the force operator $\boldsymbol{F}(\boldsymbol{\delta\xi})$ is the hermitian nature of it. This forces the eigenvalues to be purely real and the eigenvectors to be orthogonal. As such, positive eigenvalues indicate instability, or alternatively the growth rate is $\gamma = \mathrm{Im}\{\omega\}$, where the faster growing mode will dominate the solution.

2.3.2 Extended MHD Energy Principle

The linear stability of ideal MHD is intrinsically linked with the eigenvalues and eigenvectors of the hermitian force operator $\boldsymbol{F}(\boldsymbol{\delta\xi})$ taking into account appropriate boundary conditions that $\boldsymbol{\delta\xi}$ needs to satisfy. In particular Eqn.2.12 is equivalent to a normal mode equation due to the hermitian nature of the system. A normal mode represents an eigensolution of a system in terms of linearly independent solutions. Those eigensolutions are orthogonal to each other such that excitation of one mode cannot lead to excitation of other modes and therefore can be studied independently. In addition, normal modes require the minimum amount of energy for their excitation and this leads to a variational formulation that recasts Eqn.2.12 from a differential to an integral problem.

The variational formulation of ideal MHD makes use of energy minimisation to obtain the eigenvalues and eigenvectors of the system. To begin with, the momentum conservation equation Eqn.2.12a is converted into an energy equation, where the change in kinetic $\omega^2\delta K$ and potential δW energy need to be represented. This is equivalent to the inner product of Eqn.2.12a with the displacement under consideration, such that

$$\delta W(\boldsymbol{\delta\xi}^\dagger, \boldsymbol{\delta\xi}) = \omega^2 \delta K(\boldsymbol{\delta\xi}^\dagger, \boldsymbol{\delta\xi}) \tag{2.13a}$$

$$\delta K(\boldsymbol{\delta\xi}^\dagger, \boldsymbol{\delta\xi}) = \frac{1}{2}\int \rho|\boldsymbol{\delta\xi}|^2 \,\mathrm{dV} \tag{2.13b}$$

$$\delta W(\boldsymbol{\delta\xi}^\dagger, \boldsymbol{\delta\xi}) = -\frac{1}{2}\int \boldsymbol{\delta\xi}^\dagger \cdot \boldsymbol{F}(\boldsymbol{\delta\xi})\ \mathrm{dV} \tag{2.13c}$$

The trial function $\boldsymbol{\delta\xi}$ that leads to an extremum in ω^2 is a true eigensolution of the system and automatically satisfies the momentum equation Eqn.2.12a, since itself is a result of the minimisation of the mechanical action of a system. According to the energy principle if a displacement $\boldsymbol{\delta\xi}$ exists such that $\delta W(\boldsymbol{\delta\xi}^\dagger, \boldsymbol{\delta\xi}) < 0$ the equilibrium is considered unstable. This is equivalent to a growth rate $\gamma = \mathrm{Im}\{\omega\}$, being consistent with exponential stability analysis. Therefore, in order to understand the stability of a system, the knowledge of the lower bound of δW is sufficient for the determination of its stability properties without explicit quantification of the growth rate γ.

In fact, the ideal MHD δW can be written as a combination of stabilising and destabilising terms allowing a physical understanding of the behaviour of the system. By considering the original expression $\boldsymbol{F}(\boldsymbol{\delta\xi})$ and after some algebraic manipulation δW can be written in terms of a plasma volume term, a plasma surface term and a vacuum term, $\delta W = \delta W_p + \delta W_s + \delta W_v$ [90], where

$$\begin{aligned}\delta W_p(\boldsymbol{\delta\xi}^\dagger, \boldsymbol{\delta\xi}) = \frac{1}{2\mu_0}\int &[|\boldsymbol{\delta B}_\perp|^2 + B^2|\nabla\cdot\boldsymbol{\delta\xi}_\perp + 2\boldsymbol{\kappa}\cdot\boldsymbol{\delta\xi}_\perp|^2 + \mu_0\Gamma p|\nabla\cdot\boldsymbol{\delta\xi}|^2 \\ &- \mu_0\frac{\boldsymbol{J}\cdot\boldsymbol{B}}{B^2}(\boldsymbol{\delta\xi}_\perp^\dagger \times \boldsymbol{B})\cdot\boldsymbol{\delta B}_\perp \\ &- 2\mu_0(\boldsymbol{\delta\xi}_\perp\cdot\nabla p)(\boldsymbol{\delta\xi}_\perp^\dagger\cdot\boldsymbol{\kappa})]\ \mathrm{dV}\end{aligned} \tag{2.14a}$$

$$\delta W_s(\boldsymbol{\delta\xi}^\dagger, \boldsymbol{\delta\xi}) = \frac{1}{2\mu_0}\int |\boldsymbol{\delta\xi}_\perp\cdot\boldsymbol{n}|^2([\![B^2\boldsymbol{\kappa}]\!])\cdot\boldsymbol{n}\ \mathrm{dS} \tag{2.14b}$$

$$\delta W_v(\boldsymbol{\delta\xi}^\dagger, \boldsymbol{\delta\xi}) = \frac{1}{2\mu_0}\int |\boldsymbol{\delta B}|^2\ \mathrm{dV} \tag{2.14c}$$

As can be observed from Eqn.2.14b and Eqn.2.14c, the contribution of the vacuum potential perturbation is always stabilising since magnetic energy is added to the system, while the surface potential perturbation can be either stabilising or destabilising, since a definite non-negative lower bound depends on the jump of the curvature. The plasma potential perturbation is separated

into stabilising and potentially destabilising contributions and a summary of each term is given below.

- $|\boldsymbol{\delta B}_\perp|^2/\mu_0$: The shear Alfven wave (SAW) is always stabilising representing energy spent to bend the field lines.
- $(B^2/\mu_0)|\nabla \cdot \boldsymbol{\delta\xi}_\perp + 2\boldsymbol{\kappa} \cdot \boldsymbol{\delta\xi}_\perp|^2$: The compressional Alfven wave (CAW) is always stabilising representing energy spent to compress the magnetic field.
- $\Gamma p|\nabla \cdot \boldsymbol{\delta\xi}|^2$: The fluid pressure compressional wave (CPW) is always stabilising representing energy spent to compress the fluid.
- $-(\boldsymbol{J \cdot B}/B^2)(\boldsymbol{\delta\xi}_\perp^\dagger \times \boldsymbol{B}) \cdot \boldsymbol{\delta B}_\perp$: Potentially destabilising contribution representing instabilities driven by the existence of a parallel current density (kink/peeling instability).
- $-2(\boldsymbol{\delta\xi}_\perp \cdot \nabla p)(\boldsymbol{\delta\xi}_\perp^\dagger \cdot \boldsymbol{\kappa})$: Potentially destabilising contribution representing instabilities driven by the synergistic work of fluid pressure gradient and magnetic curvature (interchange and ballooning instability).

It becomes apparent from the plasma potential perturbations that the equilibrium system will be most unstable or least stable to perturbations that minimise stabilising contributions. Considering that displacing the plasma from its original equilibrium usually leads to field line bending, the minimisation of CAW and CPW typically leads to the most unstable modes. The minimisation of CPW minimises the potential energy with respect to the parallel displacement. Therefore, for a certain perpendicular displacement, the parallel displacement is chosen such that $\nabla \cdot \boldsymbol{\delta\xi} = 0$. Moreover, the minimisation of the CAW provides a relationship between the normal and binormal component of the plasma displacement. This leads to further simplification of the plasma potential perturbation and in fact to the minimisation of surface potential energy perturbation.

After the minimisation of CPW in ideal MHD, the parallel displacement becomes redundant in the minimisation of δW. Although, its existence can still affect the linear growth rate of instabilities due to its contribution in δK, where in general leads to a reduction of the growth rate. The effect of

parallel displacement and compressibility on the ideal MHD stability can still be approximated by scaling the growth rate by a factor of $1/\sqrt{1+2q^2}$ [91]. For this reason, the exclusion of the parallel displacement from the kinetic energy provides an upper bound for the growth rate of the unstable mode without affecting the marginal stability of the system. In this thesis, the incompressible and perpendicular ideal MHD stability is considered.

At this stage the perpendicular displacement $\boldsymbol{\delta\xi}_\perp$ can be projected onto a coordinate system with respect to the normal $\boldsymbol{n} = \nabla\psi/|\nabla\psi|$ and binormal $\boldsymbol{t} = (\boldsymbol{B}\times\nabla\psi)/(B|\nabla\psi|)$ vectors with respect to the magnetic field $\boldsymbol{B}$, such that

$$\boldsymbol{\delta\xi}_\perp = \frac{X}{|\nabla\psi|}\boldsymbol{n} + U\frac{|\nabla\psi|}{B}\boldsymbol{t} \tag{2.15}$$

Substituting $\boldsymbol{\delta\xi}_\perp$ into δW_p and δK while minimising the CAW and CPW leads to

$$\begin{aligned}\delta W_p =& \frac{1}{2\mu_0}\int\{\frac{B^2}{|\nabla\psi|^2}|(\boldsymbol{b}\cdot\nabla)X|^2 + |\nabla\psi|^2|(\boldsymbol{b}\cdot\nabla)U|^2 \\ &- 2(\boldsymbol{\tau}\cdot\boldsymbol{n})[\frac{SB^2}{|\nabla\psi^2|}|X|^2 - 2\mathrm{Re}\{(\boldsymbol{B}\cdot\nabla)UX^\dagger\}] \\ &- 2(\boldsymbol{\kappa}\cdot\boldsymbol{n})\mu_0\frac{\partial_\psi p}{|\nabla\psi|}|X|^2\}\,\mathcal{J}\mathrm{d}\psi\mathrm{d}\theta\mathrm{d}\phi\end{aligned} \tag{2.16a}$$

$$\delta K = \frac{1}{2}\int\rho[\frac{1}{|\nabla\psi|^2}|X|^2 + \frac{|\nabla\psi|^2}{B^2}|U|^2]\,\mathcal{J}\mathrm{d}\psi\mathrm{d}\theta\mathrm{d}\phi \tag{2.16b}$$

$$[\frac{B_\phi}{B^2}(\boldsymbol{B}\cdot\nabla) - \partial_\phi]U = [\partial_\psi + G]X \tag{2.16c}$$

where $G = [\partial_\psi \ln(\mathcal{J}B^2) + \dfrac{2\mu_0\partial_\psi p}{B^2}]$, $S = \boldsymbol{t}\cdot\nabla\times\boldsymbol{t}$ is the local shear, $\boldsymbol{\kappa} = \boldsymbol{b}\cdot\nabla\boldsymbol{b} = \kappa_n\boldsymbol{n} + \kappa_s\boldsymbol{t}$ is the magnetic curvature and $\boldsymbol{\tau} = -\boldsymbol{b}\cdot\nabla\boldsymbol{t} = \tau_n\boldsymbol{n} + \tau_s\boldsymbol{t}$ is the local torsion. The normal component of the local torsion is related to the local shear and parallel current density by $(S - \mu_0 J_{||}/B) = -2\tau_n$, where $J_{||} = \boldsymbol{J}\cdot\boldsymbol{b}$.

2.4 Ballooning Instability

The drive mechanism of these instabilities stems from the relation between the pressure gradient and the magnetic curvature. In the inner or high field side (HFS) of the torus the curvature is antiparallel to the pressure gradient leading to stabilisation of perturbations. However, in the outer or low field side (LFS) of the torus the curvature is parallel to the pressure gradient so perturbations are not stabilised. The growth of such modes will then depend on the competition of the pressure drive and the stabilising field line bending that arises from the perturbation. For that reason ballooning modes are localised at the LFS of the torus attaining a field-aligned structure that minimises magnetic field line bending.

As such ballooning modes are structures of a long wavelength along a field line while the wavelength perpendicular to the field line is small. Considering the minimisation of CAW, it can be concluded that the perpendicular divergence of the displacement is the dominant term since $k_\perp \gg k_{||}$ and $k_\perp \gg |\boldsymbol{\kappa}|$. Therefore, the displacement is normal to the perpendicular number $\boldsymbol{k}_\perp \cdot \boldsymbol{\delta\xi}_\perp \sim 0$ leading to a relation between normal and binormal displacement,

$$U \sim -\frac{k_n}{k_s} X \tag{2.17}$$

where $\boldsymbol{k}_\perp = k_n|\nabla\psi|\boldsymbol{n} + k_s B/|\nabla\psi|\boldsymbol{t}$. In fact, for such perturbations to leading order current driven instabilities lead to no contribution and can be dropped from the analysis. Considering the localised nature of the ballooning structure typically those instabilities are internal, where the displacement tends to zero as the plasma boundary is approached. Therefore, considering the plasma potential perturbation δW_p and performing some algebraic manipulation Eqn.2.16 becomes,

$$\begin{aligned}\delta W_p =& \frac{1}{2\mu_0}\int \{k_\perp^2|(\boldsymbol{b}\cdot\nabla)Y|^2 - 2\mu_0\partial_\psi p(\frac{\kappa_n}{|\nabla\psi|}k_s^2 - \frac{\kappa_s|\nabla\psi|}{B}k_n k_s)|Y|^2 \\ &- [2\tau_n\frac{SB^2}{|\nabla\psi|^2}k_s^2 + (\boldsymbol{B}\cdot\nabla)Sk_n k_s]|Y|^2\}\,\mathcal{J}\mathrm{d}\psi\mathrm{d}\theta\mathrm{d}\phi\end{aligned} \tag{2.18a}$$

$$\delta K = \frac{1}{2}\int (\frac{\rho k_\perp^2}{B^2})|Y|^2\, \mathcal{J}\mathrm{d}\psi\mathrm{d}\theta\mathrm{d}\phi \tag{2.18b}$$

where $Y = X/k_s$ represents the total perpendicular displacement and $\boldsymbol{B}\cdot\nabla(J_{||}/B) = 2\partial_\psi p\boldsymbol{\kappa}\cdot\boldsymbol{t}|\nabla\psi|/B$ is used. The first and second terms in Eqn.2.18 are of order $\mathcal{O}(1)$, while the last term is of order $\mathcal{O}(\epsilon)$ and is dropped from the analysis. The function Y that minimises Eqn.2.18 can be obtained through Euler-Lagrange minimisation with respect to $(Y, \partial_l Y)$ leading to the local ballooning equation,

$$\partial_l(k_\perp^2\partial_l Y) - 2\mu_0\partial_\psi p(\frac{\kappa_n}{|\nabla\psi|}k_s^2 - \frac{\kappa_s|\nabla\psi|}{B}k_n k_s)Y = -\omega^2(\frac{\mu_0\rho}{B^2}{k_\perp}^2)Y \tag{2.19}$$

where $\boldsymbol{b}\cdot\nabla = \partial_l$ and $k_\perp^2 = k_n^2|\nabla\psi|^2 + k_s^2(B/|\nabla\psi|)^2$ is considered. In the limit where equilibrium quantities acquire a single helicity of $N > 1$, i.e. are described by a single toroidal mode number, and the non-axisymmetric parameter Δ of the equilibrium is small compared to the axisymmetric length-scale R, a simplified equation arises that provides physical insight, called the $s-\alpha$ model, and according to Hegna *et al.* [92]

$$\frac{\partial}{\partial\eta}(1+\Lambda^2)\frac{\partial}{\partial\eta}\xi_\perp + \alpha[\cos(\eta) + \Lambda\sin(\eta)]\xi_\perp = -\Omega^2(1+\Lambda^2)\xi_\perp \tag{2.20a}$$

$$\Lambda(\eta,\chi) = \int_{\eta_k}^{\eta}[s - \alpha\cos(\eta) + \tau\cos(2\eta) + \delta\cos(k\eta + k\chi)]\,\mathrm{d}\eta \tag{2.20b}$$

where $|k_\perp|^2 \propto (1+\Lambda^2)$, Λ contains the magnetic shear, $\alpha = -\partial_\psi p(2\rho V\Delta/R)[N^2/(N-1/q)^2]$ is the normalised pressure gradient, $s = \partial_\psi q[R\rho^2/V(N-1/q)]$ is the normalised global shear, $\Omega^2 = \omega^2\mu_0\rho V^2/(N-1/q)^2$ is the normalised eigenvalue of the system, $k = N/(N-1/q)$, $\tau = (N\Delta/R)^2$, $\delta = 4\Delta R[N/(N-1/q)]$ and the angles $(\eta,\chi) = (N\phi - \theta, \theta - \phi/q)$. In the case where $\delta = \tau = 0$ the original toroidal $s-\alpha$ model of Connor *et al.* [93] is obtained.

In an axisymmetric system, the $s-\alpha$ model provides a simplified but physical understanding of ballooning mode stability and the identification of the $s-\alpha$ boundary of stability, an example of which is illustrated in Fig.2.4a. A

counterintuitive feature of ballooning stability is the existence of a second region of stability at low global shear and high pressure gradient. At high global shear, shear stabilisation from the Λ^2 term, in the field line bending part of Eqn.2.20, stabilises the ballooning mode at low pressure gradient. As the pressure gradient is increased the effect from the unfavourable curvature overcomes field line bending and the instability occurs. On the other hand at low global shear, a second region of stability emerges due to the contribution of the pressure gradient to field line bending through modification of the current density. Effectively, field line bending stabilisation is amplified at the LFS of the torus due to increase of the local shear, stabilising the ballooning mode at high pressure gradient region. For an H-mode plasma this behaviour can be beneficial as the pedestal is a region of steep pressure gradient and high current density (low magnetic shear) facilitating access to second stability. However, at high current density and high $\beta = 2\mu_0 p/B^2$, current driven and external current and pressure driven instabilities can lead to unstable peeling-ballooning modes that halt the performance of a fusion plasma due to the destabilisation of ELMs.

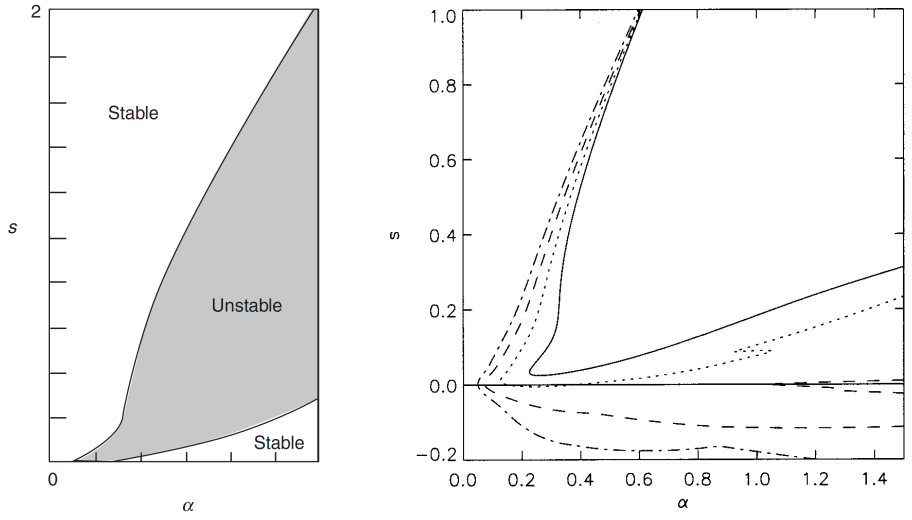

(A) (B)

FIGURE 2.4: (A) Schematic of the $s - \alpha$ model for a circular large-aspect ratio toroidal plasma illustrating the two regions of ballooning stability [94]. (B) Schematic of the $s - \alpha$ model for a quasi-axisymmetric toroidal plasma indicating the degradation of ballooning stability, where the solid line represents the axisymmetric case and the dotted lines the non-axisymmetric case [92].

In a 3D geometry a more complicated behaviour arises. Fig.2.4b illustrates

the $s - \alpha$ diagram of a quasi-axisymmetric system and the main feature that emerges is the degradation of both regions of stability. At high magnetic shear, the contribution of the local helical shear is small and no main difference from the axisymmetric case is observed. However at low shear, the mode is pushed toward regions of unfavourable curvature. The helicity of the local shear and unfavourable curvature allows localised regions where small local shear coexists with the regions of unfavourable curvature leading to destabilisation of specific field lines. This effect degrades the first region of stability and access to second stability. However, for highly localised modes a global analysis might be required to determine actual operational stability boundaries, but this analysis becomes complicated. Asymptotic WKB theory has been applied to determine the global structure of ballooning modes, but the resulting eigenmodes are found to be singular [95]. For that reason, local infinite-n ballooning analysis might be misleading or insufficient to determine the global stability of a 3D plasma.

2.5 High-β Kink/Peeling Instability

The kink instability is driven by the parallel current density and is associated with a "kink" of the magnetic flux surfaces. Depending on the poloidal spectrum of the perturbation, the instability is associated with the internal modes when the safety factor at the core is $q \sim 1$. The internal kink instability poses a limiting performance factor due to its connection with the sawtooth instability and increased temperature transport as well as a plasma disruption. However, considering a ballooning ordering, internal kink modes are found to be marginally stable for highly localised modes. As the lower order perturbation minimises magnetic compression the displacement is expressed as $\boldsymbol{\delta\xi}_\perp \sim \delta\xi_\perp(\boldsymbol{b} \times \boldsymbol{k}_\perp)$ and the normal magnetic field becomes $\boldsymbol{\delta B}_\perp \sim [\boldsymbol{b} \cdot \nabla(\delta\xi_\perp B)](\boldsymbol{b} \times \boldsymbol{k}_\perp)$. As a result the kink drive is proportional to $(\boldsymbol{\delta\xi}_\perp \times \boldsymbol{b}) \cdot \boldsymbol{\delta B}_\perp \sim 0$. On the other hand, considering modes where $k_s \gg k_n$, such that the localised condition is relaxed, kink instabilities can occur even for $q > 1$ [96]. Considering this difference a local kink equation can be derived such that,

$$\partial_{ll}Y - 2(\mu_0 \partial_\psi p \frac{\kappa_n}{|\nabla\psi|} + \tau_n \frac{SB^2}{|\nabla\psi|^2})Y = -\omega^2(\frac{\mu_0\rho}{B^2})Y \tag{2.21}$$

Apart from the internal kink mode, instabilities can also arise when coupling with the vacuum field is considered, leading to the external kink instability. In particular Eqn.2.14b is related to the existence of a finite pressure and a parallel current discontinuity at the plasma-vacuum interface that stems from the jump in the normal gradient of the equilibrium magnetic field, when coupling with the vacuum field is considered,

$$\delta W_s = \frac{1}{2}\int |X|^2[(\frac{\tilde{\kappa}_n + \kappa_n}{2})p + (\frac{\tilde{B}^2 + B^2}{2\mu_0})(\tilde{\kappa}_n - \kappa_n)]\ \mathrm{dS} \tag{2.22}$$

where the total pressure continuity $2\mu_0 p + B^2 = \tilde{B}^2$ is used. The connection of the parallel current density to the normal curvature is complicated for a non-axisymmetric geometry. Although, a simple expression can be derived considering the incompressibility of the the current density and its relation to pressure gradient and curvature,

$$\kappa_n = \frac{\boldsymbol{b}\cdot\nabla(J_{||}/B)}{2|\nabla\psi|^2\kappa_s} - \frac{\partial_\psi \ln B}{|\nabla\psi|^2} \tag{2.23}$$

In addition, it is worth mentioning that Eqn.2.22 contains a pressure dependent term, which is always destabilising at the outboard side of the torus since normal curvature is negative, limiting the maximum achievable pressure. Both contributions can lead to an external kink or peeling instability and coupling with ballooning modes, even though core kink modes are marginally stable, provided that the surface contribution exceeds the volume field line bending.

2.6 Coupled Peeling-Ballooning Model

In axisymmetric tokamaks plasmas, the onset of large type-I ELMs is attributed to ideal MHD instabilities. Experimental observations indicate that the plasma can sit on the ballooning stability boundary for several Alfvenic times and even exceeded it without the observation of an ELM crash [97], [98]. In addition, ballooning modes are radially highly localised structures at the plasma edge

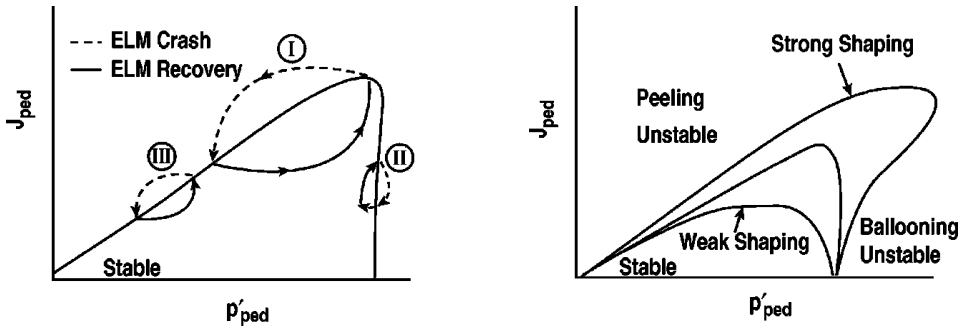

(A) (B)

FIGURE 2.5: (A) An illustration of the peeling-ballooning stability boundary and ELM cycle in a tokamak plasma and (B) an example of how plasma shaping can increase stability of ideal MHD modes, as a function of the average pedestal parallel current density $J_{||}$ and pressure gradient p'. [33]

and since those modes pass through marginal stability their initial growth is small rather than explosive. For that reason, coupling to kink modes was suggested as a way to increase the radial extent of the perturbation, leading to more particles and heat being expelled.

The coupling between kink/peeling-ballooning modes occurs in high-β plasmas as internal kink modes are usually found to be marginally stable and external kink/peeling modes are driven by the finite edge parallel current density and pressure. The coupling of the two instabilities leads to the so called $J_{||} - p'$ diagram, which is illustrated in Fig.2.5a, and represents an extension of the $s-\alpha$ model introduced earlier. Type-I ELMs are experimentally found in the nose of the stability diagram, where both pressure gradient and parallel current density is large [99]. In addition, a reduction or even loss of second ballooning stability access is observed. Careful plasma shaping allows an increase in the achievable parallel current and pressure gradient, as depicted in Fig.2.5b. In particular, the introduction of triangularity stabilises external kink modes especially in the case where a divertor configuration is introduced. The elliptic shape of the plasma boundary is shown analytically and computationally to lead to the stabilisation of external kink modes that allows increased plasma stability. An example is a D-shape tokamak plasma given in Fig.2.6, where the growth rate and mode structure of peeling-ballooning modes is illustrated. For such plasmas, the existence of a finite current density at the plasma edge leads to kink-like modes for low toroidal mode numbers n, that transition to

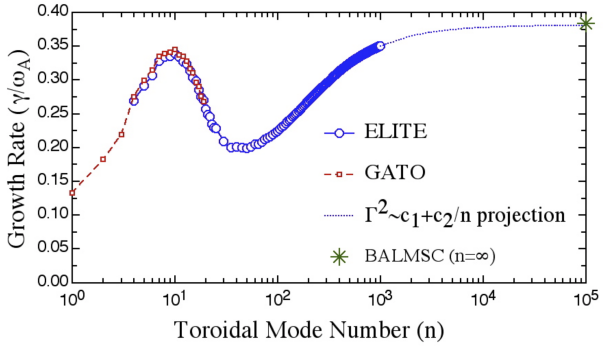

(A)

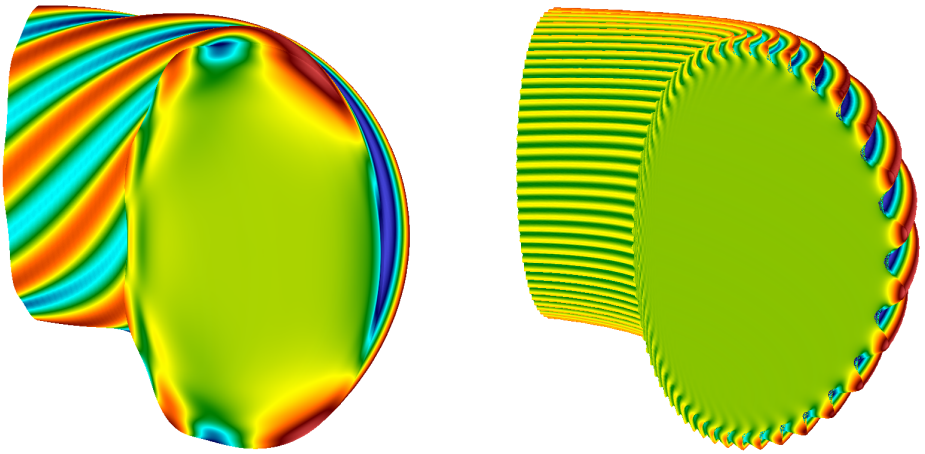

(B) (C)

FIGURE 2.6: (A) A typical growth rate γ/ω_A spectrum as a function of toroidal mode number n of the peeling-ballooning instability [100]. (B) The mode structure of a low n external kink/peeling mode. (C) The mode structure of a high n ballooning mode. The ideal MHD stability code ELITE was used for the calculation of the growth rate and mode structure.

ballooning-like modes for higher n. In the growth rate spectrum, kink modes represent the peak centred around $n \sim 10$ and ballooning modes for $n > 30$.

The success of the coupled peeling-ballooning model to explain the onset of type-I ELMs in tokamak plasmas led to the formulation of EPED model [101], [102]. This model introduced additional stability considerations from kinetic ballooning modes (KBMs) and diamagnetic stabilisation. KBMs are fluid-like ballooning modes, where kinetic diamagnetic stabilisation is included along with additional destabilisation kinetic effects. These are proposed to be responsible for halting the pedestal pressure gradient as the pedestal pressure is increased. A good approximation for KBMs is given by local ideal MHD ballooning analysis, which is often used because of computational efficiency.

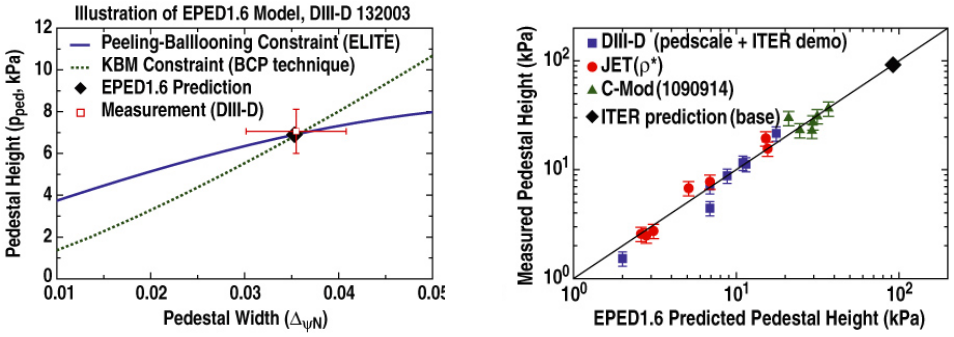

(A) (B)

FIGURE 2.7: (A) A comparison of the pedestal pressure and width at the point of the ELM as predicted by EPED and measured in the DIII-D tokamak. (B) A comparison of the predicted pedestal pressure at the point of the ELM between EPED predictions and measured data in a number of tokamaks. [101]

According to this model the ELM crash occurs when the pedestal pressure height and width is such that unstable finite n PB modes become unstable, predicting a relation between the achievable pedestal pressure and width Δ that scales as $\sqrt{\beta_p} \propto \Delta$, where $\beta_p = 2\mu_0 p/B_p^2$. Fig.2.7 shows a comparison of the EPED model with experimental data from various tokamaks.

In a non-axisymmetric tokamak, i.e. a case where an MP field is applied, the behaviour of the plasma becomes more complex. As discussed in the previous section, infinite n or local ballooning analysis indicates that due to changes in local shear and curvature, particular field lines are further destabilised leading to poloidal localised ballooning modes [70], [71]. However, external kink/peeling modes can be either destabilised or stabilised depending on the spectrum of the applied field and the resulting jump in the non-axisymmetric normal curvature. Especially for the case where kink stabilisation occurs, a similar scenario is observed with the stabilisation of external kink modes due to the presence of an ideal wall surrounding the plasma. The existence of an ideal wall drives a current sheet at the wall surface creating a magnetic field that opposes the perturbed magnetic field and constraining the plasma motion. Recent investigation from AUG suggest that density pump-out is required [50] for density control and reduction of pressure gradients below global MHD stability limits. Although, mitigated and suppressed states occur at similar regions of the 2D $J - p'$ diagram [77], they required different plasma shape and in particular triangularity. Triangularity increases the stability of kink modes, such that the postulated degradation of the MHD stability boundary from the

3D effects and corrugation of the flux surfaces keeps the plasma in a stable operational regime.

Very little literature exists with respect to the stability of medium to high n peeling-ballooning modes when MPs are applied. In recent years, progress has been achieved in the development of a 3D high n peeling-ballooning theory [103] leading to the development of the PB3D code [81], as an extension of the original 2D high n peeling-ballooning theory that the ELITE code is based on. However, the developed tools have not yet been applied to study the plasma stability under the application of MPs. Moreover, existing global 3D stability codes [78], [79], [80] are typically used for the examination of low n modes, which are not relevant to ELM related instabilities. In this work, an alternative route is followed for the examination of the 3D plasma stability. Using analytical tools of perturbation and variational theory, the ELITE code is used within a numerical framework that calculates the ideal linear plasma response, assuming knowledge of the plasma surface normal displacement, and using the axisymmetric peeling-ballooning normal modes as basis functions to study the 3D system.

2.7 ELITE

ELITE [82] is a spectral eigenvalue linear stability code for axisymmetric ideal MHD systems, and in this work the low n version of ELITE is used [83]. The coordinate system under consideration is the poloidal straight field line system $\{\psi, \theta^*, \phi\}$ that allows an efficient Fourier decomposition in the poloidal and toroidal direction, such that for a certain toroidal mode n

$$X_n(\psi, \theta^*, \phi) = \sum_m X_{nm}(\psi) e^{-i(m\theta^* - n\phi)} \tag{2.24}$$

The high n version of ELITE uses the extended ballooning ordering, accurate to second order in powers of n^{-1} as introduced by [93], retaining both ballooning and kink terms in the plasma potential energy change. The expansion in powers of n^{-1} allows an algebraic relation between the normal and binormal displacement significantly reducing the complexity of the system. Considering that the CAW needs to minimised, to zeroth order the divergence of the

perpendicular displacement needs to vanish, as described previously for an edge localised ballooning type of mode, leading to the relation,

$$U_n^{(0)} \sim \frac{i}{n}\partial_\psi X_n^{(0)} \tag{2.25}$$

where $\boldsymbol{B}\cdot\nabla \ll \partial_\phi$, $G \ll \partial_\psi$ and $\partial_\phi = in$ is considered. In order to retain higher order terms, the zeroth order relation Eqn.2.25 can be substituted in Eqn.2.16c as an approximation for $(\boldsymbol{B}\cdot\nabla)U$, giving the final relation between the normal and binormal component to second order in n^{-1}, that is:

$$U \simeq \frac{i}{n}(\partial_\psi X + GX) + \frac{1}{n^2}[\frac{B_\phi}{B^2}(\boldsymbol{B}\cdot\nabla)\partial_\psi X] \tag{2.26}$$

Although such a formalism is sufficient for the stability of typical ballooning unstable plasmas, it is not necessarily sufficient for low n high-β kink unstable plasmas or for the calculation of the low n plasma response to external 3D fields. In order to be able to simulate such phenomena, the low n version of ELITE assumes no expansion in n and directly solves Eqn.2.16c. In practice this leads to a matrix problem due to the knowledge of the differential operators in the $\{\theta^*,\phi\}$ direction. Considering that $\partial_\phi = in$ and $\partial_{\theta^*} = -im$, the matrix problem becomes,

$$U_m = A^{-1}_{mm'}[d_\psi + G_{mm'}]X_{m'} \tag{2.27}$$

where $G_{mm'} = \mathcal{F}\{\partial_\psi \ln(\mathcal{J}B^2) + \frac{2\mu_0\partial_\psi p}{B^2}\}_m$ and $A_{mm'} = -i[(m' - nq)\mathcal{F}\{B_\phi/\mathcal{J}B^2\}_m + n]$. Substituting Eqn.2.27 into Eqn.2.16 allows the system to be minimised with respect to a single variable, X_n. Some algebraic manipulation that involves integration by parts between conjugate and non-conjugate terms, results in a quadratic form for the energy equation such that,

$$\begin{aligned} WV_{mm'} = &[WV^2_{mm'}\mathrm{d}_{\psi\psi} + WV^1_{mm'}\mathrm{d}_\psi + WV^0_{mm'}] \\ &+ [WS^1_{mm'}\mathrm{d}_\psi + WS^0_{mm'} + VS^0_{mm'}]\delta(\psi-\psi_a) \end{aligned} \tag{2.28a}$$

$$\begin{aligned} KV_{mm'} = &[KV^2_{mm'}\mathrm{d}_{\psi\psi} + KV^1_{mm'}\mathrm{d}_\psi + KV^0_{mm'}] \\ &+ [KS^1_{mm'}\mathrm{d}_\psi + KS^0_{mm'}]\delta(\psi-\psi_a) \end{aligned} \tag{2.28b}$$

$$\langle X_m|WV_{mm'}|X_{m'}\rangle = \omega_n^2\langle X_m|KV_{mm'}|X_{m'}\rangle \tag{2.28c}$$

where $\langle X_m|A_{mm'}|X_{m'}\rangle = \sum_{m,m'}\int X_m^\dagger A_{mm'}X_{m'}\mathrm{d}\psi$, WV^i and KV^i are the matrix elements from the contribution of the plasma potential and kinetic energy respectively in the plasma volume; here WS^i and KS^i are the matrix elements from the contribution of the plasma potential and kinetic energy respectively in the plasma surface and VS^i are the matrix elements from the contribution of the vacuum potential energy in the plasma surface. Eqn.2.28 can be minimised with respect to X_m leading to a system of second order differential equations,

$$[A_{mm'}\mathrm{d}_{\psi\psi} + B_{mm'}\mathrm{d}_\psi + C_{mm'}]X'_m = 0 \tag{2.29}$$

ELITE solves a boundary condition at the plasma-vacuum interface to assure that the solution satisfies total pressure continuity and minimises the surface contribution, and iterates until a pure imaginary eigenvalue is found that simultaneously satisfies a core boundary condition $\{X_m(\psi_0)\} = 0$.

Finally, in order to increase time efficiency of the calculation ELITE uses two grids. The time consuming calculation of the matrix coefficients $A_{mm'}$, $B_{mm'}$, $C_{mm'}$, that depend only on equilibrium quantities, uses a coarse grid as radial variation of equilibrium quantities is slow with respect to the perturbed displacement X_m. The perturbed displacement X_m is calculated via a shooting method on a fine grid which is packed around rational surfaces, since for intermediate to high n modes X_m is a highly localised function around the corresponding rational surface $q = m/n$. Therefore, the matrix coefficients need to be interpolated from the coarse to the fine grid during the calculation. As they include radial derivatives up to second order, finite difference calculation and interpolation of derivatives can introduce numerical errors. In order to accurately calculate the radial derivatives, ELITE uses the Mercier-Luc formalism [104] where the radial derivatives of equilibrium quantities are analytically related to equilibrium quantities on the flux surface through the Grand-Safranov equation. As a result, the exact calculation of radial derivatives and their interpolation leads to a far more accurate numerical scheme assuring convergence of the solution.

Chapter 3

Plasma Stability of Non-Axisymmetric Systems

3.1 3D Ideal MHD Stability of Tokamak Plasmas

In order to examine the stability of tokamak plasmas under the application of external non-axisymmetric magnetic perturbations of toroidal mode number N, two methods are taken into consideration. The first method uses perturbation theory on the stability of the axisymmetric system. The impact of the external fields is treated as a perturbation on the original system due to the fact that those applied fields are orders of magnitude smaller. Such an analysis results in correction terms for the mode structure and growth rate of the perturbation, approximating the true non-axisymmetric normal mode. The benefit of this method is that it results in closest neighbour toroidal mode coupling leading to triplet modes $\{n - N, n, n + N\}$ significantly simplifying the complexity of non-axisymmetric stability, in contrast to toroidal mode families [105] which takes place in the full 3D stability calculation. In addition, all correction terms are functions of equilibrium quantities and axisymmetric normal modes, which can be computed efficiently with existing axisymmetric stability codes.

The second method is based on the variational formulation of the energy principle. The stability problem results in a generalised eigenvalue problem of the force operator and the stability of the system will depend on the eigenvalues of this operator. Variational approaches allow the use of orthogonal basis

functions for the representation of the plasma displacement and provide a method that determines an appropriate superposition that minimises potential energy, providing in such a way the most unstable mode that can be produced from the particular basis set. Considering that the applied fields are much smaller than equilibrium fields, the axisymmetric normal modes are postulated to serve as appropriate trial functions for energy minimisation. Although this is an approximate normal mode, the exact normal modes will only be more unstable.

In this chapter, the theory and procedure under which non-axisymmetric stability is studied is described, and the numerical framework based on the axisymmetric stability code ELITE under which that calculation is performed is presented.

3.1.1 Non-axisymmetric Stability using Perturbation Theory

The applied non-axisymmetric magnetic perturbations under consideration are typically much smaller than axisymmetric equilibrium quantities, such that it is a reasonable assumption that resulting forces produced from the non-axisymmetric equilibrium are also small in comparison to axisymmetric forces. As a result, perturbation theory can be used to provide an approximate solution to Eqn.(2.12). Such a perturbative stability analysis has been performed to first order in [106] to approximate changes in axisymmetric stability due to the presence of narrow island structures. However, second order corrections, as in [76], are required to capture perturbative non-axisymmetric effects. First, consider the momentum equation normalised to the mass density ρ,

$$\mathbf{F}\boldsymbol{\delta\xi}_n = \frac{\partial^2}{\partial t^2}\boldsymbol{\delta\xi}_n \Rightarrow (\mathbf{F}^{(0)} + \epsilon\mathbf{F}^{(1)} + \epsilon^2\mathbf{F}^{(2)} + ...)\boldsymbol{\delta\xi}_n = -\omega_n^2\boldsymbol{\delta\xi}_n \tag{3.1}$$

produced from a plasma displacement $\boldsymbol{\delta\xi}_n$, where $\mathbf{F}^{(0)}$ is a force operator due to the axisymmetric equilibrium, $\mathbf{F}^{(k)}$ is a force operator due to axisymmetric and non-axisymmetric equilibrium changes of order k and ϵ represents a small parameter proportional to $B_N^{(1)}/B_0^{(0)} \ll 1$, typically $B_N^{(1)}/B_0^{(0)} \sim 10^{-3}$. Eqn.(3.1) represents an eigenvalue equation, where the set of $-\omega_n^2$ and $\boldsymbol{\delta\xi}_n$ represent the eigenvalues (frequency or growth rate) and eigenfunctions (perpendicular displacement) respectively. Due to the perturbative nature of the higher order

contributions, the eigenvalues and eigenvectors can be expanded in the small parameter ϵ:

$$\omega_n^2 = \omega_n^{(0)2} + \epsilon\omega_n^{(1)2} + \epsilon^2\omega_n^{(2)2} + ... \tag{3.2}$$

$$\boldsymbol{\delta\xi}_n = \boldsymbol{\delta\xi}_n^{(0)} + \epsilon\boldsymbol{\delta\xi}_n^{(1)} + \epsilon^2\boldsymbol{\delta\xi}_n^{(2)} + ... \tag{3.3}$$

Solving order by order, we derive to $k \leq 2$,

$$\underline{0^{\text{th}}\text{ Order:}}\ \mathbf{F}^{(0)}\boldsymbol{\delta\xi}_n^{(0)} = -\omega_n^{(0)2}\boldsymbol{\delta\xi}_n^{(0)} \tag{3.4}$$

$$\underline{1^{\text{st}}\text{ Order:}}\ \mathbf{F}^{(1)}\boldsymbol{\delta\xi}_n^{(0)} + \mathbf{F}^{(0)}\boldsymbol{\delta\xi}_n^{(1)} = -\omega_n^{(1)2}\boldsymbol{\delta\xi}_n^{(0)} - \omega_n^{(0)2}\boldsymbol{\delta\xi}_n^{(1)} \tag{3.5}$$

$$\underline{2^{\text{nd}}\text{ Order:}}\ \mathbf{F}^{(2)}\boldsymbol{\delta\xi}_n^{(0)}+\mathbf{F}^{(1)}\boldsymbol{\delta\xi}_n^{(1)}+\mathbf{F}^{(0)}\boldsymbol{\delta\xi}_n^{(2)} = -\omega_n^{(2)2}\boldsymbol{\delta\xi}_n^{(0)}-\omega_n^{(1)2}\boldsymbol{\delta\xi}_n^{(1)}-\omega_n^{(0)2}\boldsymbol{\delta\xi}_n^{(2)} \tag{3.6}$$

The unperturbed system

$$\mathbf{F}^{(0)}\boldsymbol{\delta\xi}_n^{(0)} = -\omega_n^{(0)2}\boldsymbol{\delta\xi}_n^{(0)} \tag{3.7}$$

is considered to be unstable and non-degenerate, i.e. $\omega_n^{(0)} \neq \omega_m^{(0)}$ for $n \neq m$. Thus, the eigenvalues $-\omega_n^{(0)2}$ and eigenfunctions $\boldsymbol{\delta\xi}_n^{(0)}$ are fully determined for a range of n and can be used as basis functions for the solution of higher order equations. These basis functions are orthogonal, and considered to be normalised such that $\langle\boldsymbol{\delta\xi}_m^{(0)}|\boldsymbol{\delta\xi}_n^{(0)}\rangle = \int \boldsymbol{\delta\xi}_m^{*(0)} \cdot \boldsymbol{\delta\xi}_n^{(0)}\mathcal{J}\mathrm{d}^3\mathbf{x} = \delta_{nm}$, where $\mathcal{J}$ is a weight function representing the Jacobian of the coordinate system.

To obtain first order corrections for the eigenvalues and eigenfunctions, the inner product of Eqn.(3.5) with $\boldsymbol{\delta\xi}_n^{(0)}$ is considered,

$$\langle\boldsymbol{\delta\xi}_n^{(0)}|\mathbf{F}^{(0)}|\boldsymbol{\delta\xi}_n^{(1)}\rangle + \langle\boldsymbol{\delta\xi}_n^{(0)}|\mathbf{F}^{(1)}|\boldsymbol{\delta\xi}_n^{(0)}\rangle = -\omega_n^{(0)2}\langle\boldsymbol{\delta\xi}_n^{(0)}|\boldsymbol{\delta\xi}_n^{(1)}\rangle - \omega_n^{(1)2}\langle\boldsymbol{\delta\xi}_n^{(0)}|\boldsymbol{\delta\xi}_n^{(0)}\rangle \tag{3.8}$$

The first terms on the left and right hand sides of Eqn.(3.8) cancel, due to the fact that $\mathbf{F}^{(0)}$ is Hermitian. This leads to a simple relation for the 1st order correction of the eigenvalue,

$$\omega_n^{(1)2} = -\langle\boldsymbol{\delta\xi}_n^{(0)}|\mathbf{F}^{(1)}|\boldsymbol{\delta\xi}_n^{(0)}\rangle \tag{3.9}$$

Taking the inner product of Eqn.(3.5) with $\boldsymbol{\delta\xi}_m^{(0)}$ $(m \neq n)$ leads to

$$(\omega_m^{(0)2} - \omega_n^{(0)2})\langle\boldsymbol{\delta\xi}_m^{(0)}|\boldsymbol{\delta\xi}_n^{(1)}\rangle = \langle\boldsymbol{\delta\xi}_m^{(0)}|\mathbf{F}^{(1)}|\boldsymbol{\delta\xi}_n^{(0)}\rangle \tag{3.10}$$

One can use the freedom in the solution to Eqn.(3.5) for $\boldsymbol{\delta\xi}_n^{(1)}$ to satisfy an orthogonality relation $\langle \boldsymbol{\delta\xi}_n^{(0)} | \boldsymbol{\delta\xi}_n^{(1)} \rangle = 0$. This allows the representation of the perturbed state as a superposition of the unperturbed states,

$$\boldsymbol{\delta\xi}_n^{(1)} = \sum_{m \neq n} \langle \boldsymbol{\delta\xi}_m^{(0)} | \boldsymbol{\delta\xi}_n^{(1)} \rangle \boldsymbol{\delta\xi}_m^{(0)} \tag{3.11}$$

Substituting Eqn.(3.11) into Eqn.(3.10) provides the first order correction of the eigenfunction that depends on known quantities,

$$\boldsymbol{\delta\xi}_n^{(1)} = \sum_{m \neq n} \frac{\langle \boldsymbol{\delta\xi}_m^{(0)} | \mathbf{F}^{(1)} | \boldsymbol{\delta\xi}_n^{(0)} \rangle}{(\omega_m^{(0)2} - \omega_n^{(0)2})} \boldsymbol{\delta\xi}_m^{(0)} \tag{3.12}$$

At this stage it can be noted that if the first order correction of the force operator $\mathbf{F}^{(1)}$ is non-axisymmetric, then the correction to the eigenfunction is non-zero $\boldsymbol{\delta\xi}_n^{(1)} \neq 0$, but there is no change to the eigenvalue, i.e. $\omega_n^{(1)2} = 0$. On the other hand, if the first order correction of the force operator $\mathbf{F}^{(1)}$ is axisymmetric, the opposite is expected. In addition, for a non-axisymmetric magnetic perturbation with a toroidal mode number N, a triplet mode emerges: $\{n - N, n, n + N\}$. This represents a truncation of the mode families that occurs in 3D equilibrium geometry and n is not anymore a "good"quantum number. This leads to a poloidal localisation of the 3D mode, provided the coupling is strong enough.

In order to calculate corrections to either the mode structure or the growth rate of peeling-ballooning modes due to the presence of 3D fields, second order corrections need to be considered. Repeating the above procedure for Eqn.(3.6), we derive:

$$\omega_n^{(2)2} = -\langle \boldsymbol{\delta\xi}_n^{(0)} | \mathbf{F}^{(2)} | \boldsymbol{\delta\xi}_n^{(0)} \rangle - \langle \boldsymbol{\delta\xi}_n^{(0)} | \mathbf{F}^{(1)} | \boldsymbol{\delta\xi}_n^{(1)} \rangle \tag{3.13}$$

The second order force operator $\mathbf{F}^{(2)}$ can be dropped from the analysis as it provides corrections due to axisymmetric changes, and substituting Eqn.(3.12) into Eqn.(3.13), the second order correction of the eigenvalue is explicitly expressed as,

$$\omega_n^{(2)2} = -\sum_{m \neq n} \frac{\langle \boldsymbol{\delta\xi}_n^{(0)} | \mathbf{F}^{(1)} | \boldsymbol{\delta\xi}_m^{(0)} \rangle \langle \boldsymbol{\delta\xi}_m^{(0)} | \mathbf{F}^{(1)} | \boldsymbol{\delta\xi}_n^{(0)} \rangle}{(\omega_m^{(0)2} - \omega_n^{(0)2})} = -\sum_{m \neq n} \frac{||\mathbf{F}_{nm}^{(1)}||^2}{(\omega_m^{(0)2} - \omega_n^{(0)2})} \tag{3.14}$$

For a single toroidal mode number N, Eqn.(3.12) and Eqn.(3.14) result in solely first neighbour coupling $m = n \pm N$, leading to the triplet mode $\{n - N, n, n + N\}$. Note that since the numerator of Eqn.(3.14) is always positive, for $\omega_m^{(0)2} > \omega_n^{(0)2}$ the contribution is stabilising, while for $\omega_m^{(0)2} < \omega_n^{(0)2}$ the contribution is destabilising. Most importantly, if the spectrum contains extrema, the most unstable mode will become more unstable and the most stable mode becomes more stable.

3.1.2 Non-axisymmetric Stability using Variational Theory

The ideal MHD system defines a hermitian stability problem that can efficiently be solved considering discrete normal modes, as explained in Chapter2. In the case where non-degenerate eigenvalues are considered $\omega_m^2 \neq \omega_n^2$ for $m \neq n$, the normal modes are orthogonal,

$$(\omega_m^2 - \omega_n^2)\langle \boldsymbol{\delta\xi}_m | \delta K | \boldsymbol{\delta\xi}_n \rangle = \frac{1}{2}[\langle \boldsymbol{\delta\xi}_m | \delta W | \boldsymbol{\delta\xi}_n \rangle - \langle \boldsymbol{\delta\xi}_n | \delta W | \boldsymbol{\delta\xi}_m \rangle] = 0 \tag{3.15}$$

and lead to $\langle \boldsymbol{\delta\xi}_m | \delta K | \boldsymbol{\delta\xi}_n \rangle = \int \boldsymbol{\delta\xi}_m^* \cdot \boldsymbol{\delta\xi}_n \rho \mathcal{J} \mathrm{d}\psi \mathrm{d}\theta \mathrm{d}\phi = 0$. The displacement under consideration is linear with respect to the normal displacement functional X_n, such that $\boldsymbol{\delta\xi}(c_n X_n) = c_n \boldsymbol{\delta\xi}(X_n)$. As a result, both the force and energy operators are linear with respect to the displacement and therefore the functional X_n, i.e. $\boldsymbol{F}(c_n X_n) = c_n \boldsymbol{F}(X_n)$ and $\delta W(c_m^* X_m^*, c_n X_n) = c_m^* c_n \delta W(X_m^*, X_n)$. In this way a generalised eigenvalue problem is constructed $\boldsymbol{c}^T(\boldsymbol{\delta W} - \omega^2 \boldsymbol{\delta K})\boldsymbol{c} = 0$.

In the case where the plasma equilibrium is axisymmetric, the energy functional results in a toroidally decoupled system due to the orthogonality of the toroidal basis functions, i.e. the toroidal Fourier harmonics.

$$\begin{aligned} \sum_m \sum_n \omega^2 c_m^* c_n \langle \boldsymbol{\delta\xi}_m | \delta K_0 | \boldsymbol{\delta\xi}_n \rangle &= \sum_m \sum_n c_m^* c_n \langle \boldsymbol{\delta\xi}_m | \delta W_0 | \boldsymbol{\delta\xi}_n \rangle \\ \sum_m \omega_m^2 \delta K_0 |c_m|^2 &= \sum_m \delta W_0 |c_m|^2 \end{aligned} \tag{3.16}$$

It becomes apparent from Eqn.(3.16) that no coupling of toroidal modes occurs and each $\boldsymbol{\delta\xi}_n$ corresponds to a normal mode of the axisymmetric system that can be used as basis functions to study the stability of the 3D system. As

such, a displacement can be expressed as a linear superposition of axisymmetric normal modes,

$$\boldsymbol{\delta\xi}(\psi,\theta,\phi) = \sum_n c_n \boldsymbol{\delta\xi}_n(\psi,\theta)e^{in\phi} = \sum_n c_n \boldsymbol{\delta\xi}_n(\psi,\theta)\Phi_n(\phi) \tag{3.17}$$

If non-axisymmetric fields are present, toroidal mode coupling occurs and the resulting system becomes,

$$\begin{aligned} \sum_{m,n} \omega^2 c_m^* c_n \langle \Phi_m | \delta K_0 | \Phi_n \rangle &= \sum_{m,n} c_m^* c_n \langle \Phi_m | \delta W_0 + \delta W_N | \Phi_n \rangle \\ \sum_m \omega_m^2 \delta K_0 |c_m|^2 &= \sum_m \delta W_0 |c_m|^2 \\ &\quad + \sum_{m,n} \delta W_N c_m^* c_n \delta_{mn\pm N} \end{aligned} \tag{3.18}$$

If the δW_N coefficients are small, weak coupling occurs and it is expected that the variational method is equivalent to a perturbative method. An advantage of the variational method is that it is not restricted to weak coupling as larger values of δW_N will result in strong or broadband coupling of toroidal modes. However, in both approaches the poloidal dependence of the toroidal normal mode remains fixed. As a result the applied magnetic field will not affect the coupling of the individual poloidal harmonics within each toroidal normal mode and the possible structure of the non-axisymmetric normal mode is significantly constrained. In order to resolve this issue, the individual poloidal Fourier harmonics of the axisymmetric normal modes can be taken into consideration for a displacement of the form,

$$\boldsymbol{\delta\xi}(\psi,\theta^*,\phi) = \sum_n \sum_l c_{n,l} \boldsymbol{\delta\xi}_{n,l}(\psi) e^{-i(l\theta^* - n\phi)} = \sum_n \sum_l c_{n,l} \boldsymbol{\delta\xi}_{n,l}(\psi)\Theta_l(\theta^*)\Phi_n(\phi) \tag{3.19}$$

For the axisymmetric system, such a representation results in a system of normal modes, where each is a superposition of poloidal Fourier modes due to poloidal inhomogeneity of the axisymmetric equilibrium,

$$\sum_{m,n}\sum_{k,l}\omega^2 c^*_{m,k}c_{n,l}\langle\Theta_k\Phi_m|\delta K_{0,s}|\Theta_l\Phi_n\rangle = \sum_{m,n}\sum_{k,l} c^*_{m,k}c_{n,l}\langle\Theta_k\Phi_m|\delta W_{0,s}|\Theta_l\Phi_n\rangle$$
$$\sum_{m}\sum_{k,l}\omega^2_m\delta K_{0,s}c^*_{m,k}c_{m,l}\delta_{kl\pm s} = \sum_{m}\sum_{k,l}\delta W_{0,s}c^*_{m,k}c_{m,l}\delta_{kl\pm s} \tag{3.20}$$

It is straight forward to derive an expression for the non-axisymmetric system, which becomes

$$\sum_{m,n}\sum_{k,l}\omega^2 c^*_{m,k}c_{n,l}\langle\Theta_k\Phi_m|\delta K_{0,s}|\Theta_l\Phi_n\rangle = \sum_{m,n}\sum_{k,l} c^*_{m,k}c_{n,l}\langle\Theta_k\Phi_m|\delta W_{0,s}+\delta W_{N,s'}|\Theta_l\Phi_n\rangle$$
$$\sum_{m}\sum_{k,l}\omega^2_m\delta K_{m,s}c^*_{m,k}c_{n,l}\delta_{kl\pm s} = \sum_{m}\sum_{k,l}\delta W_{0,s}c^*_{m,k}c_{n,l}\delta_{kl\pm s}$$
$$+\sum_{m,n}\sum_{k,l}\delta W_{N,s'}c^*_{m,k}c_{n,l}\delta_{mn\pm N}\delta_{kl\pm s'} \tag{3.21}$$

It can be observed from Eqn.(3.21) that the non-axisymmetric equilibrium will lead to non-uniform poloidal mode coupling of each toroidal normal mode and in the case where $\delta W_{N,s}$ is not much smaller than $\delta W_{0,s}$ or strong coupling occurs, the structure of each toroidal normal mode can change significantly. In principle, such a feature allows the decoupling of external kink/peeling modes to core ballooning modes, as the corresponding poloidal harmonics can change independently. In addition, in a tokamak plasma, elongation and triangularity lead to coupling of $\{m, m\pm1, m\pm2\}$ poloidal modes, whereas in a non-axisymmetric plasma additional shaping effects can significantly increase the number of coupled poloidal harmonics, indicating the importance of allowing freedom in the poloidal mode coupling of each axisymmetric toroidal normal modes.

3.2 Potential and Kinetic Energy Matrix Coefficients

The calculation of the potential and kinetic energy matrix coefficients requires knowledge of the perturbed force produced from the non-axisymmetric equilibrium. The matrix coefficients for the perturbative and variational

approach come from the same set of equations and the only difference occurs in the coupling of the individual basis. A straightforward relation exists between the two methods if the relative poloidal coupling of the axisymmetric normal modes remains unchanged, such that

$$F^{(1)}_{mn} = \frac{\langle \Phi_m | \delta W_N | \Phi_n \rangle}{\sqrt{\langle \Phi_m | \delta K_0 | \Phi_m \rangle \langle \Phi_n | \delta K_0 | \Phi_n \rangle}} \tag{3.22}$$

As a result, a single analysis for the potential and kinetic energy matrix coefficients is required. Considering an ideal and incompressible plasma, a displacement $\boldsymbol{\delta\xi}$ of the plasma will result in a force,

$$\boldsymbol{F} = \boldsymbol{J} \times \boldsymbol{\delta B} + \boldsymbol{\delta J} \times \boldsymbol{B} + \nabla(\boldsymbol{\delta\xi} \cdot \nabla P) \tag{3.23}$$

where ($\boldsymbol{\delta\xi}$, $\boldsymbol{\delta B}$, $\boldsymbol{\delta J}$) represent the mode displacement, magnetic field and current density respectively. In order to express $\boldsymbol{F}$ in an ordered way, the plasma equilibrium can be split into an axisymmetric and non-axisymmetric part, i.e. $\boldsymbol{B} = \boldsymbol{B}_0 + \boldsymbol{B}_N$. The perturbed quantities are linear with respect to equilibrium quantities and similarly,

$$\boldsymbol{\delta B} = \boldsymbol{\delta B}_n + \boldsymbol{\delta B}_{n\pm N} \tag{3.24a}$$

$$\boldsymbol{\delta J} = \boldsymbol{\delta J}_n + \boldsymbol{\delta J}_{n\pm N} \tag{3.24b}$$

$$\delta p = \delta p_n + \delta p_{n\pm N} \tag{3.24c}$$

Substituting Eqn.(3.24) into the linearised force, naturally results in an ordered axisymmetric and non-axisymmetric contribution,

$$\boldsymbol{F}_n = \boldsymbol{J}_0 \times \boldsymbol{\delta B}_n + \boldsymbol{\delta J}_n \times \boldsymbol{B}_0 + \nabla(\boldsymbol{\delta\xi}_n \cdot \nabla p_0) \tag{3.25}$$

$$\boldsymbol{F}_{n\pm N} = \boldsymbol{J}_0 \times \boldsymbol{\delta B}_{n\pm N} + \boldsymbol{J}_N \times \boldsymbol{\delta B}_n + \boldsymbol{\delta J}_n \times \boldsymbol{B}_N + \boldsymbol{\delta J}_{n\pm N} \times \boldsymbol{B}_0 + \nabla(\boldsymbol{\delta\xi}_n \cdot \nabla p_N) \tag{3.26}$$

$$\boldsymbol{F}_{n\pm 2N} = \boldsymbol{J}_N \times \boldsymbol{\delta B}_{n\pm N} + \boldsymbol{\delta J}_{n\pm N} \times \boldsymbol{B}_N \tag{3.27}$$

where $\boldsymbol{\delta B}_n = \nabla \times (\boldsymbol{\delta\xi}_n \times \boldsymbol{B}_0)$ and $\boldsymbol{\delta B}_{n\pm N} = \nabla \times (\boldsymbol{\delta\xi}_n \times \boldsymbol{B}_N)$. The zeroth order force is due to the original axisymmetric equilibrium and the first order arises due to the non-axisymmetric equilibrium that provides the coupling between the toroidal axisymmetric modes. The second order force is dropped from the calculation, as it is assumed that $\boldsymbol{F}_{n\pm 2N} \ll \boldsymbol{F}_{n\pm N}$.

The matrix coefficients δK, δW can be calculated using the above 3D equilibrium quantities $(\boldsymbol{B}_N, \boldsymbol{J}_N, \nabla p_N)$ and axisymmetric toroidal modes $\{\boldsymbol{\delta\xi}_n\}$ obtained using ELITE. Considering Eqn.(3.26) and taking the inner product with $\boldsymbol{\delta\xi}_n$, after some algebraic manipulation the matrix coefficients δK, δW are split into a volume and surface contribution, such as

$$\delta K_{0\ volume} = \frac{1}{2}\int \boldsymbol{\delta\xi}_m^* \cdot \rho_0 \boldsymbol{\delta\xi}_n \, \mathcal{J} \mathrm{d}\psi \mathrm{d}\theta^* \mathrm{d}\phi \tag{3.28}$$

$$\begin{aligned}\delta W_{0\ volume} = \frac{1}{2}\int \{ |\boldsymbol{\delta B}_{m\perp}|^2 - \frac{\boldsymbol{J_0 \cdot B_0}}{B^2}(\boldsymbol{\delta\xi}_{m\perp}^* \times \boldsymbol{B}_0) \cdot \boldsymbol{\delta B}_{m\perp} \\ - 2(\boldsymbol{\delta\xi}_{m\perp} \cdot \nabla p_0)(\boldsymbol{\delta\xi}_{m\perp}^* \cdot \boldsymbol{\kappa}_0) \} \, \mathcal{J} \mathrm{d}\psi \mathrm{d}\theta^* \mathrm{d}\phi\end{aligned} \tag{3.29}$$

$$\begin{aligned}\delta W_{N\ volume} = -\frac{1}{2}\int \{ [\boldsymbol{\delta\xi}_m^* \cdot (\boldsymbol{J}_N \times \boldsymbol{\delta B}_n + \boldsymbol{\delta J}_n \times \boldsymbol{B}_N)] \\ + [\nabla \times (\boldsymbol{\delta\xi}_m^* \times \boldsymbol{J}_0)] \cdot (\boldsymbol{\delta\xi}_n \times \boldsymbol{B}_N) \\ - \boldsymbol{\delta J}_m^* \cdot (\boldsymbol{\delta\xi}_n \times \boldsymbol{B}_N) \} \, \mathcal{J} \mathrm{d}\psi \mathrm{d}\theta^* \mathrm{d}\phi\end{aligned} \tag{3.30}$$

$$\begin{aligned}\delta W_{N\ surface} = -\frac{1}{2}\int \{ (\boldsymbol{\delta\xi}_m^* \cdot \boldsymbol{n})[(\boldsymbol{\delta\xi}_n \times \boldsymbol{B}_N) \cdot \boldsymbol{J}_0 - \boldsymbol{\delta B}_{n\pm N} \cdot \boldsymbol{B}_0] \\ + \boldsymbol{\delta B}_m^* \cdot [\boldsymbol{B}_N (\boldsymbol{\delta\xi}_n \cdot \boldsymbol{n}) - \boldsymbol{\delta\xi}_n (\boldsymbol{B}_N \cdot \boldsymbol{n})] \\ + (\boldsymbol{\delta\xi}_m^* \cdot \boldsymbol{n})(\boldsymbol{\delta\xi}_n \cdot \nabla p_N) \} \, \mathcal{J} \mathrm{d}\theta^* \mathrm{d}\phi\end{aligned} \tag{3.31}$$

Moreover, shielding currents that arise due to electron flow at rational surfaces block the corresponding resonant harmonics of the applied magnetic perturbation, and in the absence of resistivity lead to δ-function current layers [107], [108]. The calculation of those layers is subtle within a single fluid MHD model due to large Pfirsch-Schlüter currents but can be approximated from the jump of the normal derivative of the perturbed flux $\Delta_{Nl} = [(l - Nq)/q][\![\partial_\psi X_{Nl}]\!]$ according to,

$$\mu_0 \boldsymbol{J}_{||N\ screening} = -\sum_l \frac{l\Delta_{Nl}\delta(\psi - \psi_l)}{n^2 \oint B^2/|\nabla\psi|^2 \mathcal{J} \mathrm{d}\theta^* \mathrm{d}\phi} \exp\left[-i(l\theta^* - N\phi)\right] \boldsymbol{B}_0 \tag{3.32}$$

where ψ_l corresponds to the poloidal flux at a rational surface. The corresponding coupling coefficients that arise from this contribution are given by,

$$\delta W_{N\ screening} = -\int \boldsymbol{\delta\xi}^*_m \cdot (\boldsymbol{J}_{||N\ screening} \times \boldsymbol{\delta B}_n)\, \mathcal{J} \mathrm{d}\psi \mathrm{d}\theta^* \mathrm{d}\phi \tag{3.33}$$

3.3 Linear Ideal MHD Plasma Response

The application of external non-axisymmetric fields results in a non-axisymmetric plasma equilibrium configuration. In order to obtain such a configuration various approaches can be followed. Equilibrium solutions can be obtained by solving the ideal MHD set of equations numerically using nonlinear MHD codes, e.g. VMEC [109], or by approximating the solution by solving the linearised MHD set of equations using axisymmetric eigenvalue stability codes in marginal stability, e.g. IPEC [110] or MARS-F [85]. Due to the fact that MP fields are much smaller than axisymmetric equilibrium fields, the solution of the linearised set of equations provides realistic solutions in comparison to nonlinear solutions [111], [112], [113]. In addition, the use of an eigenvalue code results in a much faster computation in comparison to nonlinear MHD codes, allowing the integration of the plasma response to a framework that uses axisymmetric stability codes to study the non-axisymmetric equilibrium and stability. For example, as part of a design loop for optimising the MP coil configuration.

In this work, the low n version of ELITE is used to calculate the plasma response, where details in the differences between the high n and the low n version of ELITE is given in Chapter2. As described in Chapter2, ELITE evolves a second order differential equation for the functional of the normal displacement that minimises energy, according to

$$[A_{mm'} d_{\psi\psi} + B_{mm'} d_\psi + C_{mm'}] X_{m'} = 0 \tag{3.34}$$

where $\{X_m\}$ define the Fourier coefficients of the normal displacement functional,

$$X(\psi, \theta^*, \phi) = \sum_m X_m(\psi) e^{-i(m\theta^* - n\phi)} \tag{3.35}$$

The evolution of Eqn.(3.34) requires the solution of the boundary condition that evaluates the normal displacement and its gradient at the plasma-vacuum interface,

$$D_{mm'} d_\psi X_{m'} = E_{mm'} X_{m'} \tag{3.36}$$

In order to represent some external non-axisymmetric field, the normal perturbation $\{X_m\}$ is fixed at the plasma-vacuum interface and the boundary condition provides a solution for the gradient $d_\psi X_m$, such that Eqn.(3.34) can be evolved in space. Therefore, the non-axisymmetric normal magnetic field, which is continuous at the interface, can provide a way to compute the normal plasma displacement using the linearised induction equation $\boldsymbol{B}_N = \nabla \times (\boldsymbol{\xi}_N \times \boldsymbol{B}_0)$, such that

$$\begin{aligned} \boldsymbol{B}_N \cdot \boldsymbol{n} &= \frac{\boldsymbol{B} \cdot \nabla}{|\nabla \psi|} \sum_l X_{l,N} \exp\left[-i(l\theta^* - iN\phi)\right] \\ \Rightarrow X_{l,N} &= \mathcal{F}\{i \frac{|\nabla\psi| \mathcal{J}}{\nu} \boldsymbol{B}_N \cdot \boldsymbol{n}\}_l / (\frac{l - nq}{q}) \end{aligned} \tag{3.37}$$

This approach assumes prior knowledge of the non-axisymmetric normal magnetic field at the vacuum region and corresponds to a fixed boundary plasma response. In the case where vacuum currents, i.e. coils, give rise to the perturbation a free boundary response needs to be taken into account. Nevertheless, for the stability examination of the tokamak plasma under the application of some external magnetic perturbation, this approach is sufficient to generate a consistent plasma response to be used.

In future work, it is visualised that the vacuum code provides the necessary information for the calculation of a free boundary response. In principle, the free boundary response can be computed considering the relation of the vacuum magnetic field to the total magnetic field, i.e. including the plasma response. It is proven that a linear transformation exists to map the normal vacuum field to the normal total field [114], where the map is the product of the vacuum magnetic inductance $\boldsymbol{\Lambda}$ [115] to the inverse of the plasma inductance

$\boldsymbol{L}^{-1}$, such that $B_\psi^{tot} = \boldsymbol{\Lambda}\boldsymbol{L}^{-1}B_\psi^{vac}$. The vacuum inductance is an integral function that depends on the geometry and current density of the coils and the plasma inductance relates the added plasma potential energy to the induced poloidal magnetic flux. The latter is a quantity that can be obtained from an axisymmetric stability code at marginal stability. Finally, it should be noted that within the context of linear plasma response, scaling the perturbed flux at the plasma surface is equivalent to scaling the amplitude of the current on the coil configuration. Therefore, in this thesis where a fixed plasma response is considered, it can still be correlated to an increasing current in the MP coils, as long as the linear response remains a reasonable approximation for the amplitude of the applied field.

The low n ELITE code provides the radial dependence of the normal displacement. The binormal displacement is related to the normal displacement due to energy minimisation as discussed in Chapter2, and ELITE provides the corresponding relation through matrices W^1 and W^2,

$$U = \frac{i}{n}[\partial_\psi X + \mu_0 \frac{\partial_\psi p}{B^2} + W] \tag{3.38}$$

$$W_m = [W^1_{mm'} d_\psi + W^2_{mm'}]X_{m'} \tag{3.39}$$

From the perpendicular displacement $\boldsymbol{\xi}_{\perp N}$, the full non-axisymmetric equilibrium quantities $\boldsymbol{B}_N, \boldsymbol{J}_N, \nabla p_N$ can be obtained through the linearised set of ideal MHD equations. To begin with, inserting $\boldsymbol{\xi}_{\perp N}$ into the magnetic induction equation and after some algebraic manipulation, the non-axisymmetric magnetic field becomes,

$$\boldsymbol{B}_N = B_\psi \frac{\nabla\psi}{|\nabla\psi|^2} + B_s \frac{\boldsymbol{B}\times\nabla\psi}{B^2} + B_b \frac{\boldsymbol{B}}{B^2} \tag{3.40}$$

$$B_\psi = \frac{\boldsymbol{B}\cdot\nabla}{|\nabla\psi|^2} X_N \tag{3.41}$$

$$B_s = \frac{\boldsymbol{B}\cdot\nabla}{|\nabla\psi|^2} U_N - S\frac{B^2}{|\nabla\psi|^2} X_N \tag{3.42}$$

$$B_b = -[(\nabla\cdot\boldsymbol{\xi}_{\perp N} + 2\boldsymbol{\xi}_{\perp N}\cdot\boldsymbol{\kappa}) + p_N] \tag{3.43}$$

where $p_N = -\boldsymbol{\xi}_{\perp N} \cdot \nabla p / B^2$ is the non-axisymmetric pressure. Once the magnetic field is known, the calculation of the non-axisymmetric current density becomes straight forward, as it represents the curl of the magnetic field. In the orthogonal coordinate system under consideration the curl of a vector field $A_i \nabla x^i$ is obtained through $(\nabla \times \boldsymbol{A})_i = \epsilon_{ijk}(g_{ii}/\mathcal{J})[\partial_j A_k - \partial_k A_j]$ and the metric coefficients can be found in Chapter2. The non-axisymmetric pressure gradient can be obtained considering the linearised force balance $\nabla p_N = \boldsymbol{J}_N \times \boldsymbol{B} + \boldsymbol{J} \times \boldsymbol{B}_N$.

3.4 3D Stability Framework Using ELITE

ELMs are an intermediate to high n ideal MHD phenomenon and no global ideal 3D MHD stability code has been used to resolve the effect of MPs on the stability of these modes, since the resolution required in the normal direction and the number of poloidal and toroidal harmonics required is significant. The perturbative and variational approaches proposed, allow the examination of individual triplet modes that simplify the numerical complexity of the problem. The aim of this work is to be able to routinely produce stability diagrams for shots with applied MPs as is done currently with ELITE for axisymmetric discharges. This is the first stage of a project to develop a tool which can optimise plasma response and ELM stability together. This will be required for the design of a plasma scenario for future reactors if ELM control coils will be needed. It may also help us understand the details of ELM mitigation and suppression.

As a result, the non-axisymmetric stability of a tokamak plasma that is subject to external small non-axisymmetric fields requires the knowledge of the plasma response, i.e. the non-axisymmetric equilibrium component, and of the axisymmetric normal modes as result from the stability of the axisymmetric system. All required information can be obtained from axisymmetric stability codes, which are routinely used to compute both the axisymmetric stability as well as the linear plasma response. As such, a numerical framework based on axisymmetric stability codes can be created to compute the stability of the plasma under the application of external non-axisymmetric fields. In this work, the low n version of ELITE is used as it can provide both the

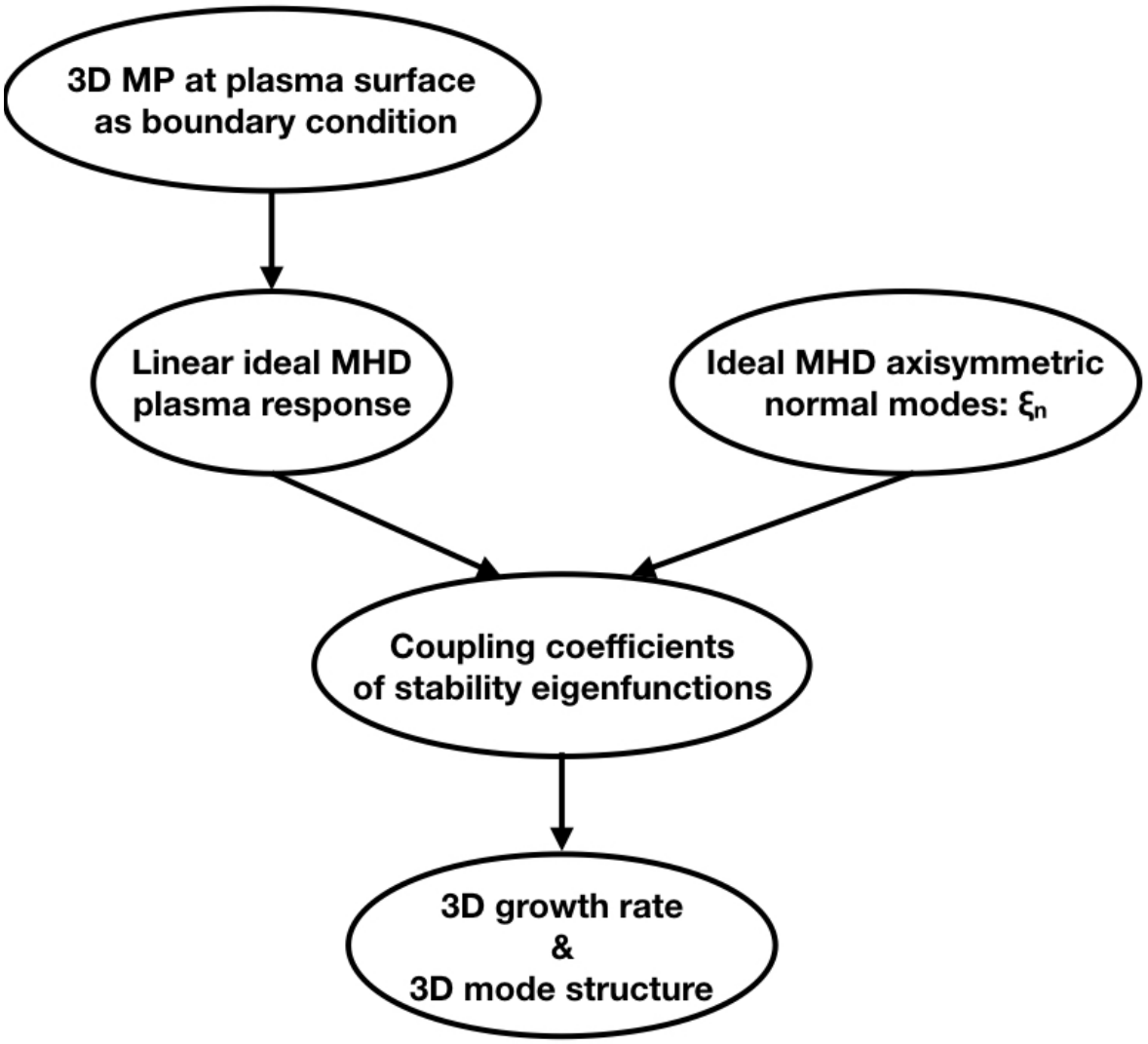

FIGURE 3.1: Schematic of the workflow of the 3D stability numerical framework based on an axisymmetric stability code such as ELITE.

low n linear plasma response and the intermediate to high n axisymmetric peeling-ballooning eigenfunctions. A schematic of the workflow can be seen in Fig.3.1. The numerical framework is implemented in a Fortran90 code and further information can be found in AppendixA.

Chapter 4

Application to External Magnetic Perturbations

4.1 Implementation of Boundary Condition

The calculation of the linear plasma response with low n ELITE requires the knowledge of the normal magnetic field at the plasma-vacuum interface. This is calculated by a Fortran90 code developed for this purpose which computes the vacuum magnetic field due to a set of current carrying coils; more details can be found in AppendixB. Once the normal magnetic field is known at the plasma boundary, Eqn.3.37 is used to provide the boundary condition inserted in ELITE.

Benchmark Study

In order to test the accuracy of the calculation of the magnetic field two analytic cases were investigated. The first case referred to an infinitely long current carrying wire. The wire was placed perpendicular to the xy-plane and centred at $z = 0$, such that current flows along the z-axis. Therefore the resulting magnetic field at a radial distance r is given by $B = \mu_0 I/2\pi r$. The second case referred to the magnetic field produced by a closed current carrying loop placed in the xy-plane and centred at $z = 0$. The magnetic field produced along the

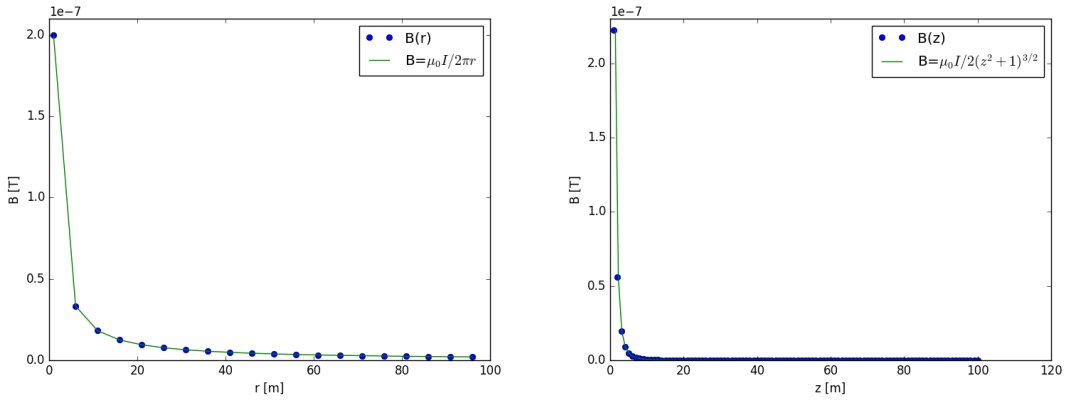

(A) (B)

FIGURE 4.1: Comparison of computational and analytical value of the magnetic field as produced by (A) an infinite wire and (B) a closed loop.

z-axis is $B = \mu_0 R^2 I/2(z^2 + R^2)^{3/2}$. Fig.[4.1a] and Fig.[4.1b] show the calculated field as a function of the distance from the wire and loop respectively.

Further benchmarking was performed with results from ERGOS, a magnetic vacuum code, for the vacuum field as produced by the in-vessel MP coil system in MAST. In MAST each coil is composed of 4 thick wire turns each carrying up to 1.4 kA. The coil locations are given by $(r_0, z_0) = (1.44, 0.595)$ and $(r_1, z_1) = (1.322, 0.795)$, where (r_0, z_0) is one corner and (r_1, z_1) is the opposite corner of the coil, and an N=3 odd current configuration is considered. The radial component of the field is calculated in terms of the cylindrical (r, z) cross-section. The location in the chamber under consideration was $(r, z) = (1.4, -0.5)$ for the odd current configuration. Very good agreement was obtained between the two codes. Fig.[4.2] show the comparison between ERGOS [116] and Fig.[4.3] shows the field on the whole surface.

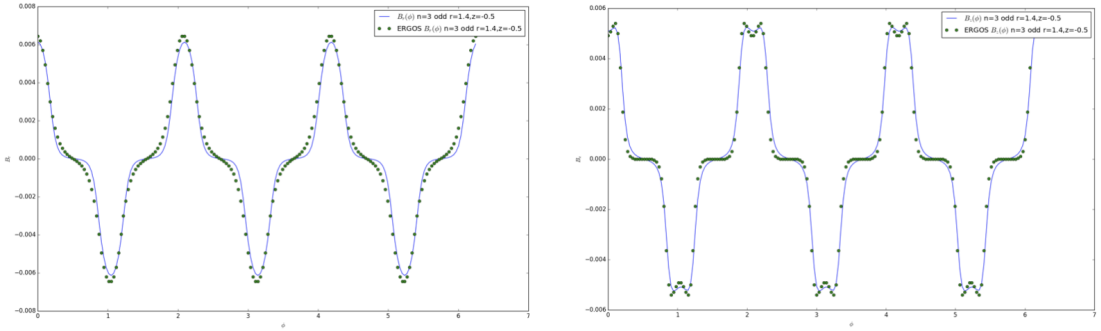

FIGURE 4.2: Comparison of the magnetic field B_r, B_z with ERGOS for an odd n=3 configuration at $(r, z) = (1.4, -0.5)$.

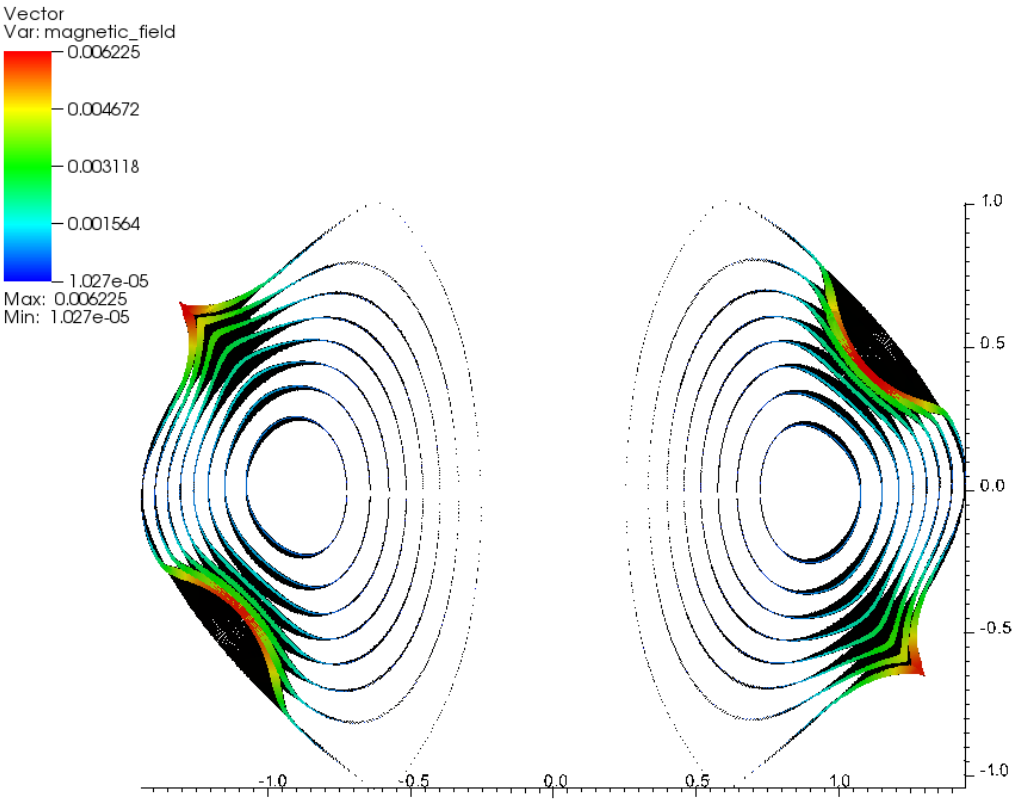

FIGURE 4.3: MP field $\boldsymbol{B}$ as produced by a odd N=3 current configuration in MAST.

4.2 Fixed Boundary Plasma Response with ELITE

4.2.1 Circular Large Aspect Ratio Plasma Equilibrium

The calculation of the non-axisymmetric part of the equilibrium begins with an initial axisymmetric equilibrium that is stable to low n toroidal modes but unstable to intermediate to high n ballooning modes, to which MP fields are applied. We examine such an equilibrium for a large aspect ratio $\epsilon = 0.33$ circular cross-section plasma of core pressure $p_0 = 22.8$ [kPa], core magnetic field $B_0 = 1.8$ [T], core parallel current density $J_{||0} = 0.7$ [MAm^{-2}] and edge safety factor $q_a = 2.71$. The axisymmetric equilibrium plasma profiles and PB stability analysis are illustrated in Fig.4.4.

Two cases are examined, one for a resonant magnetic field and one for a non-resonant magnetic field at the plasma-vacuum interface for a toroidal mode number $N = 3$ MP field. The resonance condition is met by maximising

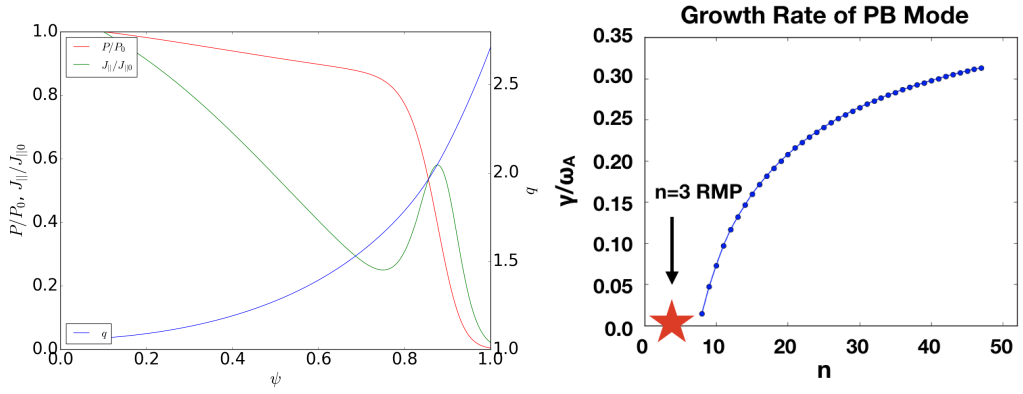

(A) (B)

FIGURE 4.4: Normalised radial equilibrium plasma profiles for A) the pressure, outer mid-plane current density and q-profile as a function of the normalised poloidal flux as well as B) the normalised PB growth rate for the $cbm18\_dens6$ equilibrium as a function of the toroidal mode number.

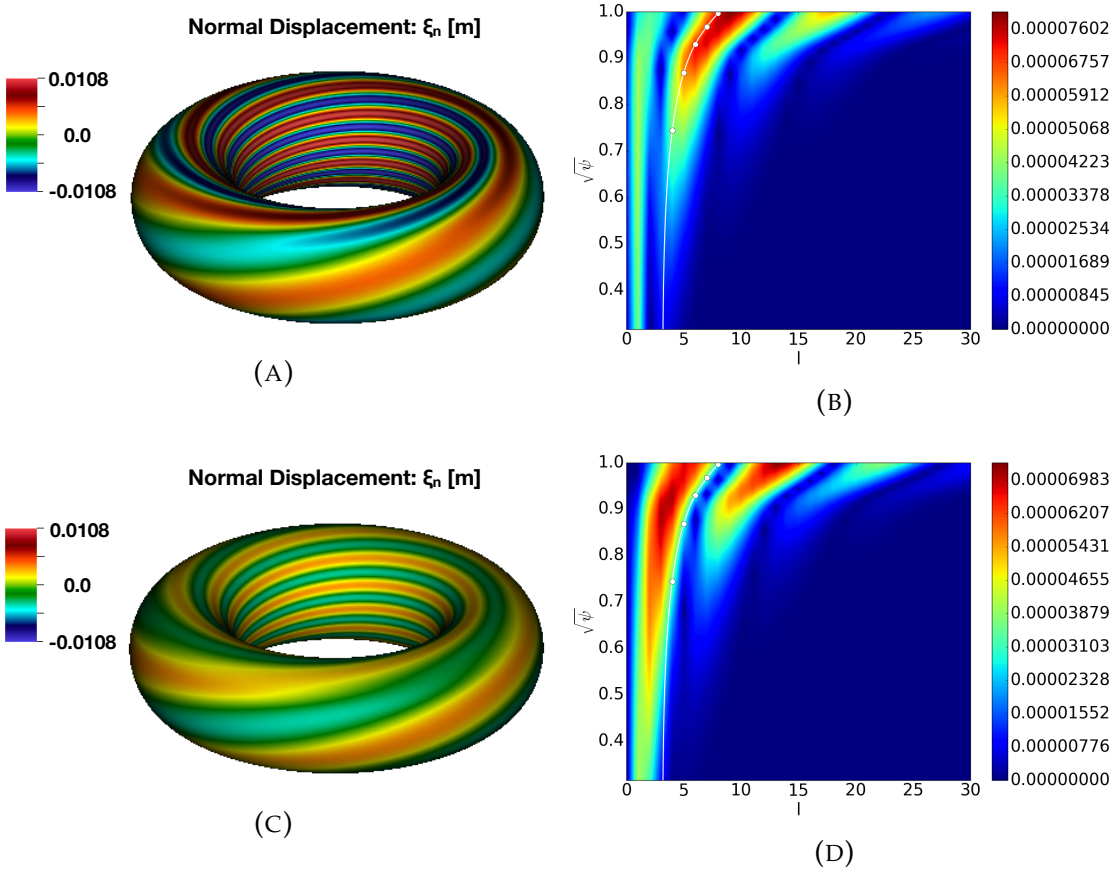

(A) (B)

(C) (D)

FIGURE 4.5: Normal displacement $\boldsymbol{\xi}_N \cdot \boldsymbol{n}$ [m] and poloidal mode structure in a straight field-line angle coordinate system for the normal magnetic field $\boldsymbol{B}_N \cdot \boldsymbol{n}$ [T] for the (A),(B) resonant and (C),(D) non-resonant N=3 MP configuration at the plasma surface. The solid white line represents the resonant location $q_a N = 8.13$ of the plasma surface.

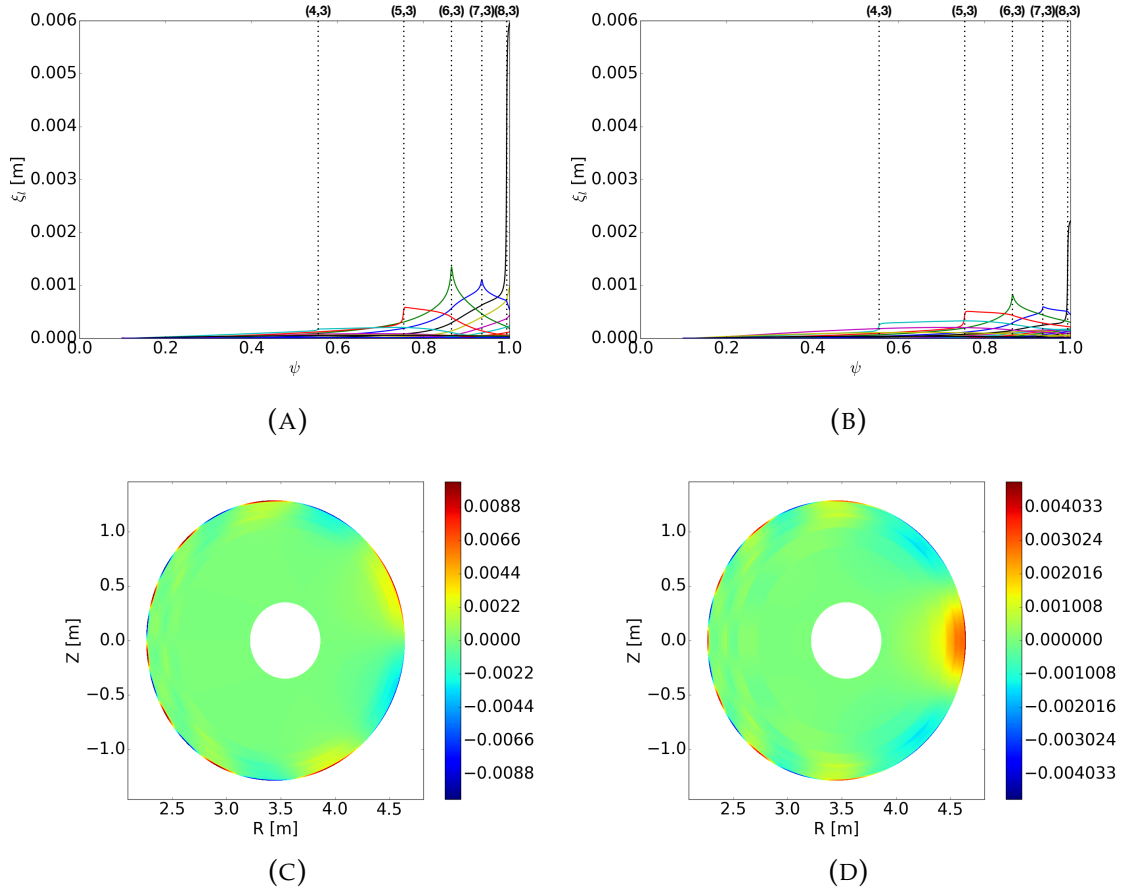

FIGURE 4.6: The radial dependence of the poloidal Fourier harmonics ξ_l for $l = [0, 70]$ of the normal displacement $\boldsymbol{\xi}_N \cdot \boldsymbol{n}$ [m] as a function of ψ for (A) a resonant and (B) a non-resonant $N = 3$ MP field. The harmonics that peak around resonant surfaces are the corresponding resonant harmonics. In addition, the reconstruction of the poloidal cross section of the mode (C) and (D) for the resonant and non-resonant case respectively.

the vacuum poloidal harmonics l at radial location where $q \sim l/N$. Fig.4.5 illustrates the normal displacement $\boldsymbol{\xi}_N \cdot \boldsymbol{n}$ that represents the boundary condition, and the poloidal mode structure of the corresponding normal magnetic field $\boldsymbol{B}_N \cdot \boldsymbol{n}$, where $\boldsymbol{n} = \nabla\psi/|\nabla\psi|$ is the unit vector normal to the magnetic flux surfaces of the axisymmetric reference equilibrium.

In the resonant case, the plasma response is characterised by a strong peeling-like normal displacement, as the amplitude of the last resonant poloidal harmonic is much larger than the rest of the poloidal harmonics. In the non-resonant case, a kink-ballooning response is observed, as the amplitude of the last resonant harmonic is comparable to the rest of the poloidal harmonics. The normal displacement is strongly peaked around rational surfaces in both

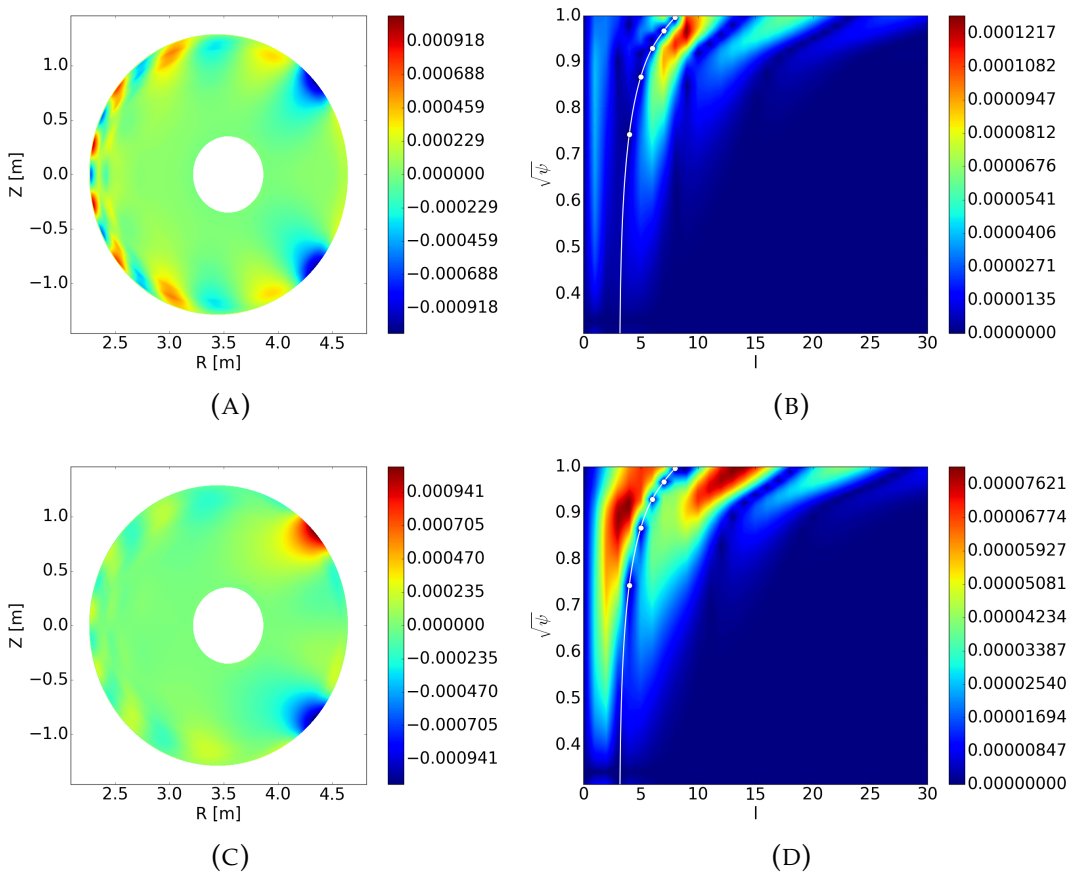

FIGURE 4.7: The (A),(C) normal component of magnetic field $\boldsymbol{B}_N \cdot \boldsymbol{n}_0$ [T] and (B),(D) its poloidal mode structure B_{Nl} [T] in a straight field-line angle coordinate system as reconstructed from ELITE output data for (A),(B) a resonant and (C),(D) a non-resonant N=3 MP configuration. The straight white line indicates the position of the q-profile.

cases, due to resonance with the corresponding poloidal harmonics and finite pressure gradient, leading to large local response and potential break down of the linear response. Away from the rational surfaces $(\boldsymbol{\xi}_N \cdot \boldsymbol{n})/R \sim (\boldsymbol{B}_N \cdot \boldsymbol{n})/B_0$, such that a linear response is valid in the majority of the plasma volume and in many cases is observed to match with a non-linear plasma response model [117]. The mode structure and the poloidal cross-section reconstruction of the normal displacement are depicted in Fig.4.6.

In this ideal MHD model, individual poloidal harmonics of the normal magnetic field are screened at their corresponding rational surfaces so that island formation is prohibited, since field line bending is minimised, i.e. $(\boldsymbol{B}_0 \cdot \nabla) \propto (l - Nq) = 0$. Nevertheless, this screening is imperfect due to poloidal mode coupling in toroidal geometry, that allows field penetration. In the non-resonant case, the screening effect is reduced since the poloidal harmonics

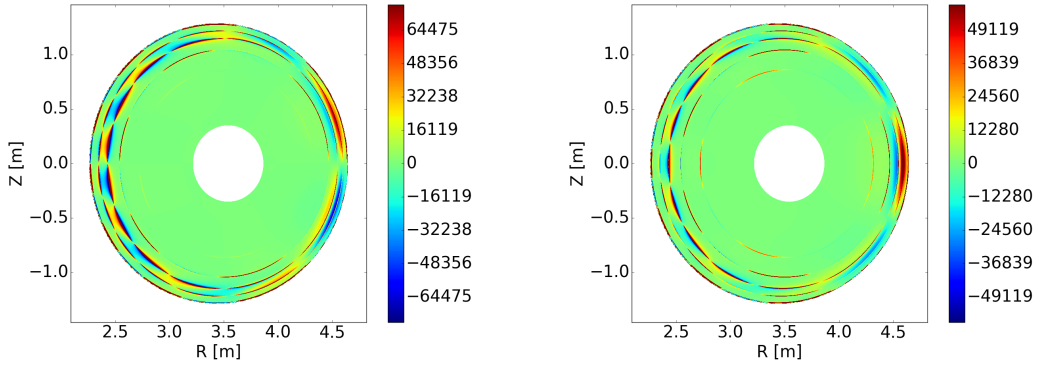

(A) (B)

FIGURE 4.8: The parallel current density $J_{||N}$ [Am^{-2}] as reconstructed from ELITE output data for the (A) resonant and (B) non-resonant $N = 3$ MP configuration.

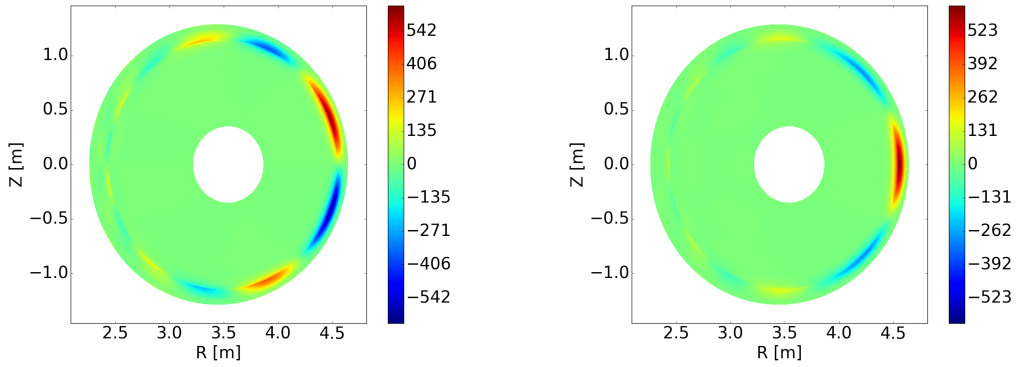

(A) (B)

FIGURE 4.9: The plasma pressure p_N [Pa] as reconstructed from ELITE output data for the (A) resonant and (B) non-resonant $N = 3$ MP configuration.

of the vacuum MP field are already minimised at their rational surfaces, and the vacuum field is not significantly altered. However, in the resonant case, the poloidal harmonics of the vacuum MP field are maximised at their rational surfaces and strong screening is observed, leading to significant modification of the MP vacuum field and amplification of external poloidal harmonics in the plasma. The normal field and its poloidal mode structure are illustrated in Fig.4.7.

The calculation of the current density becomes straightforward once the magnetic field and metrics of the coordinate system are known. Fig.4.8 illustrates the parallel current density $J_{||N}$ created around rational surfaces, which has two contributions. One contribution corresponds to the existence

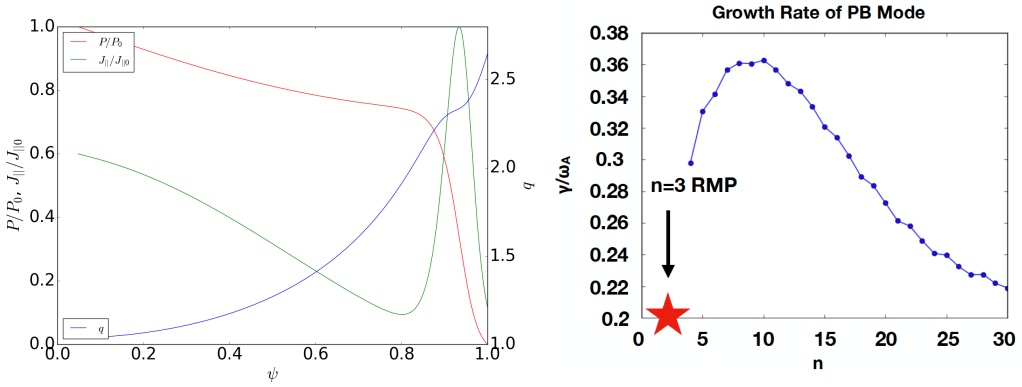

(A) (B)

FIGURE 4.10: Normalised radial equilibrium plasma profiles for A) the pressure, outer mid-plane current density and q-profile as a function of the normalised poloidal flux as well as B) the normalised PB growth rate for the $dbm9$ D-shaped equilibrium as a function of the toroidal mode number.

of Pfirsch-Schlüter current density due to quasi-neutrality and non-vanishing pressure gradient. The second contribution arises due to screening currents at rational surfaces. The ideal plasma response results in large Pfirsch-Schlüter current density for both MP configurations, which is the dominant contribution to the current density. The final perturbed quantity is the non-axisymmetric pressure calculated using the linearised perturbation $p_N = -\boldsymbol{\xi}_{\perp N} \cdot \nabla p_0$. For the toroidal mode coupling coefficients the pressure gradient ∇p_N is needed and obtained through the linearised force balance $\boldsymbol{J}_N \times \boldsymbol{B}_0 + \boldsymbol{J}_0 \times \boldsymbol{B}_N = \nabla p_N$. The non-axisymmetric pressure profile is shown in Fig.4.9.

4.2.2 D-shaped Plasma Equilibrium

A D-shaped plasma equilibrium configuration is also investigated, which is unstable to low n kink modes and unstable to intermediate to high n ballooning modes. Fig.4.10 shows the axisymmetric plasma equilibrium profiles, for a core pressure $p_0 = 81.88$ [kPa], core magnetic field $B_0 = 3.05$ [T], core parallel current density $J_{||0} = 1.69$ [MAm^{-2}] and edge safety factor $q_a = 2.65$, as well as the axisymmetric ideal MHD stability. It can be observed that a characteristic peak exist at intermediate $n \sim 10$ due to kink unstable modes, while the characteristic ballooning spectrum is retrieved for high $n > 30$ (not shown).

The plasma surface normal displacement $\boldsymbol{\xi}_N \cdot \boldsymbol{n}$ is nearly resonant with the plasma, leading to an external kink-ballooning response. Fig.4.11 illustrates the

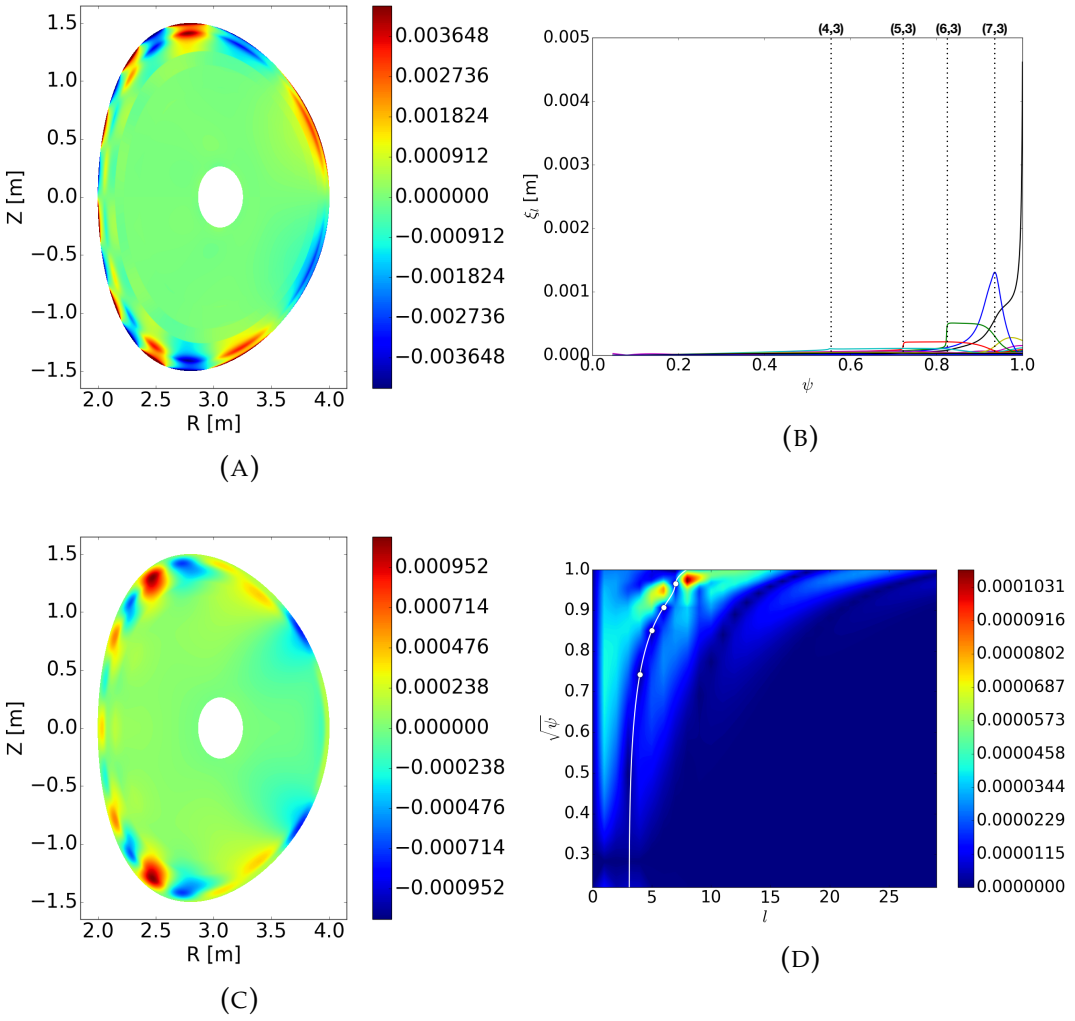

FIGURE 4.11: (A),(C) The normal displacement $\boldsymbol{\xi}_N \cdot \boldsymbol{n}$ [m] and magnetic field $\boldsymbol{B_N} \cdot \boldsymbol{n}$ [T] and (B),(D) the corresponding mode structure in a straight field line poloidal angle. The straight white line indicates the position of the q-profile.

normal displacement $\boldsymbol{\xi}_N \cdot \boldsymbol{n}$ and the normal magnetic field $\boldsymbol{B}_N \cdot \boldsymbol{n}$ as well as the corresponding poloidal mode structures, and it can be observed that a strong external kink response is formed from the first external poloidal harmonic of the displacement, leading to excitation of external modes for the magnetic field.

4.3 Benchmark with BOUT++ and MARS-F

The nonlinear MHD BOUT++ fluid code and the linear MHD MARS-F eigenvalue code have been compared with the computed non-axisymmetric equilibrium from ELITE to verify the calculation.

4.3.1 BOUT++ Benchmark

BOUT++ is used to model the linear plasma response imposing a fixed parallel magnetic potential $A_{||N}$ at the outer boundary of the computational domain. At first the $A_{||N}$ is computed using the original coordinate system $[\nabla\psi, \nabla\theta, \nabla\phi]$ and then transformed into a field aligned coordinate system $[\nabla\psi, \boldsymbol{B}_0, \nabla(\phi - q\theta^*)]$ that BOUT++ uses, employing the transformation $A_{||N} \equiv A_{||N} \exp[-i(qN\theta^*)]$. The physics model under consideration is based on a reduced ideal MHD 3-field model appropriate for flute-like $k_\perp \gg k_{||}$ and incompressible $\nabla \cdot \boldsymbol{\xi} = 0$ perturbations,

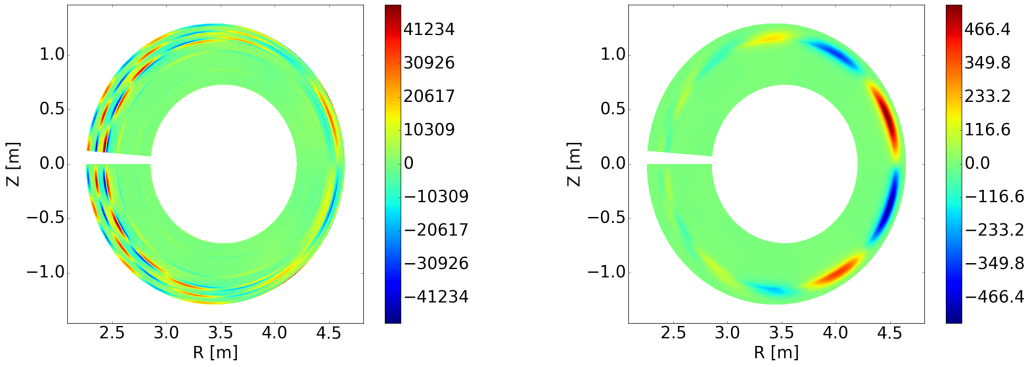

(A) (B)

FIGURE 4.12: The (A) parallel current density $J_{||N}$ [Am^{-2}] and (B) plasma pressure p_N [Pa] as calculated from BOUT++ for the resonant $N = 3$ MP field.

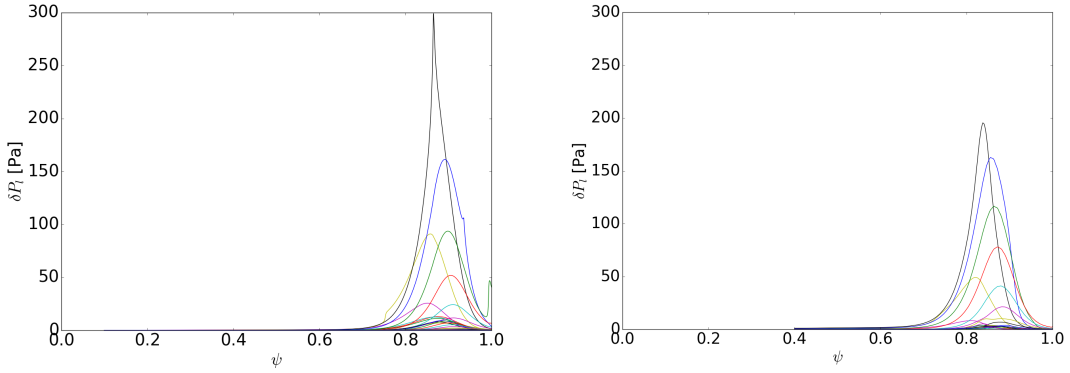

(A) (B)

FIGURE 4.13: Comparison of the plasma pressure poloidal mode structure in the straight field line angle coordinate system between (A) ELITE and (B) BOUT++ results.

$$\frac{\partial w}{\partial t} = B^2 \mathbf{b} \cdot \nabla(\frac{J_{||}}{B}) + 2\mathbf{b_0} \times \kappa_\mathbf{0} \cdot \nabla p \tag{4.1}$$

$$\frac{\partial p}{\partial t} = -\frac{1}{B_0}\mathbf{b_0} \times \nabla\phi \cdot \nabla p \tag{4.2}$$

$$\frac{\partial \psi}{\partial t} = -\frac{1}{B_0}\nabla_{||}\phi \tag{4.3}$$

with a closure that relates the electric potential to the vorticity and the parallel current density to the poloidal flux,

$$w = \frac{\rho_0}{B_0}\nabla_{\perp}^2\phi \tag{4.4}$$

$$J_{||} = J_{||0} - \frac{1}{\mu_0}B_0\nabla_{\perp}^2(\psi + \psi_{MP}) \tag{4.5}$$

As can be observed from Fig.4.12 and Fig.4.13, the non-axisymmetric equilibrium pressure and parallel current density match well with ELITE. Some discrepancy occurs close to rational surfaces, which is attributed to the non-uniform grid spacing along the normal direction that allows very fine resolution close to rational surfaces with ELITE, and as a result sharper features can be resolved. In addition, for numerical stability a small value of numerical dissipation is required in the BOUT++ simulations, and this also tends to round off the sharp features.

4.3.2 MARS-F Benchmark

A further benchmark is performed for an experimental equilibrium configuration with the MARS-F code. MARS-F is an eigenvalue code that solves the linearised resistive MHD model and computes the free boundary linear plasma response considering current coils in the vacuum region. The set of MHD equations for a given equilibrium toroidal rotation $\boldsymbol{v} = \omega\nabla\phi$ is given by,

$$i(\omega_{MP} + N\omega)\boldsymbol{\delta\xi} = \boldsymbol{\delta v} + (\boldsymbol{\delta\xi}\cdot\nabla\omega)\nabla\phi \tag{4.6}$$

$$\begin{aligned} i(\omega_{MP} + N\omega)\boldsymbol{\delta v} = &-\nabla\delta p + \boldsymbol{\delta J}\times\boldsymbol{B} + +\boldsymbol{J}\times\boldsymbol{\delta B} \\ &-\rho[2\omega\hat{\boldsymbol{z}}\times\boldsymbol{\delta v} + (\boldsymbol{\delta v}\cdot\nabla\omega)\nabla\phi] \\ &-\rho\kappa_{||}|k_{||}v_{th,i}|[\boldsymbol{\delta v} + (\boldsymbol{\delta\xi}\cdot\nabla\boldsymbol{v})] \end{aligned} \tag{4.7}$$

$$i(\omega_{MP} + N\omega)\boldsymbol{\delta B} = \nabla\times(\boldsymbol{\delta v}\times\boldsymbol{B}) + (\boldsymbol{\delta B}\cdot\nabla\omega)\nabla\phi - \nabla\times(\eta\boldsymbol{\delta J}) \tag{4.8}$$

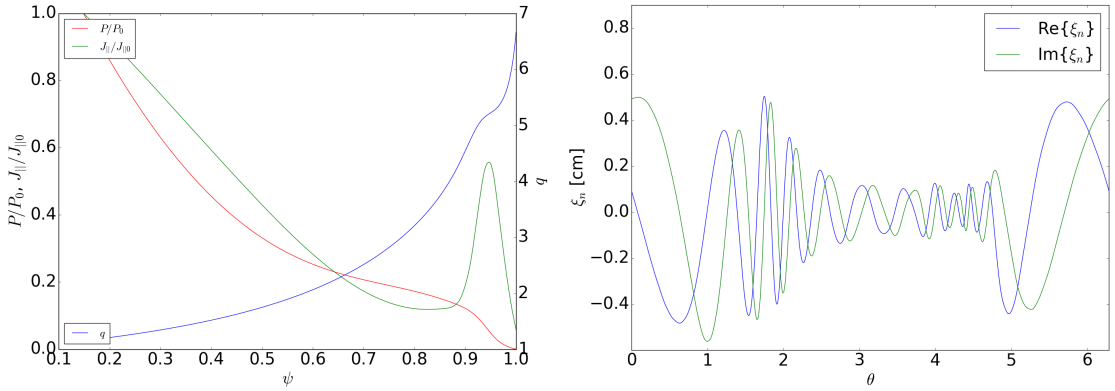

(A) (B)

FIGURE 4.14: A) Equilibrium profiles of the normalised plasma pressure P/P_0, the normalised parallel current density $J_{||}/J_{||0}$ at the outboard mid-plane and the safety factor q. B) The plasma surface normal displacement $\boldsymbol{\xi}_N \cdot \boldsymbol{n}$ due to a N=2 MP field. Those figures were provided by D. Ryan

$$i(\omega_{MP} + N\omega)\delta p = -\boldsymbol{\delta v} \cdot \nabla p - \gamma p \nabla \cdot \boldsymbol{\delta v} \tag{4.9}$$

where N and ω_{MP} is the toroidal mode number and rotational frequency of the applied MP field respectively, $v_{th,i}$ is the ion thermal velocity, η is the plasma resistivity and $\kappa_{||}$ is a damping amplitude due to fluid compression. In order to match the resistive MHD model to ELITE, the resistivity η, the damping $\kappa_{||}$ and the equilibrium rotational frequency ω are considered negligible leading to the linearised ideal MHD model.

The plasma equilibrium under consideration is based on an AUG equilibrium, which was provided by S. Saarelma, and the plasma surface perturbation is known from the MARS-F solution, which was provided by D. Ryan. ELITE is used as a fixed boundary response solver to compute the plasma response within the plasma region, leading to a direct comparison of the two codes. The equilibrium plasma profiles and surface normal displacement due to applied MPs of the shot #30839 is illustrated in Fig.4.14, where $p_0 = 66.4$ [kPa], $J_{||0} = 1.8$ [MAm^{-2}] and $q_a = 6.66$.

The benchmark case under consideration refers to an applied $N = 2$ MP field of $\Delta\phi = 0$ for the AUG MP coils and is a case that has been already benchmarked with VMEC, as well as compared with experimental measurements. Fig.4.15 illustrates the normal plasma displacement $\boldsymbol{\xi}_N \cdot \boldsymbol{n}$ and the corresponding straight field line poloidal mode structure derived from MARS-F.

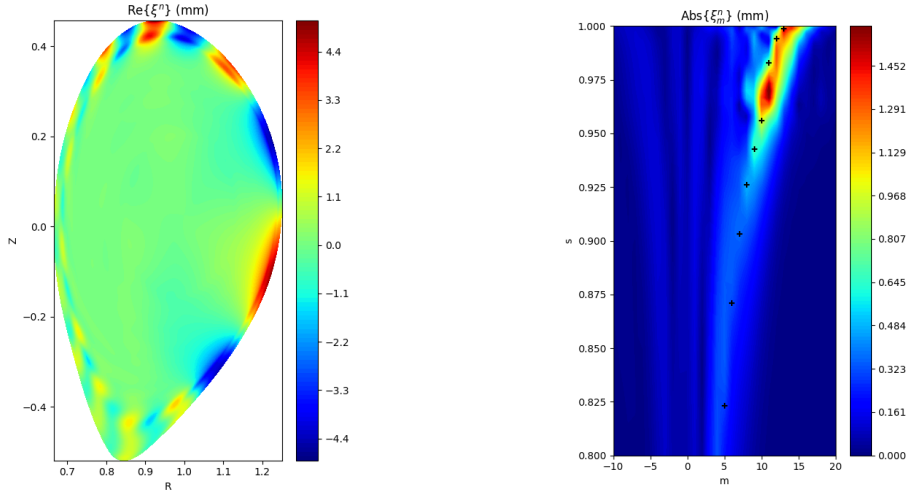

(A) (B)

FIGURE 4.15: A) The normal plasma displacement $\boldsymbol{\xi}_N \cdot \boldsymbol{n}$ [mm] and B) the mode structure $\xi_{N,l}$ in the straight field line poloidal angle for the $N = 2$, $\Delta\phi = 0$ MP coil configuration in AUG shot #30839 as produced from MARS-F.

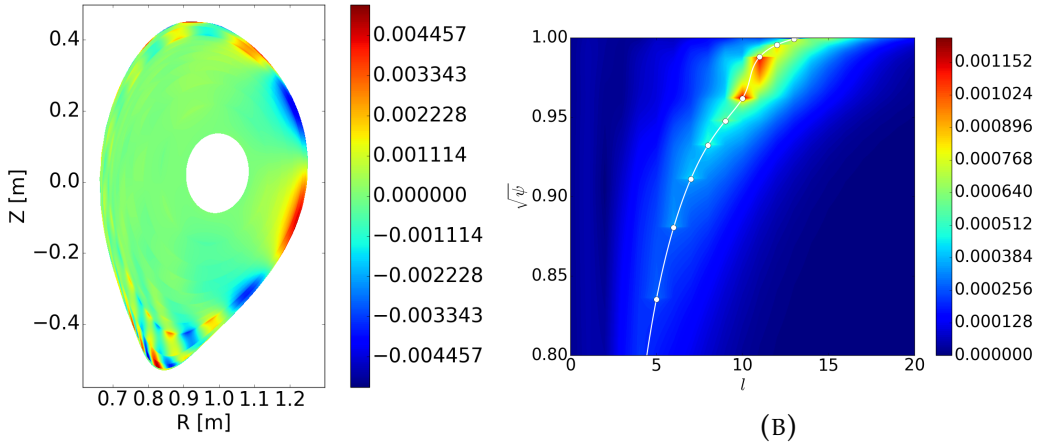

(A) (B)

FIGURE 4.16: A) The normal plasma displacement $\boldsymbol{\xi}_N \cdot \boldsymbol{n}$ [m] and B) the mode structure $\xi_{N,l}$ in the straight field line poloidal angle for the $N = 2$, $\Delta\phi = 0$ MP coil configuration in AUG shot #30839 as produced from ELITE.

As can be observed from Fig.4.16 the plasma response as produced from ELITE is in good agreement with MARS-F (the reader should bear in mind that the displacement from MARS is in [mm] while from ELITE is in [m]). A difference occurs close to the X-point region, which is attributed to an oscillatory behaviour of the poloidal magnetic field in the equilibrium input file in the run with ELITE. In addition, from the mode structure it becomes apparent that the displacement of each individual harmonic peaks very close

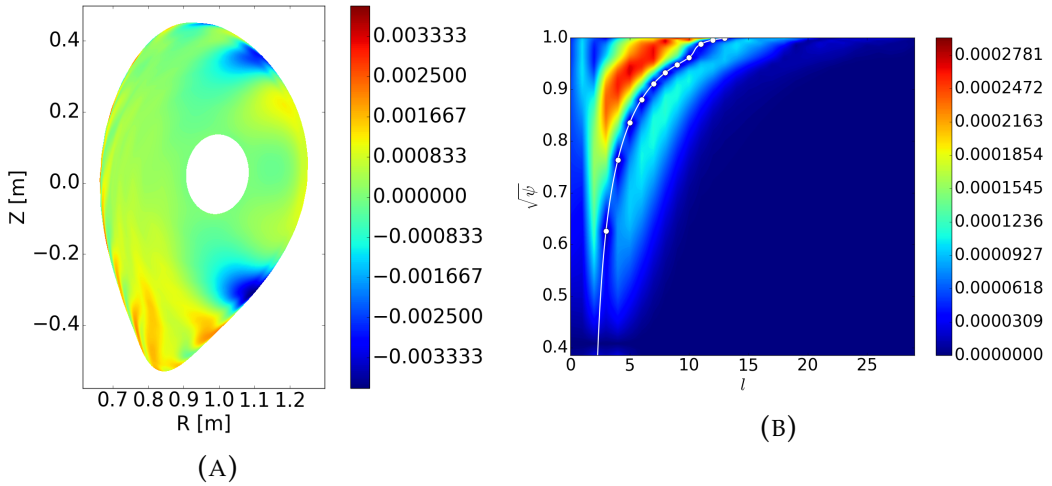

(A) (B)

FIGURE 4.17: (A) The normal magnetic field $\boldsymbol{B}_N \cdot \boldsymbol{n}$ [T] and (B) the mode structure $B_{N,l}$ in the straight filed line poloidal angle for the $N = 2$, $\Delta\phi = 0$ MP coil configuration in AUG shot #30839 as produced from ELITE.

to the rational surfaces, while in the MARS-F case it happens in between the rational surfaces. Fig.4.17 illustrates the resulting normal component of the magnetic field $\boldsymbol{B}_N \cdot \boldsymbol{n}$ and its poloidal mode structure, where clear screening of the magnetic field is observed around the q-profile.

4.4 Perturbative Stability Analysis

In order to test the perturbative method the $cbm18\_dens6$ equilibrium is used. The linear plasma response for a resonant and non-resonant MP is computed and presented in the previous section. In addition, ELITE is used to calculate the axisymmetric stability to obtain the axisymmetric toroidal normal modes $\boldsymbol{\xi}_{0n}$ and their growth rates ω_{0n}. This information is used to compute the coupling coefficients Eqn.3.14. Two plasma responses are taken into account, one for a resonant perturbation and one for a non-resonant perturbation.

As stated in Chapter3, the perturbative analysis results is a truncation of 3D toroidal mode families due to weak toroidal coupling and results in triplet modes $\{n - N, n, n + N\}$. Considering the resonant case, Fig.4.18a illustrates the growth rate of the triplet modes $\{n - N, n, n + N\}$ as a function of toroidal mode number for the primary mode n and applied field strength B_N/B_0. As can be observed, a small increase in the growth rate occurs indicating further

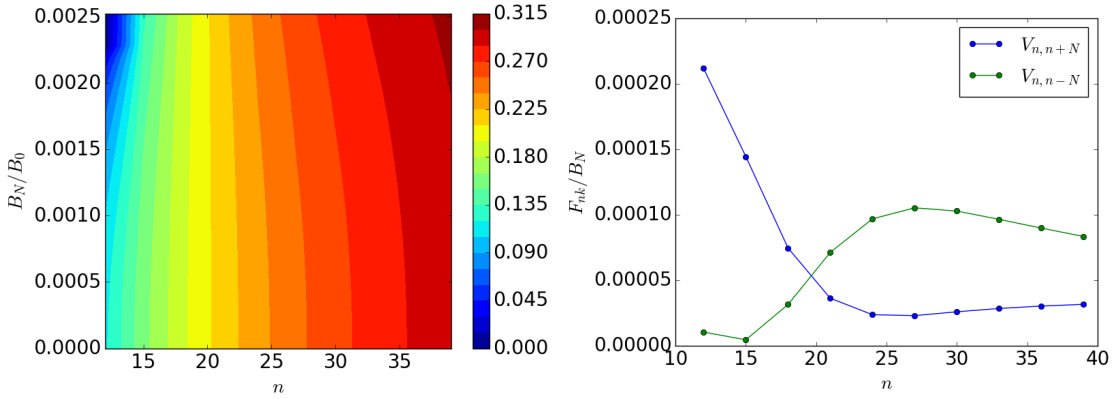

(A) (B)

FIGURE 4.18: (A) The growth rate of 3D peeling-ballooning triplets $n-N, n, n+N$ as a function of primary toroidal mode n and applied field strength B_N/B_0. (B) The normalised coupling coefficients $|F_{nk}|/B_N$ as a function of primary toroidal mode n. This case corresponds to the resonant $N = 3$ MP field.

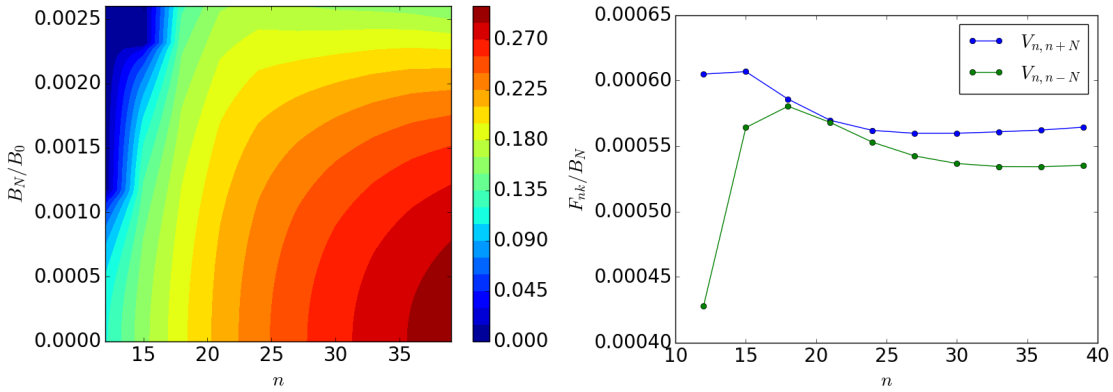

(A) (B)

FIGURE 4.19: (A) The growth rate of 3D peeling-ballooning triplets $n-N, n, n+N$ as a function of primary toroidal mode n and applied field strength B_N/B_0. (B) The normalised coupling coefficients $|F_{nk}|/B_N$ as a function of primary toroidal mode n. This case corresponds to the non-resonant $N = 3$ MP field.

destabilisation of ballooning modes in the presence of the external perturbation. Although for experimentally relevant MP field amplitude $B_N/B_0 \sim 2 \cdot 10^{-3}$, the increase in the growth rate is marginal, $\sim 5\%$. However, low n modes seem to become more stable in the presence of the external field. Fig.4.18b shows the dependence of the coupling coefficients F_{nk} on the primary toroidal mode n of the triplet and as can be observed for all primary modes of $n < 20$ get more stable since $F_{nn+N} > F_{nn-N}$, while primary modes of $n > 20$ get more unstable since $F_{nn+N} < F_{nn-N}$.

Considering the non-resonant case, Fig.4.19a illustrates the growth rate of the

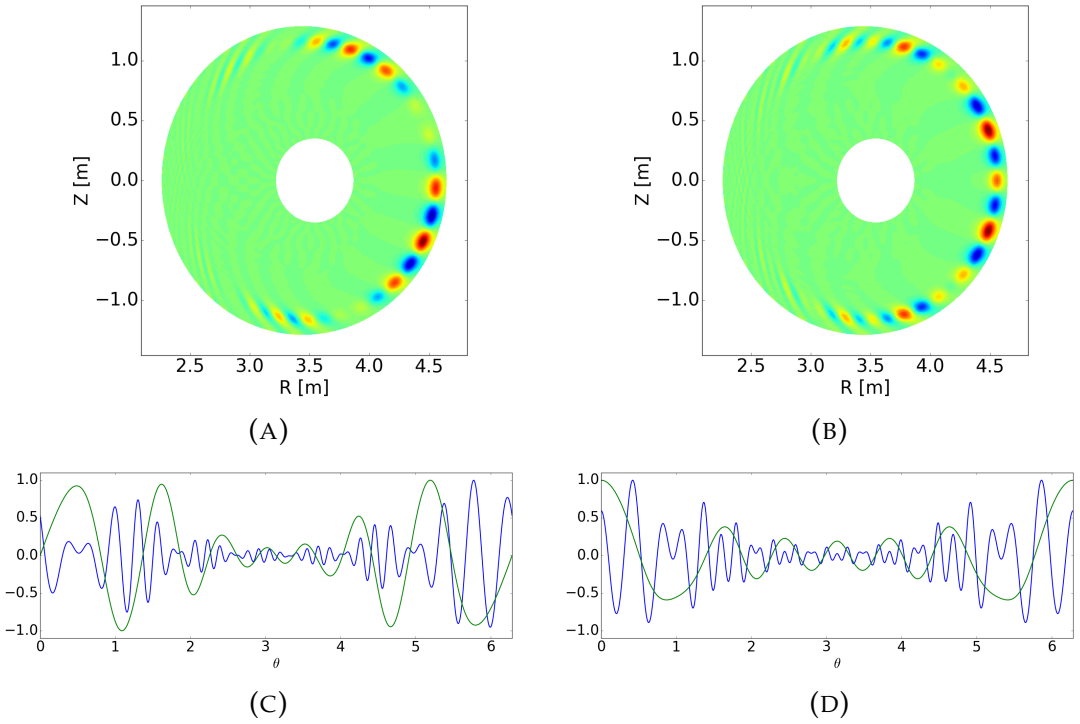

FIGURE 4.20: (A),(B) The reconstruction of the 3D peeling-ballooning mode structure of a $n = 12$ triplet mode for $B_N/B_0 \sim 1.5 \cdot 10^{-3}$. (C),(D) The poloidal angle dependence of the triplet mode (blue line) in comparison to the non-axisymmetric surface displacement (green line) of the plasma response, at the flux surface where the mode is maximised. The resonant case are (A),(C) and the non-resonant case are (B),(C).

triplet mode $\{n - N, n, n + N\}$ as a function of toroidal mode number of the primary mode n and applied field strength B_N/B_0. As can be observed, a decrease in the growth rate occurs indicating stabilisation of ballooning modes in the presence of the external perturbation. Fig.4.19b shows the dependence of the coupling coefficients F_{nk} on the primary toroidal mode n of the triplet and as it can be observed for all primary modes the 3D peeling-ballooning modes become less unstable since is always $F_{nn+N} > F_{nn-N}$. It is interesting to notice, that although the plasma response in the non-resonant case is smaller than the resonant case, stronger toroidal coupling is observed in the non-resonant case. This indicates the importance of the resulting poloidal spectrum of the plasma response, rather than its absolute magnitude, in order to have a significant impact on plasma stability.

Furthermore, the existence of a triplet mode indicates that in the case of sufficiently high coupling a beat structure should form. Such a feature can be observed in Fig.4.20 where a 3D peeling-ballooning mode of primary toroidal

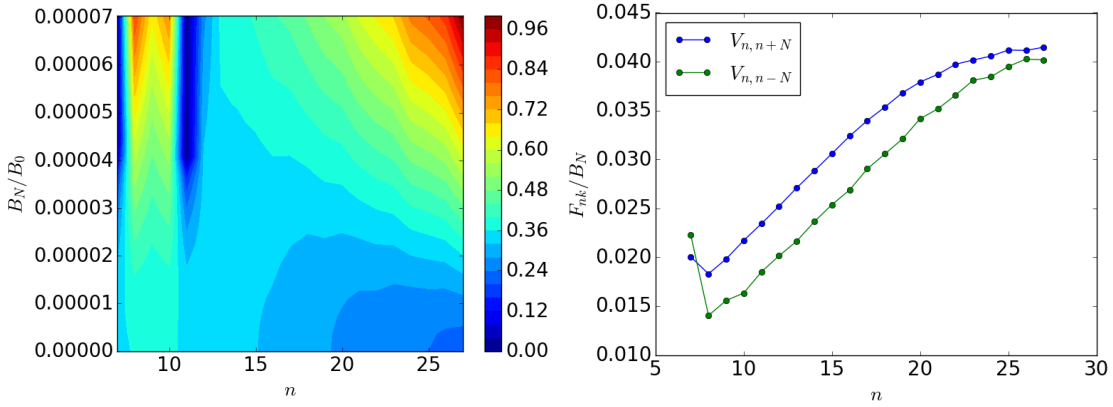

(A) (B)

FIGURE 4.21: (A) The growth rate of 3D peeling-ballooning triplets $n-N, n, n+N$ as a function of primary toroidal mode n and applied field strength B_N/B_0. (B) The normalised coupling coefficients F_{nk}/B_N as a function of primary toroidal mode n. This case corresponds to the resonant $N = 3$ MP field for the $dbm9$ equilibrium.

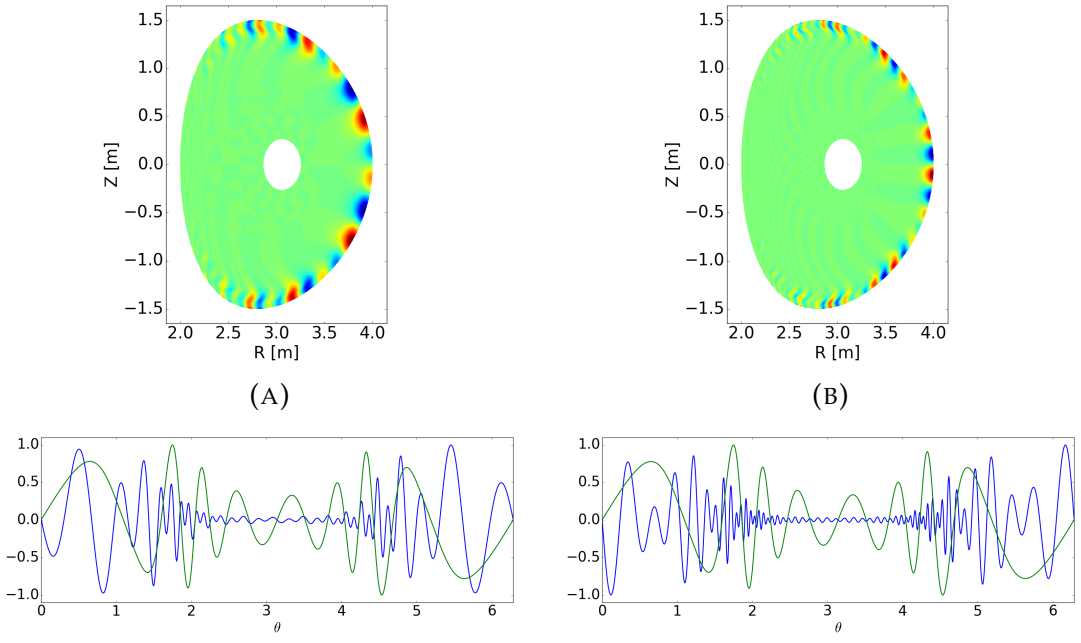

(A) (B)

(C) (D)

FIGURE 4.22: The reconstruction of the 3D peeling-ballooning mode structure of the (A) $n = 9$ and (B) the $n = 18$ triplet mode for $B_N/B_0 \sim 10^{-4}$. The poloidal angle dependence of the (C) $n = 9$ and (D) $n = 18$ triplet mode (blue line) in comparison to the non-axisymmetric surface displacement (green line) of the plasma response, at the flux surface where the mode is maximised.

mode $n = 12$ is plotted considering $B_N/B_0 \sim 1.5 \cdot 10^{-3}$ for the resonant and non-resonant case. The peeling-ballooning mode preferentially sits close to locations where the plasma response, i.e. the non-axisymmetric equilibrium

displacement, crosses zero $\boldsymbol{\xi}_N \cdot \boldsymbol{n} \sim 0$. A similar feature has been observed through infinite n ballooning stability calculations on experimental MP cases in MAST and AUG [71], [118].

Moreover, the D-shaped equilibrium $dbm9$ is used in order to explore the impact of external MPs to a growth rate spectrum where an extremum in the growth rate spectrum occurs. In this case, strong destabilisation occurs at triplets with primary mode number $n \sim 8$. The strongest destabilisation does not occur exactly at the triplet with the most unstable axisymmetric mode, i.e. $n \sim 10$. Since destabilisation depends on the difference of the axisymmetric growth rates, $n \sim 8$ couples to modes that do have smaller growth rate but their difference is minimum, shifting the location of the peak to lower n. Such a feature indicates the importance of the choice of the imposed toroidal mode N from the MP in relation to growth rate spectrum of the axisymmetric peeling-ballooning modes. In addition, strong destabilisation is observed for high n modes, indicating once again that the external field can further destabilise ballooning modes. Fig.4.21 illustrates the 3D growth rate as a function of applied field strength B_N/B_0 and primary toroidal mode number n, as well as the amplitude of the coupling coefficients $|F_{nk}|$. Fig.4.22 illustrates the reconstructed mode structure of a $n = 9$ triplet close to the kink peak, and $n = 18$ triplet away from the kink peak at $B_N/B_0 \sim 10^{-4}$; once again it can be observed that the mode sits at locations where the plasma response vanishes $\boldsymbol{\xi}_N \cdot \boldsymbol{n} \sim 0$.

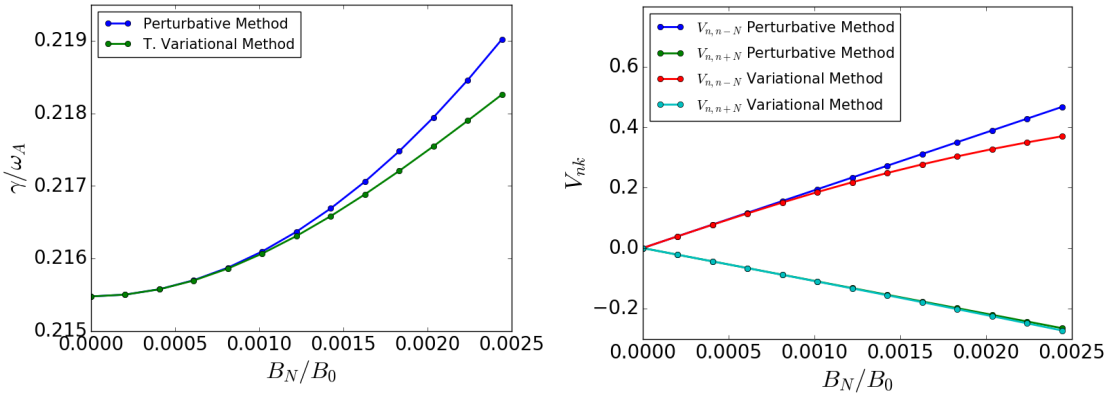

(A) (B)

FIGURE 4.23: Comparison of (A) the normalised growth rate and (B) the coupling coefficients V_{nk} between the perturbative method and the toroidal variational method for a triplet mode of primary mode number $n = 21$ as a function of applied field strength B_N/B_0.

Finally, it should be noted that in the $dbm9$ equilibrium case the toroidal coupling is strong even at $B_N/B_0 \sim 10^{-4}$, leading to potential break down of the perturbative approach that requires weak coupling between the toroidal normal modes. As a result, it is required to use a an approach that in principle allows strong coupling between the modes of the basis under consideration. Therefore, a variational method is more appropriate to examine the 3D stability of the plasma especially for high β_N plasmas which were shown to lead to much stronger toroidal coupling.

4.5 Variational Stability Analysis

In the previous section we showed that for high β_N plasmas, strong coupling occurs between the axisymmetric normal modes, such that a variational method is required. Using as basis functions the axisymmetric normal modes, two approaches become available; one considers toroidal coupling of axisymmetric normal modes, while the other uses the individual poloidal harmonics that make up the axisymmetric normal modes as described in Chapter3. This means that non-axisymmetric effects will change the coupling between the poloidal modes.

4.5.1 Coupled Toroidal Normal Modes

In this section, we use the full axisymmetric normal modes as our basis functions, to enable a straight comparison with the perturbative method. Considering once again the $cbm18\_dens6$ equilibrium, a similar analysis is performed. Initially, only first neighbour coupling is taken into account and for applied field strength $B_N/B_0 < 10^{-3}$ where weak coupling occurs the variational method should result the same outcome as the perturbative method. Fig.4.23 illustrates a comparison for the growth rate and the coupling coefficients between the two approaches considering a triplet mode with primary toroidal mode number $n = 21$. As can be observed up to $B_N/B_0 \sim 10^{-3}$ the two approaches agree very well, but as the field strength is increased a disagreement starts to build up and the two approaches diverge. The growth rate of the triplet in the variational case is observed to increase slower with the

applied field since the coupling to the destabilising lower n modes becomes weaker in this case. In addition, in the perturbative analysis, the assumption of weak toroidal coupling means that the coupling coefficient of the primary mode n is unity, i.e. $c_n = 1$. In the variational approach this assumption is relaxed and $c_n \neq 1$ such that the perturbative method results in unphysical behaviour as B_N/B_0 increases.

Furthermore, the variational method allows the coupling of multiple toroidal normal modes. Since perturbation theory deviates at $B_N/B_0 \sim 10^{-3}$, it is expected that strong coupling occurs requiring more toroidal normal modes to be retained. As can be observed from Fig.4.24, with increasing applied field

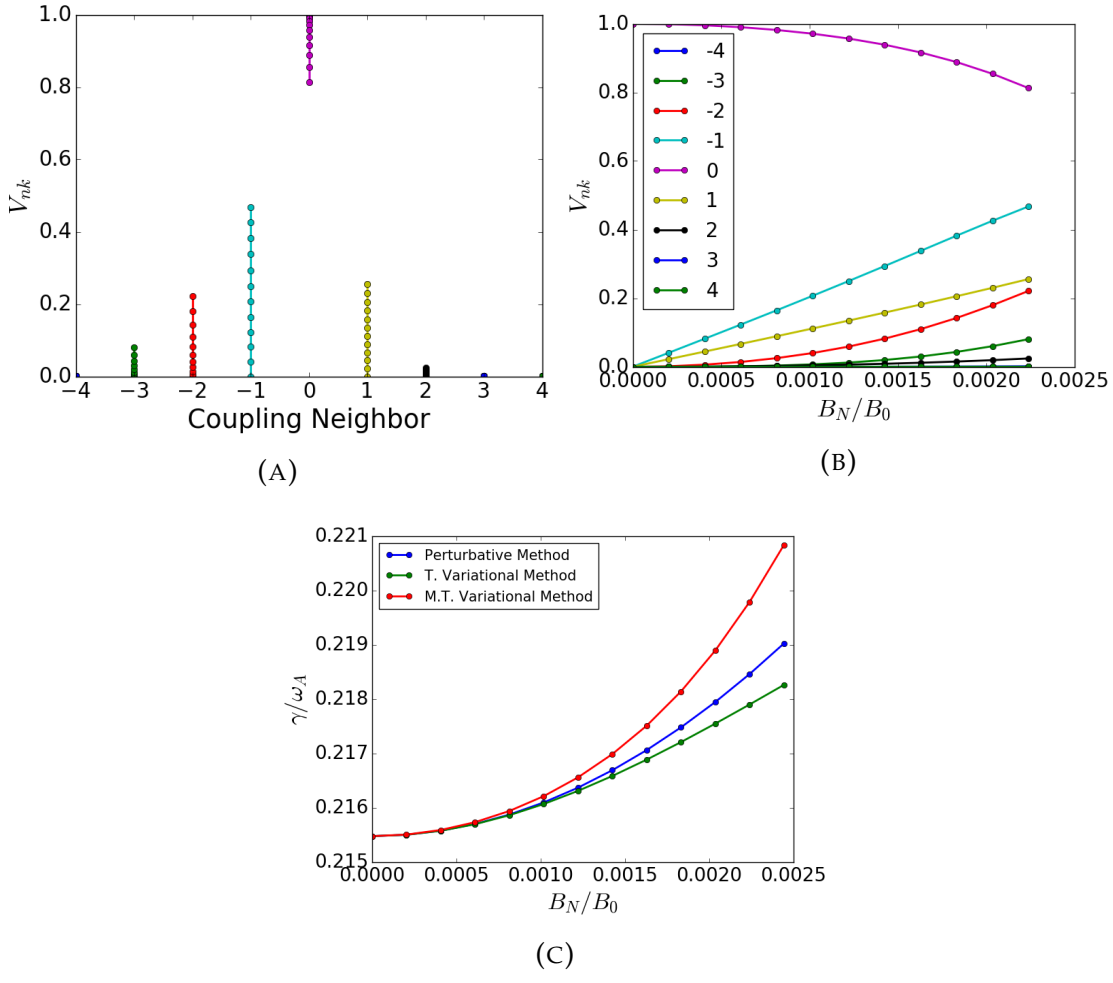

FIGURE 4.24: The coupling coefficients of the multi-mode variational method, (A) as a function coupling neighbour and (B) applied field strength B_N/B_0 considering coupling between 9 axisymmetric normal modes. (C) Illustrates a comparison between the perturbative, toroidal variational and toroidal multi-mode variational methods.

	Growth Rate	***Balloon***	***Kink***	***Bending***
n=12				
ELITE	0.1096	-2.858E-02	-3.838E-03	2.905E-02
Reconstruct	0.1134	-2.907E-02	-3.615E-03	2.974E-02
n=15				
ELITE	0.1550	-4.325E-02	-4.648E-03	4.095E-02
Reconstruct	0.1582	-4.404E-02	-4.451E-03	4.204E-02
n=18				
ELITE	0.1876	-7.308E-02	-6.514E-03	6.536E-02
Reconstruct	0.1869	-7.448E-02	-6.298E-03	6.731E-02

TABLE 4.1: Comparison of growth rates and energy contribution in terms of destabilising ballooning and kink/peeling terms and stabilising field line bending between the ELITE result and the reconstructed result for the $cbm18\_dens6$ equilibrium case.

	Growth Rate	***Balloon***	***Kink***	***Bending***
n=9				
ELITE	0.3682	*N.A.*	*N.A.*	*N.A.*
Reconstruct	0.3312	-2.901E-02	-5.527E-002	6.112E-02
n=12				
ELITE	0.3879	*N.A.*	*N.A.*	*N.A.*
Reconstruct	0.3685	-1.705E-02	-2.944E-002	3.339E-02
n=15				
ELITE	0.3941	*N.A.*	*N.A.*	*N.A.*
Reconstruct	0.3897	-1.631E-02	-2.618E-02	3.033E-02

TABLE 4.2: Comparison of growth rates and energy contribution in terms of destabilising ballooning and kink/peeling terms and stabilising field line bending between the ELITE result and the reconstructed result for the $dbm8$ asymmetric equilibrium case.

multi-mode coupling takes place and in this case for $B_N/B_0 \sim 2.5 \cdot 10^{-3}$ even 3^{rd} neighbouring coupling is required, and further destabilisation is observed due to the inclusion of additional degrees of freedom. The 3D $n = 12$ mode couples strongly to lower n neighbours as indicated from the perturbative method with the 3^{rd} neighbour contributing $\sim 10\%$. In addition, the stronger coupling to lower n modes leads to further destabilisation, as can be observed from the Fig.4.24. In addition, it can be observed that with increasing field strength B_N/B_0 the perturbative assumption $c_n = 1$ is violated and the approach becomes inaccurate.

4.5.2 Coupled Toroidal & Poloidal Normal Modes

Neither the perturbative method nor the toroidal variational method allows changes in the coupling of poloidal modes in the individual axisymmetric normal modes. Since the applied field is composed of a wide range of poloidal harmonics, and strong coupling takes place at experimentally relevant applied fields, it is expected that the poloidal coupling within each axisymmetric normal mode will be affected as well. To test this hypothesis, we allow the coupling between the poloidal harmonics to change. However, also in this case the axisymmetric potential and kinetic energy matrices need to be reconstructed. The reconstruction of those matrices is performed in two ways. In the first way, those matrices are input variables and taken from ELITE, provided the plasma is up-down symmetric or the low n version is not used. In the second way, those matrices are calculated considering the axisymmetric δW and δK for the displacement ELITE provides and so even non-symmetric plasmas or low n modes can be considered.

To begin with, the $cbm18\_dens6$ equilibrium is used in order to verify that the calculation of the axisymmetric matrices is correct. As can be observed from Table.4.1, where a comparison of the growth rate and destabilising/stabilising energy contributions are listed, the reconstruction agrees with the ELITE result. Additionally, a non-symmetric equilibrium $dbm8$ is examined and reproduces well the ELITE growth rate as shown in Table.4.2.

At this stage, where the axisymmetric energies can be computed accurately, the impact of the applied field on the poloidal mode coupling can be examined. The $cbm18\_dens6$ is considered initially for the resonant $N = 3$ MP perturbation used previously. Fig.4.25 illustrates the growth rate of 3D peeling-ballooning modes as a function of primary toroidal mode n and applied field strength B_N/B_0. Initially, only first neighbour toroidal coupling is considered, i.e. triplet modes $\{n - N, n, n + N\}$, retaining all the constituent poloidal harmonics and allowing freedom in the poloidal coupling. From Fig.4.25a and Fig.4.25b it becomes apparent that the freedom in the poloidal coupling results in strong destabilisation of the ballooning mode, and for an applied field of $B_N/B_0 \sim 2 \cdot 10^{-3}$ the growth rate increased by $\sim 60\%$ in comparison to the previous methods where only a difference of $\sim 5\%$ occurred. The applied field interacts strongly with specific poloidal harmonics minimising in such a way field line

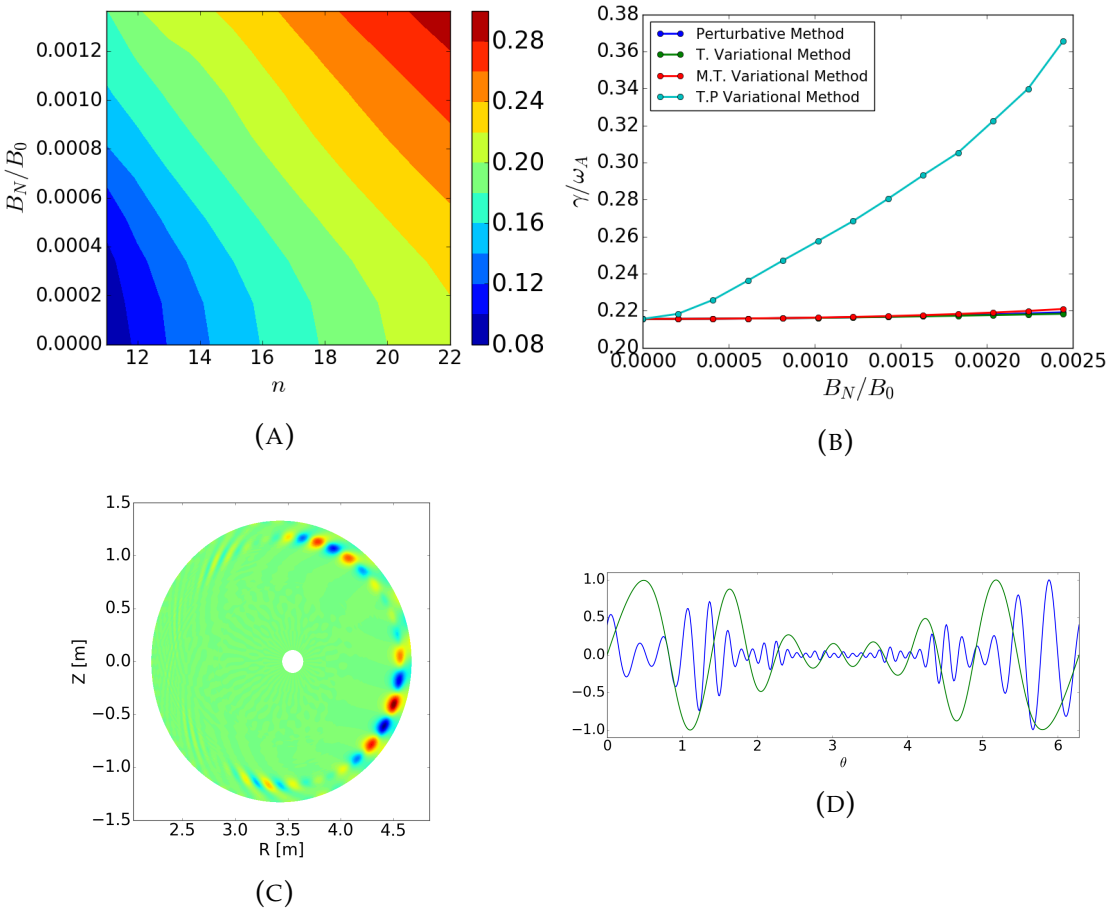

FIGURE 4.25: (A) The growth rate of the 3D triplet modes as a function of primary toroidal mode n and applied field strength B_N/B_0 for a resonant N=3 MP. (B) Comparison between the different perturbative and variational methods for a $n = 21$ triplet mode as a function of B_N/B_0. (C) The reconstruction of the mode structure of a $n = 12$ triplet and (D) the poloidal variation of the $n = 12$ triplet (blue line) in comparison to the plasma response (green line).

bending and maximising the driving terms. However, from Fig.4.25c and Fig.4.25d it can be concluded that the resulting mode structure is in good agreement with the perturbative method. Although, direct comparison of the coupling coefficients is not possible, as the toroidal coefficients are replaced by a set of toroidal/poloidal coefficients, the difference in poloidal spectrum of the axisymmetric normal mode to the 3D mode can be studied. Fig.4.26 illustrates the relative amplitude of the poloidal coupling for each axisymmetric normal mode in relation to the poloidal coupling of the 3D mode. As can be observed, the poloidal coupling is affected by the applied field and in this case pushes the ballooning mode outwards, while excitation occurs for external poloidal harmonics. In addition, the inclusion of poloidal coupling leads to a different

relative coupling in comparison to the perturbative method since the higher sideband $n + N$ is observed to be the one with the higher amplitude. Within the perturbative method stabilisation would be expected, but the observed destabilisation is attributed to the different structure of the normal modes.

Furthermore, the impact of MPs is examined with respect to β_N and $\Delta\phi$, where $\Delta\phi$ is the parity of the current at the top and bottom row of coils with respect to the mid-plane. The $cbm18\_dens6$, $cbm18\_dens7$ and $cbm18\_dens8$ equilibria are considered such that $\beta_N = [1.65, 1.99, 2.35]$ with $q_a = [2.97, 3.01, 3.04]$. Fig.4.27a illustrates the dependence on β_N for a $n = 15$ triplet mode considering the resonant $N = 3$ MP. As can be observed, further destabilisation due to the applied MP is observed in all three cases. In addition, it can be observed that the relation is linear for low B_N/B_0 and becomes nonlinear as $B_N/B_0 \sim 10^{-3}$. The stronger destabilisation that occurs in the case where $\beta_N = 2.35$ is not attributed only to the larger response. For a fixed normal magnetic field at the plasma boundary a larger plasma response, i.e. normal flux surface displacement, is expected with increasing β_N. However, since the relation is not linear it can be concluded once again that the poloidal mode structure of the applied MP

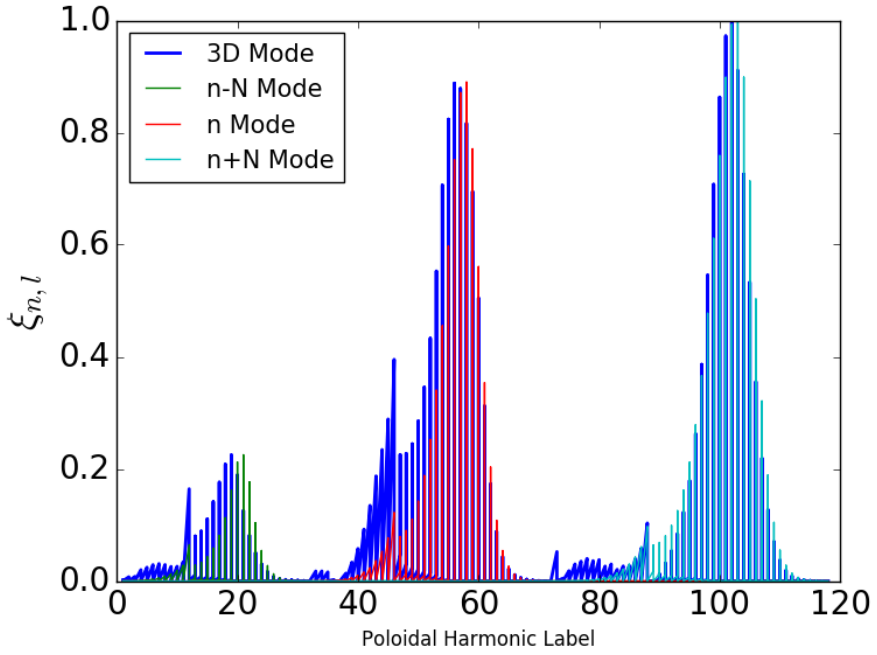

FIGURE 4.26: A comparison between the axisymmetric modes and the 3D triplet mode for the relative amplitude of the constituent poloidal harmonics for each toroidal normal mode of the $n = 12$ triplet for $N = 3$ and $B_N/B_0 \sim 1.5 \cdot 10^{-3}$.

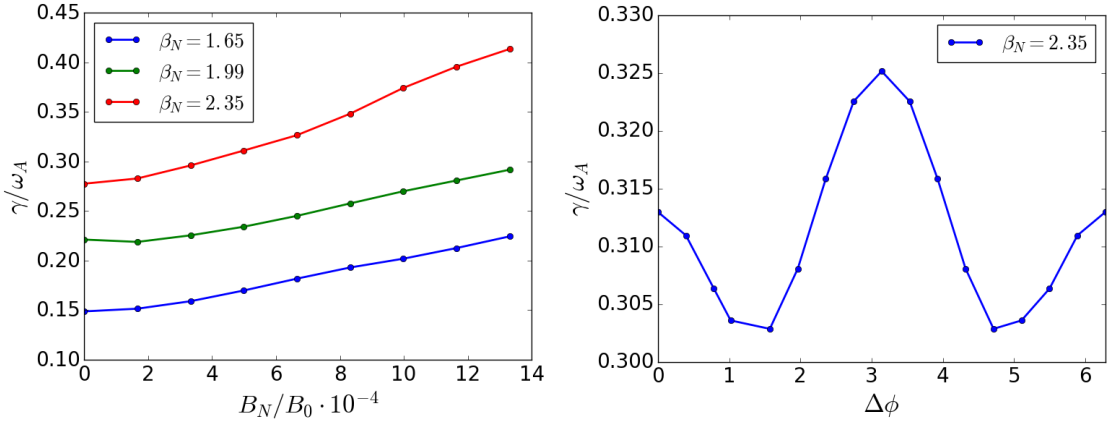

(A) (B)

FIGURE 4.27: (A) The normalised growth rate of the $n = 15$ triplet as a function of the applied field strength B_N/B_0 for different β_N. (B) The dependence of the $n = 15$ triplet on the phase $\Delta\phi$ of the imposed MP for the $\beta_N = 2.35$ equilibrium case.

itself is a crucial factor for the plasma stability. Moreover, Fig.4.27b illustrates the dependence of the $n = 15$ triplet for the $\beta_N = 2.35$ case on the applied MP phase, where $\Delta\phi = 0$ is the resonant MP and $\Delta\phi = \pi$ is the non-resonant MP and $B_N/B_0 = 5 \cdot 10^{-4}$. It should be noted that this phase indicates the transition between a resonant and a non-resonant applied MP, since if a free boundary response was computed a different result would be expected to occur with $\Delta\phi$. Nevertheless, it can provide an insight on the resonance that can occur between the imposed field and the plasma surface. As can be observed, the most unstable case occurs for the non-resonant case, although the plasma response is smaller. This indicates once again the importance of the poloidal spectrum of the MP.

The $dbm9$ equilibrium case has also been examined as it represents a more experimentally relevant case, and again the $N = 3$ resonant MP field is considered. Fig.4.28 illustrates the growth rate of the triplet modes as a function of primary toroidal mode n and applied field strength B_N/B_0. The growth rate of primary modes that exhibit the largest growth rate with respect to their triplet are significantly destabilised by a factor of ~ 2.8. The rest of the primary modes are also observed to be further destabilised but at lower levels and again this provides an indication that ballooning modes become more unstable with the applied MP. This observation is similar to the perturbative method where strong destabilisation occurred at modes around the peak of the growth spectrum. However, the resulting change in the growth rate in the variational

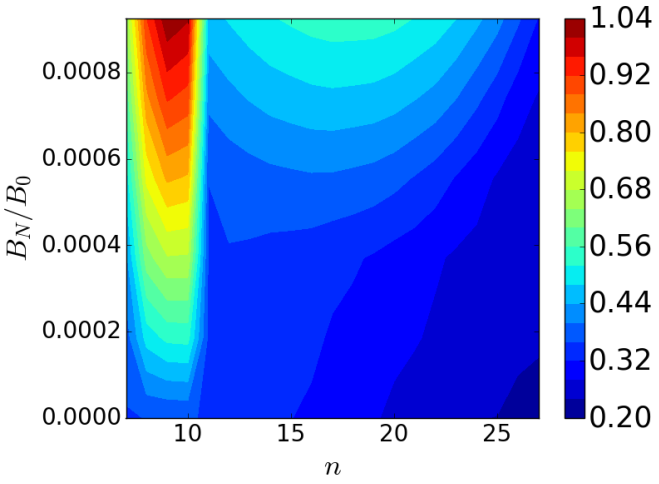

FIGURE 4.28: Growth rate of the 3D triplet modes as a function of the primary toroidal mode number n and applied field strength B_N/B_0 for the $dbm9$ equilibrium case and a $N = 3$ resonant applied MP.

method is significantly lower than the perturbative method, indicating a break down of the perturbative method when the coupling coefficients are not small. An additional interesting feature that occurs, is the complete reorganisation of modes away from the kink peak of the growth rate spectrum. Fig.4.29 and Fig.4.30 illustrates the $n = 9$ triplet and $n = 18$ triplet for $B_N/B_0 \sim 10^{-4}$ and $B_N/B_0 \sim 10^{-3}$. As can be observed, the $n = 9$ triplet has a different structure in comparison to the perturbative method and the structure does not significantly change with an increasing B_N/B_0. On the other hand, the $n = 18$ triplet for low B_N/B_0 is similar to the perturbative method, but for higher B_N/B_0 the mode is reorganised with the external kink poloidal harmonics being minimised and the 3D mode is pushed radially inwards.

Finally, especially for the $dbm9$ equilibrium case where strong toroidal coupling is observed even for small B_N/B_0, the impact of multi-mode coupling of the toroidal normal modes is examined, including freedom in the relative poloidal coupling. The $n = 18$ mode is considered as the primary harmonic of a triplet $\{n-N, n, n+N\}$, a quintuplet $\{n-2N, n-N, n, n+N, n+2N\}$ and a septuplet $\{n-3N, n-2N, n-N, n, n+N, n+2N, n+3N\}$ 3D mode for $B_N/B_0 \sim 10^{-3}$. As can be observed from Fig.4.31a, strong coupling occurs between the individual toroidal normal modes even considering a septuplet mode. The relative shape of the poloidal spectrum of the individual normal modes is not significantly altered by considering more normal modes in the coupling, but their relative

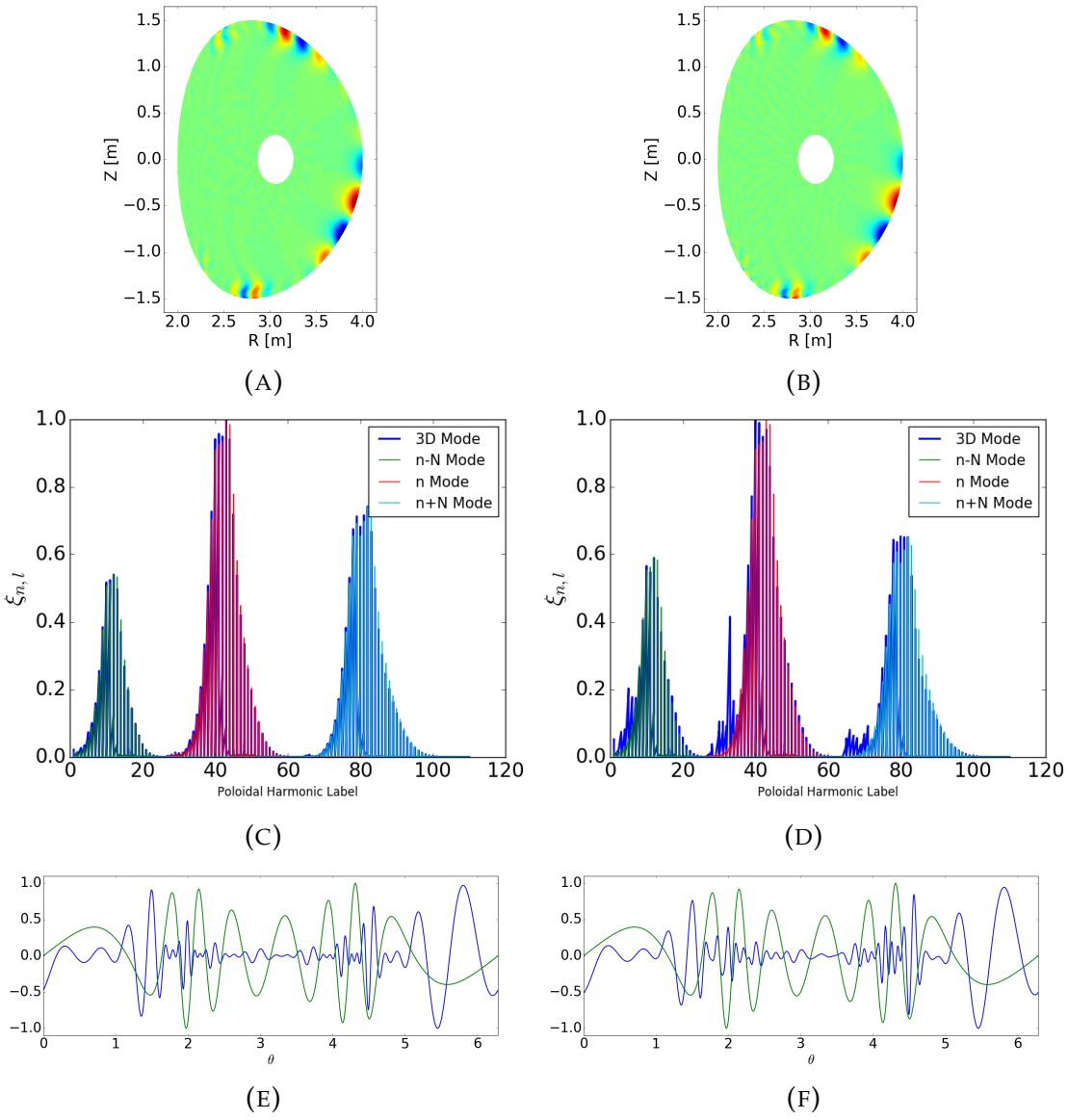

FIGURE 4.29: The reconstruction of the $n = 9$ triplet mode, a comparison between the axisymmetric modes and the 3D triplet mode for the relative amplitude of the constituent poloidal harmonics for each toroidal normal mode and the poloidal dependence of triplet mode for $N = 3$ and for (A), (C), (E) $B_N/B_0 \sim 10^{-4}$ and (B), (D), (F) $B_N/B_0 \sim 10^{-3}$ applied MP.

amplitude changes. This results in a significantly more poloidal localised 3D mode minimising field line bending, such that the growth rate of the mode increases further, from $\gamma/\omega_A = 0.55$ for the triplet to $\gamma/\omega_A = 0.62$ for the quintuplet.

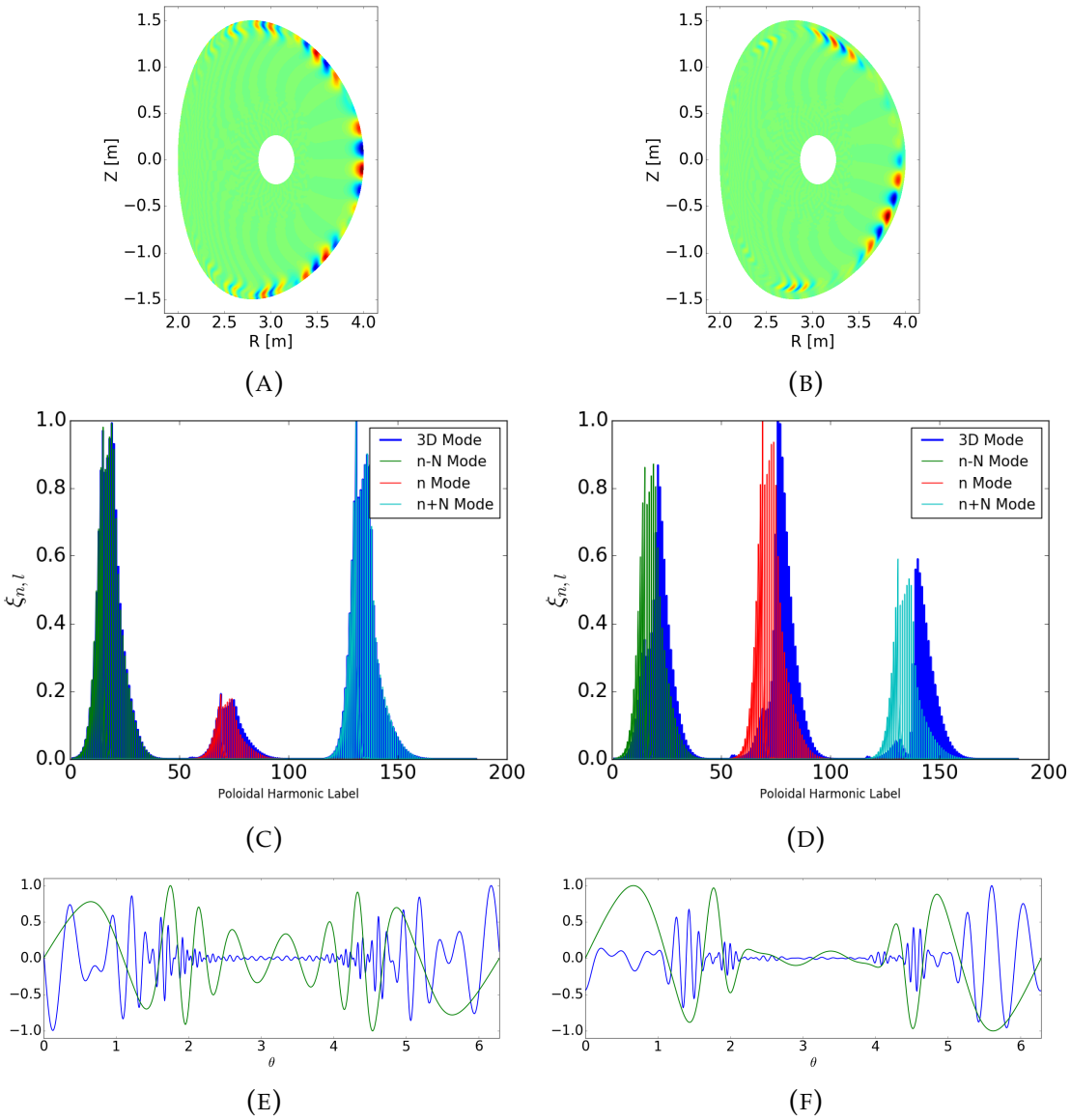

FIGURE 4.30: The reconstruction of the $n = 18$ triplet mode, a comparison between the axisymmetric modes and the 3D triplet mode for the relative amplitude of the constituent poloidal harmonics for each toroidal normal mode and the poloidal dependence of triplet mode for $N = 3$ and for (A), (C), (E) $B_N/B_0 \sim 10^{-4}$ and (B), (D), (F) $B_N/B_0 \sim 10^{-3}$ applied MP.

4.6 Summary

The low n ELITE ideal linear MHD stability code was used within a numerical framework to calculate both the ideal linear plasma response and the 3D ideal linear MHD stability of tokamak plasmas, under the application of external non-axisymmetric MP fields.

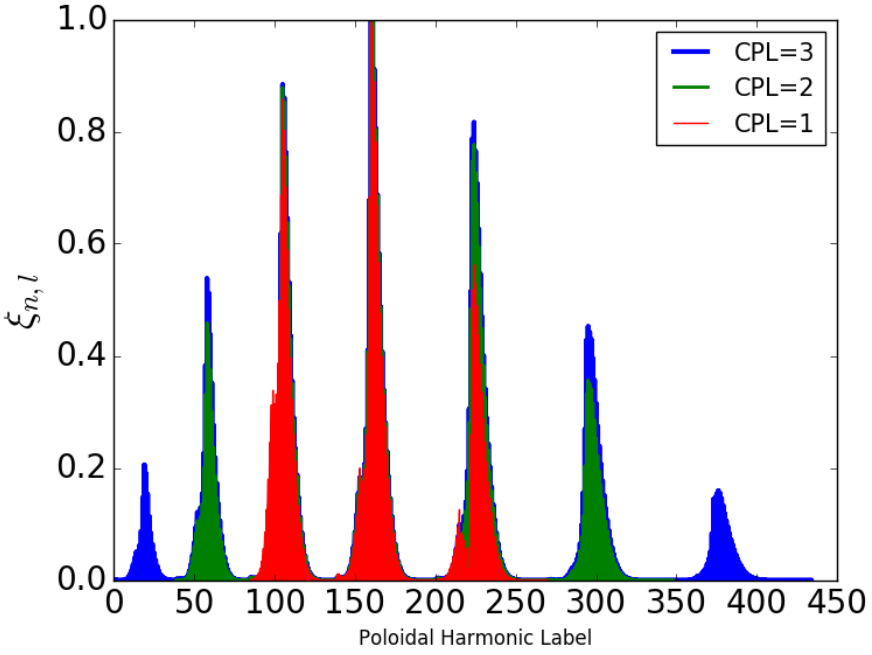

(A)

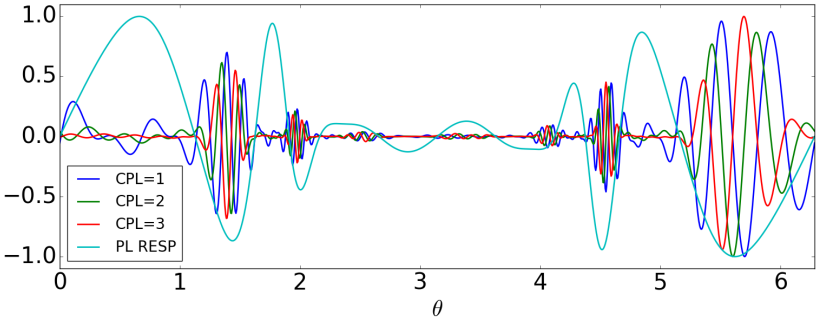

(B)

FIGURE 4.31: (A) The relative amplitude of individual poloidal harmonics of the toroidal normal modes as a function of their poloidal harmonic label, considering a primary mode of $n = 18$ for $B_N/B_0 = 10^{-3}$ and multi-mode coupling. (B) Illustrates the poloidal dependence of the 3D mode with respect to plasma response.

Benchmark studies were presented for the ideal linear plasma response between ELITE and BOUT++, as well as MARS-F. Satisfactory agreement was obtained considering the differences in the numerical methods, the reduced set of MHD equations in BOUT++ and MARS-F, as well as the small differences in the equilibrium input files that each code uses.

The 3D ideal MHD stability was studied using two methods. The first approach used second order perturbation theory to treat the applied 3D fields as a

perturbation of the original axisymmetric system. As such, basis functions can be constructed from the toroidal normal modes of the axisymmetric system, to calculate correction terms in the mode structure and growth rate of the 3D mode. Such a procedure leads to triplet modes $\{n - N, n, n + N\}$ reducing significantly the numerical complexity of the 3D system. In general, it was observed that ballooning modes become more unstable and field-aligned localisation is observed. However, for experimentally relevant high β_N plasmas, the original assumptions that justify the use of a perturbative method break down, leading to unrealistic results.

The second approach used variational theory and the toroidal normal modes of the axisymmetric system as basis functions for the structure of the 3D modes, to minimise the 3D energy functional that is a result of the total non-axisymmetric plasma equilibrium. The variational approach allows the relaxation of the assumptions that perturbation theory requires, i.e. weak toroidal coupling, and allows the minimisation of the toroidal as well as the poloidal coupling of the constituent basis functions. The stability of the system is observed to be in general reduced from the 3D applied fields. Ballooning modes are observed to be further destabilised and field-aligned localisation is observed in a similar manner to the results obtained with perturbation theory. However, the system was further destabilised due to the additional degrees of freedom. In addition, for experimentally relevant plasmas that become kink unstable at high β_N, extrema (maxima) in the growth rate spectrum can occur. The application of 3D fields highly destabilises the most unstable kink modes, due to an unstable synergistic toroidal coupling from the neighbouring toroidal modes. This behaviour can be analytically understood using perturbative arguments. Finally, the variational method allows for multi-toroidal mode coupling, which is required in cases of strong toroidal coupling. Further destabilisation of the 3D system was observed due to the additional degrees of freedom.

Chapter 5

Conclusion

5.1 Discussion & Future Development

The linear stability of quasi-axisymmetric tokamak plasmas is examined within a numerical framework based on the eigenvalue axisymmetric stability code ELITE. The framework initially computes the linear plasma response, i.e. the 3D equilibrium component, and the axisymmetric peeling-ballooning eigenfunctions. Considering perturbative and variational methods all this information is used to approximate the 3D stability of ideal MHD normal modes.

To begin with, the linear plasma response is computed assuming a fixed boundary condition at the plasma-vacuum interface. This assumes prior knowledge of the total 3D magnetic field, as the plasma itself will alter the vacuum field produced from the MP coil configuration. Although this provides a simplified way to compute 3D equilibria, it is sufficient to examine the impact of 3D fields on the stability of the tokamak plasma. The fixed boundary response was benchmarked with BOUT++ and MARS-F. With BOUT++ an idealised circular cross-section large aspect ratio plasma was considered and agreement was obtained between BOUT++ and ELITE. ELITE can accommodate significantly higher radial resolution, requires no numerical dissipation and therefore was able to capture sharp features at the rational surfaces. The benchmark with MARS-F was performed for an AUG experimental equilibrium and the free boundary response was provided as a

boundary condition in ELITE. The outcome was satisfactorily similar to the MARS-F result. Nevertheless, some difference occurred close to the X-point region, and this is attributed to an oscillatory behaviour of the equilibrium input for ELITE. By means of artificial smoothing of this oscillatory behaviour, a better match could be obtained. Finally, ELITE can be used to obtain the free boundary plasma response provided the vacuum magnetic inductance and the plasma inductance are known in the plasma-vacuum interface. The vacuum inductance is a function of the coil configuration and the plasma surface coordinates, while the plasma inductance relates a change in the potential energy to the perturbed current density and flux poloidal magnetic flux. Such a method has been successfully used with DCON [119] leading to the IPEC framework. In a similar way, ELITE can provide the plasma inductance and the vacuum inductance can be calculated by modification of the vacuum code used currently within the framework. This will be part of future work.

The linear 3D stability is examined first using a perturbative method as suggested by [76]. The perturbative approach assumes small disturbance of the flux surfaces that in turn leads to a 3D force operator which is of order $\epsilon \ll 1$ with respect to the axisymmetric force operator. As a result, weak coupling occurs leading to a triplet $\{n-N, n, n+N\}$ that represents the 3D mode for primary mode number n. The 3D equilibrium profiles and the geometrically induced coupling of toroidal modes [105] had a significant impact on MHD modes above a certain phenomenological threshold for the amplitude of the applied field. For the $cbm18\_dens6$ equilibrium case, the growth rate is enhanced by the MP in the case of a resonant applied field, due to stronger coupling with the lower n sideband. On the other hand, decrease of the linear growth rate is observed due to stronger coupling with the higher n sideband of the axisymmetric system in the non-resonant case. For the $dbm9$ equilibrium case, where extrema exist in the growth rate spectrum, a strong destabilisation is observed for modes close to the peak of the growth rate spectrum. In both cases, the reconstruction of the 3D mode in the poloidal cross-section resulted in poloidal localisation of the mode close to specific locations where the displacement of the linear response crosses zero, i.e. $\xi_N \sim 0$.

The coupling of toroidal harmonics by MPs can significantly influence the ballooning instability even for a low MP field of $B_N/B_0 \sim 10^{-3}$. This then raises questions about the validity of the perturbative approach, without taking

into account the influence of the MP field on the axisymmetric poloidal mode structure of the triplet. In order to resolve such an issue, a more general variational approach original to this work is followed. This uses the individual poloidal and toroidal Fourier modes from the axisymmetric normal modes as a basis for trial functions, summing over them with coefficients to be determined by minimisation of the energy functional. This provides significantly more degrees of freedom, allowing the MP field to influence the ballooning structure of each constituent axisymmetric mode.

The variational method revealed the impact of the MP field in the poloidal coupling of the individual axisymmetric normal modes. The change in the poloidal coupling of the basis functions resulted in further destabilisation for ballooning modes. Especially, in cases where strong toroidal coupling is observed, for example in the $dbm9$ equilibrium case, the peeling-ballooning mode was completely reorganised and it was observed that the kink component of the instability, i.e. poloidal harmonics that resonate at the vacuum region, were suppressed for sufficiently high applied field B_N/B_0. However, for toroidal modes close to the peak, the external kink-like structure was retained, and those modes were highly destabilised. Such a feature could be relevant for experimental high β_N plasmas, where unstable internal or external kink modes are expected for low n modes. The significant increase in the growth rate of the most unstable kink mode potentially indicates a faster ELM crash of similar mode number n, a feature which is observed experimentally in ELM mitigation. In addition, since plasma shaping is important for the stabilisation of low n kink modes, ELM suppression could be a manifestation of the absence of a strong kink peak, that could result in faster growing high n ballooning modes that result in softer transport, i.e. no ELM crash. In any case, plasma stability seems to be degraded by the applied MP field and could provide an insight in experimental observation that suggests unstable plasmas in regions where the axisymmetric $J_{||} - p'$ diagram indicates stable operation.

Finally, due to strong coupling of toroidal modes, the notion of a triplet mode might be misleading and more toroidal modes may be needed for an accurate representation of the 3D mode. The variational approach allows the inclusion of a whole set of toroidal normal modes. Such a case was examined retaining only toroidal coupling for the $cbm18\_dens6$ equilibrium case and significant contribution from the $\pm 2N$ and $\pm 3N$ sidebands was observed

leading to further destabilisation. A similar analysis was performed for the $dbm9$ equilibrium case, but allowing freedom in the poloidal coupling of the toroidal basis functions, and a similar outcome could be drawn. The inclusion of more toroidal modes resulted in further destabilisation and stronger poloidal localisation of the peeling-ballooning mode. The strong poloidal localisation in 3D geometry is a feature that is observed experimentally in AUG, [118], and was successfully reproduced by theory considering a local ballooning analysis [71]. In those cases the 3D ballooning mode was localised around specific field lines, that coincided with locations where the plasma response crosses zero, i.e. $\xi_N \sim 0$. A numerical investigation in MAST using MPs, revealed similar behaviour for the 3D local ballooning mode. It was shown that for those field lines changes in local torsion lead to strong destabilisation. The perturbative and variational method for low B_N/B_0 provided similar results for the localisation of the mode for the $cbm18$ and $dbm9$ cases. However for higher B_N/B_0, in the variational approach considering the $dbm9$ case, the 3D mode seemed to be shifted towards regions where the flux surfaces are pushed inwards. This could indicate further destabilisation from the sharper pressure gradient in the 3D system, instead of the modification of the local torsion, and the contribution of the kink instability in the mode structure. However, due to the complex interplay of local shear/torsion, curvature and pressure gradient a more rigorous examination is needed with respect to the individual stabilising and destabilising energy terms in 3D geometry.

As a future work, the variational method should be benchmarked with a global 3D stability code to quantitatively verify the growth rate and mode structure of instabilities as well as the region of validity of such an approach, as the radial structure of the individual poloidal harmonics is considered fixed. This assumption is appropriate for intermediate to high n ballooning-like modes but for low n kink/peeling-like modes this assumption might be violated. The VMEC/CASTOR3D framework could be used for low n modes, while the newly developed VMEC/PB3D framework could be used for intermediate to high n modes, in order to benchmark and compare this variational method that minimises the 3D energy functional for a given set of unstable normal modes as obtained form the axisymmetric system. Eventually, this framework could be used as part of a design tool for MP coils that are optimised with respect to the peeling-ballooning stability of the plasma, due to the simultaneous simulation of 3D plasma response and stability, as well as its computational efficiency.

5.2 Summary

H-mode tokamak plasmas are characterised by quasi-periodic instabilities called edge localised modes (ELMs), which transfer particles and heat to plasma facing components and the divertor of the tokamak device. Large scale tokamaks, like ITER, will not be able to cope with the corresponding heat fluxes and so active ELM control methods are required. One promising method applies external non-axisymmetric resonant magnetic perturbations and it has been experimentally demonstrated that ELM mitigation or even complete ELM suppression is possible. This work has focused on understanding the impact of the resulting 3D geometry on the ideal MHD stability of the tokamak plasma. The geometry symmetry breaking leads to the coupling of axisymmetric toroidal MHD modes that allows the exchange of energy between them even in the linear phase, altering the growth rate of unstable peeling-ballooning modes, which are believed to be the cause of ELMs. Qualitatively, depending on the axisymmetric growth rate spectrum, a particular mode can be either stabilised or destabilised. However, a definite trend exists near extrema in the spectrum; minima are always stabilised, while maxima are observed to be always destabilised. In order to examine the impact of mode coupling, perturbation and variational theory are employed to calculate the 3D growth rate and mode structure. The axisymmetric normal modes are postulated to be appropriate trial functions, since the applied field is orders of magnitude lower than the main axisymmetric confining equilibrium field. The perturbative and variational methods require information from the full non-axisymmetric plasma equilibrium and the axisymmetric toroidal modes. As such a numerical framework is constructed based on the axisymmetric stability code ELITE, to obtain the linear plasma response and the toroidal basis functions in order to examine the change in the linear MHD stability for a given MP configuration. The symmetry breaking results in modification of the plasma stability above a critical value of the applied MP field and field-line localisation of the peeling-ballooning eigenmode. It is observed that intermediate to high n ballooning modes are in general destabilised by the applied MP field, while intermediate kink modes can become stable at sufficiently high MP field. Extrema in the growth rate spectrum due to low n kink modes are observed to be strongly destabilised, as predicted by perturbation theory.

We have demonstrated the key elements required for the proposed tool. Plasma response and plasma stability can both be calculated using the ELITE code. Further work will be required to build the code to produce the free boundary plasma response. The final code should then be benchmarked against 3D stability codes for low n modes where comparisons are possible. The testing of the code against experimental results will provide key insights into the physics of ELM mitigation and suppression with MPs.

Appendix A

Appendix: 3D Potential Energy Terms

The calculation of the 3D stability requires the knowledge of the force operator due to a displacement of the plasma equilibrium. The force operator acts on a displacement functional and the eigenvalues and eigenvector define the stability of the 3D system. In order to obtain eigenvalues and eigenvectors, a quadratic integral form is used that relates the potential and kinetic energy change of the system, such as

$$\delta K(\boldsymbol{\delta\xi}_n^*, \boldsymbol{\delta\xi}_n) = \frac{1}{2}\int \boldsymbol{\delta\xi}_n^* \cdot \boldsymbol{\delta\xi}_n \, \mathcal{J}\mathrm{d}\psi\mathrm{d}\theta^*\mathrm{d}\phi \tag{A.1}$$

$$\begin{aligned}\delta W(\boldsymbol{\delta\xi}_n^*, \boldsymbol{\delta\xi}_n) = \frac{1}{2}\int \{|\boldsymbol{\delta B}_{n\perp}|^2 - \frac{\boldsymbol{J_0 \cdot B_0}}{B^2}(\boldsymbol{\delta\xi}_{n\perp}^* \times \boldsymbol{B}_0)\cdot\boldsymbol{\delta B}_{n\perp} \\ - 2(\boldsymbol{\delta\xi}_{n\perp}\cdot\nabla p_0)(\boldsymbol{\delta\xi}_{n\perp}^*\cdot\boldsymbol{\kappa}_0)\}\,\mathcal{J}\mathrm{d}\psi\mathrm{d}\theta^*\mathrm{d}\phi\end{aligned} \tag{A.2}$$

$$\begin{aligned}\delta Y(\boldsymbol{\delta\xi}_n^*, \boldsymbol{\delta\xi}_{n'}) = -\frac{1}{2}\int \{[\boldsymbol{\delta\xi}_n^*\cdot(\boldsymbol{J}_N\times\boldsymbol{\delta B}_{n'} + \boldsymbol{\delta J}_{n'}\times\boldsymbol{B}_N)] \\ + [\nabla\times(\boldsymbol{\delta\xi}_n^*\times\boldsymbol{J}_0)]\cdot(\boldsymbol{\delta\xi}_{n'}\times\boldsymbol{B}_N) \\ - \boldsymbol{\delta J}_n^*\cdot(\boldsymbol{\delta\xi}_{n'}\times\boldsymbol{B}_N)\}\,\mathcal{J}\mathrm{d}\psi\mathrm{d}\theta^*\mathrm{d}\phi\end{aligned} \tag{A.3}$$

$$\begin{aligned}\delta S(\boldsymbol{\delta\xi}_n^*, \boldsymbol{\delta\xi}_{n'}) = -\frac{1}{2}\int \{(\boldsymbol{\delta\xi}_n^*\cdot\boldsymbol{n})[(\boldsymbol{\delta\xi}_{n'}\times\boldsymbol{B}_N)\cdot\boldsymbol{J}_0 - \boldsymbol{\delta B}_{n'\pm N}\cdot\boldsymbol{B}_0] \\ + \boldsymbol{\delta B}_n^*\cdot[\boldsymbol{B}_N(\boldsymbol{\delta\xi}_{n'}\cdot\boldsymbol{n}) - \boldsymbol{\delta\xi}_{n'}(\boldsymbol{B}_N\cdot\boldsymbol{n})] \\ + (\boldsymbol{\delta\xi}_n^*\cdot\boldsymbol{n})(\boldsymbol{\delta\xi}_{n'}\cdot\nabla p_N)\}\,\mathcal{J}\mathrm{d}\theta^*\mathrm{d}\phi\end{aligned} \tag{A.4}$$

Considering a solution that is obtained through superposition of axisymmetric solutions, i.e. the axisymmetric normal modes serve as trial functions, minimisation of their coupling coefficients, i.e. $\boldsymbol{c}^{\dagger}_{m,k}(\boldsymbol{\delta W} - \boldsymbol{\omega^2 \delta K})_{mn,kl}\boldsymbol{c}_{n,l}$=0, leads to a generalised eigenvalue problem to be numerically solved through LAPACK routines.

In order to efficiently and accurately compute the integral matrix elements, which involve terms based on integration and differentiation of highly oscillatory functions of the normal displacement functional $X_{n,l}$, the calculation is performed semi-analytically. Considering Fourier basis functions for the poloidal and toroidal dependence differential operators can be replaced from their eigenvalues and integral forms are simplified due to the orthogonality of the basis as appropriate sums. More specifically, the integral forms as written above can be generalised as an inner functional product, where $A_{mn,kl} = \int f^{\dagger}_{m,k} g_{n,l} \ \mathrm{d}\psi \delta_{mn,kl}$. Although, numerical differential is used for the radial coordinate ψ, based on polynomial differentiation. The choice of δW and δK as given above minimises the order of differentiation that takes place in the various terms. ELITE provides in terms of poloidal Fourier harmonics for each toroidal mode number the $X_{n,l}$, and a set of Fourier modes both in toroidal or poloidal direction occurs for each $X_{n,l}$, due to operations that take place within each energy term. In such a way, for each $c_{n,l}X_{n,l}$ a set of $c^{\dagger}_{m,k}A_{mn,kl}c_{n,l}$ elements can occur.

The quantities that need to be computed analytically, due to the fact that involve differentiation, are $\boldsymbol{\delta \xi}_{\perp n,l}$, $\boldsymbol{\delta B}_{n,l}$, $\boldsymbol{\delta B}_{n\pm N,l}$, $\boldsymbol{\delta J}_{n,l}$, and $\nabla \times (\boldsymbol{\xi}_{\perp \boldsymbol{n,l}} \times \boldsymbol{J}_0)$. The rest of the operations involve dot and cross products that are themselves analytic operations and can be exactly calculated by generalised routines considering a curvilinear coordinate system (ψ, θ, ϕ). For all vector quantities a contravariant representation, $A_i \nabla x^i$ is followed, since it simplifies operations.

- $(\boldsymbol{\delta \xi}_{\perp n,l})_{\psi} = g_{\psi\psi} X_{n,l}$
- $(\boldsymbol{\delta \xi}_{\perp n,l})_{\theta} = -\nu \dfrac{g^{\psi\psi}}{B^2} U_{n,l}$
- $(\boldsymbol{\delta \xi}_{\perp n,l})_{\phi} = \dfrac{g^{\psi\psi}}{B^2} U_{n,l}$
- $(\boldsymbol{\delta B}_{n,l})_{\psi} = \dfrac{g_{\psi\psi}}{\mathcal{J}} [\partial_{\theta} + \nu \partial_{\phi}] X_{n,l}$

- $(\boldsymbol{\delta B}_{n,l})_\theta = -\frac{g_{\theta\theta}}{\mathcal{J}}[\partial_\psi X_{n,l} + \partial_\phi U_{n,l}]$
- $(\boldsymbol{\delta B}_{n,l})_\phi = \frac{g_{\phi\phi}}{\mathcal{J}}[\partial_\theta U_{n,l} - \nu\partial_\psi X_{n,l} - \partial_\psi \nu X_{n,l}]$
- $\partial_\theta(\boldsymbol{\delta B}_{n,l})_\psi = \partial_\theta(\frac{g_{\psi\psi}}{\mathcal{J}})[\partial_\theta + \nu\partial_\phi]X_{n,l} + \frac{g_{\psi\psi}}{\mathcal{J}}[\partial_{\theta\theta} + \partial_\theta\nu\partial_\phi + \nu\partial_{\phi\theta}]X_{n,l}$
- $\partial_\psi(\boldsymbol{\delta B}_{n,l})_\theta = -\partial_\psi(\frac{g_{\theta\theta}}{\mathcal{J}})[\partial_\psi X_{n,l} + \partial_\phi U_{n,l}] - \frac{g_{\theta\theta}}{\mathcal{J}}[\partial_{\psi\psi} X_{n,l} + \partial_{\psi\phi} U_{n,l}]$
- $\partial_\psi(\boldsymbol{\delta B}_{n,l})_\phi = \partial_\psi(\frac{g_{\phi\phi}}{\mathcal{J}})[\partial_\theta U_{n,l} - \partial_\psi\nu X_{n,l} - \nu\partial_\psi X_{n,l}] + \frac{g_{\phi\phi}}{\mathcal{J}}[\partial_{\psi\theta} U_{n,l} - \partial_{\psi\psi}\nu X_{n,l} - \nu\partial_{\psi\psi} X_{n,l} - 2\partial_\psi\nu\partial_\psi^{} X_{n,l}]$
- $\partial_\theta(\boldsymbol{\delta B}_{n,l})_\phi = \partial_\theta(\frac{g_{\phi\phi}}{\mathcal{J}})[\partial_\theta U_{n,l} - \partial_\psi\nu X_{n,l} - \nu\partial_\psi X_{n,l}] + \frac{g_{\phi\phi}}{\mathcal{J}}[\partial_{\theta\theta} U_{n,l} - \partial_{\theta\psi}\nu X_{n,l} - \nu\partial_{\theta\psi} X_{n,l} - \partial_\theta\nu\partial_\psi X_{n,l} - \partial_\psi\nu\partial_\theta X_{n,l}]$
- $[\nabla \times (\boldsymbol{\xi_{\perp n,l}} \times \boldsymbol{J}_0)]_\psi = -\frac{g_{\psi\psi}}{\mathcal{J}}(\partial_\psi B_\phi \partial_\theta X_{n,l} + \nu(\frac{\partial_\psi p}{B_t^2} B_\phi + \partial_\psi B_\phi)\partial_\phi X_{n,l})$
- $[\nabla \times (\boldsymbol{\xi_{\perp n,l}} \times \boldsymbol{J}_0)]_\theta = \frac{g_{\theta\theta}}{\mathcal{J}}[\partial_{\psi\psi} B_\phi X_{n,l} + \partial_\psi B_\phi \partial_\psi X_{n,l} + (\frac{\partial_\psi p}{B^2} f + \partial_\psi B_\phi)\partial_\phi U_{n,l}]$
- $[\nabla \times (\boldsymbol{\xi_{\perp n,l}} \times \boldsymbol{J}_0)]_\phi = \frac{g_{\phi\phi}}{\mathcal{J}}\{\partial_\psi[\nu(\frac{\partial_\psi p}{B_t^2} B_\phi + \partial_\psi B_\phi)]X_{n,l} + \nu(\frac{\partial_\psi p}{B_t^2} B_\phi + \partial_\psi B_\phi)\partial_\psi X_{n,l} - \partial_\theta(\frac{\partial_\psi p}{B^2} B_\phi + \partial_\psi B_\phi)U_{n,l} + \nu(\frac{\partial_\psi p}{B^2} B_\phi + \partial_\psi B_\phi)\partial_\theta U_{n,l}\}$
- $\partial_\theta(\boldsymbol{\xi}_n \times \boldsymbol{B}_N)_\psi = -\partial_\theta(\frac{B_{N\theta} + \nu B_{N\phi}}{\mathcal{J}B^2})U_{n,l} - (\frac{B_{N\theta} + \nu B_{N\phi}}{\mathcal{J}B^2})\partial_\theta U_{n,l}$
- $\partial_\phi(\boldsymbol{\xi}_n \times \boldsymbol{B}_N)_\psi = -\frac{\partial_\phi[(B_{N\theta} + \nu B_{N\phi})U_{n,l}]}{\mathcal{J}B^2}$
- $\partial_\psi(\boldsymbol{\xi}_n \times \boldsymbol{B}_N)_\theta = -\partial_\psi(\frac{\nu}{B_\phi} B_{N\phi})X_{n,l} - (\frac{\nu}{B_\phi} B_{N\phi})\partial_\psi X_{n,l} + \partial_\psi(\frac{\nu g^{\psi\psi 2}}{B_\phi B^2} B_{N\psi})U_{n,l} + (\frac{\nu g^{\psi\psi 2}}{B_\phi B^2} B_{N\psi})\partial_\psi U_{n,l}$
- $\partial_\phi(\boldsymbol{\xi}_n \times \boldsymbol{B}_N)_\theta = -\partial_\phi[(\frac{\nu}{B_\phi} B_{N\phi})X_{n,l} - (\frac{\nu g^{\psi\psi 2}}{B_\phi B^2} B_{N\psi})U_{n,l}]$
- $\partial_\psi(\boldsymbol{\xi}_n \times \boldsymbol{B}_N)_\phi = \partial_\psi[\nu(\frac{\partial_\psi p}{B_t^2} B_\phi + \partial_\psi B_\phi)]X_{n,l} + \nu(\frac{\partial_\psi p}{B_t^2} B_\phi + \partial_\psi B_\phi)\partial_\psi X_{n,l} + \partial_\psi[(\frac{\partial_\psi p}{B^2} B_\phi + \partial_\psi B_\phi)]U_{n,l} + (\frac{\partial_\psi p}{B^2} B_\phi + \partial_\psi B_\phi)\partial_\psi U_{n,l}$
- $\partial_\theta(\boldsymbol{\xi}_n \times \boldsymbol{B}_N)_\phi = B_\phi\partial_\theta(\frac{g_{\psi\psi}}{\nu} B_{\theta N})X_{n,l} + \frac{B_\phi g_{\psi\psi}}{\nu} B_{\theta N}\partial_\theta X_{n,l} + B_\phi\partial_\theta(\frac{g^{\psi\psi}}{B^2} B_{N\psi})U_{n,l} + \frac{B_\phi g^{\psi\psi}}{B^2} B_{N\psi}\partial_\theta U_{n,l}$

- $\nabla \cdot \boldsymbol{\xi}_{\perp n,l} = (\partial_\psi \ln \mathcal{J} + \partial_\psi) X_{n,l} - (2\frac{|\nabla\psi|}{B}\kappa_s + \frac{B_t^2}{\nu B^2}\partial_\theta - \frac{B_p^2}{B^2}\partial_\phi) U_{n,l}$

The derivatives of the displacement functionals $X_{n,l}$ and $U_{n,l}$ are the remaining quantities to be computed analytically and are given in the list below.

- $\partial_\psi X_{n,l} = (\mathrm{d}_\psi - il\partial_\psi\theta^*)X_{n,l}$
- $\partial_\theta X_{n,l} = -i\frac{\nu}{q} l X_{n,l}$
- $\partial_{\psi\psi} X_{n,l} = [\mathrm{d}_{\psi\psi} - il\partial_{\psi\psi}\theta^* - (l\partial_\psi\theta^*)^2 - i2l\partial_\psi\theta^*]X_{n,l}$
- $\partial_{\theta\psi} X_{n,l} = -il[\frac{\nu}{q}\partial_\psi + \partial_\psi(\frac{\nu}{q})]X_{n,l}$
- $\partial_{\theta\theta} X_{n,l} = -i\frac{l}{q}(\partial_\theta\nu + \nu\partial_\theta)X_{n,l}$
- $\partial_{\theta\theta\psi} X_{n,l} = -il[\partial_{\theta\psi}(\frac{\nu}{q}) + \partial_\psi(\frac{\nu}{q})\partial_\theta + \partial_\theta(\frac{\nu}{q})\partial_\psi + (\frac{\nu}{q})\partial_{\theta\psi}]X_{n,l}$
- $\partial_{\theta\psi\psi} X_{n,l} = -il[\partial_{\theta\psi}(\frac{\nu}{q}) + 2\partial_\psi(\frac{\nu}{q})\partial_\psi + (\frac{\nu}{q})\partial_{\psi\psi}]X_{n,l}$
- $U_{n,l} = \frac{i}{n}(\partial_\psi + \frac{\partial_\psi p}{B^2})X_{n,l} + W_{n,l}$
- $\partial_\psi U_{n,l} = \frac{i}{n}[\partial_{\psi\psi} + \frac{\partial_\psi p}{B^2}\partial_\psi + \partial_\psi(\frac{\partial_\psi p}{B^2})]X_{n,l} + \frac{i}{n}\partial_\psi W_{n,l}$
- $\partial_\theta U_{n,l} = \frac{i}{n}[\partial_{\theta\psi} + \frac{\partial_\psi p}{B^2}\partial_\theta + \partial_\theta(\frac{\partial_\psi p}{B^2})]X_{n,l} + \frac{i}{n}\partial_\theta W_{n,l}$
- $\partial_{\theta\psi} U_{n,l} = \frac{i}{n}[\partial_{\theta\psi\psi} + (\frac{\partial_\psi p}{B^2})\partial_{\theta\psi} + \partial_\theta(\frac{\partial_\psi p}{B^2})\partial_\psi + \partial_\psi(\frac{\partial_\psi p}{B^2})\partial_\theta + \partial_{\theta\psi}(\frac{\partial_\psi p}{B^2})]X_{n,l} + \frac{i}{n}\partial_{\theta\psi} W_{n,l}$
- $\partial_{\theta\theta} U_{n,l} = \frac{i}{n}[\partial_{\theta\theta\psi} + (\frac{\partial_\psi p}{B^2})\partial_{\theta\theta} + 2\partial_\theta(\frac{\partial_\psi p}{B^2})\partial_\theta + \partial_{\theta\theta}(\frac{\partial_\psi p}{B^2})]X_{n,l} + \frac{i}{n}\partial_{\theta\theta} W_{n,l}$

Finally, the functional $W_{n,l}$ has the same functional form as $X_{n,l}$, as such differential operations on $W_{n,l}$ result similar functionals as $X_{n,l}$. Due to the choice of an axisymmetric coordinate system, the differential operator $\partial_\phi = in$ when acting on any perturbed quantity and $\partial_\phi = 0$ when acting on any equilibrium quantity. The only difference occurs when terms include the plasma response together with the perturbed quantity, where $\partial_\phi = i(n \pm N)$.

Appendix B

Appendix: 3D Stability Framework

B.1 Code Structure

The numerical framework is implemented in a Fortran90 code and is split in various modules, allowing a tractable structure and facilitating future development. A summary of the various modules is is given below.

main.f90

In this module the main operations of the work flow are called, linking in such a way the input parameters, the grid generation, the MP vacuum field, the elite run for the plasma response, the reconstruction of the equilibrium, the reconstruction of the axisymmetric eigenmodes and the 3D plasma stability, either via the perturbative method or the variational method. All tasks can run independently and according to flags that are specified in the initialisation input file.

initiate.f90

This module reads the initialisation input file and defines global variables for other modules to use. In the input file the user can specify various options, which parts of the general code to be used and specifies information regarding folder and file paths, the grid resolution, the MP coil configuration, symmetric

or asymmetric plasma, regular or low n ELITE version, axisymmetric toroidal modes to be used, variational or perturbative method, etc. The list of the important variables defined is given below:

1. Grid:
    - Radial Res: nr
    - Poloidal Res: nt
    - Increase Poloidal Res: mlt
2. Modes:
    - Minimum poloidal mode for response: $mmin$
    - Maximum poloidal mode for response: $mmax$
    - Minimum toroidal mode for stability: ni
    - Maximum poloidal mode for stability: nf
3. Functionality:
    - Use Low n ELITE: $lown$
    - Asymmetric Plasma: $asym$
    - Spare Grid Initialisation: grd
    - Fine Grid Initialisation: $axis$
    - Boundary Condition: $rmpbc$
    - Equilibrium Response: sol
    - Stability: $stab$
    - Axisymmetric Stability Response: $resp$
    - Variational Poloidal Coupling: pl
    - Axisymmetric Stability: pl_axis
    - Non-Axisymmetric Stability: pl_na
4. Stability:
    - Scale External Field: b_fact
    - Variational Multi-toroidal Coupling: cpl_ord
    - Use δW_0, δK_0 from ELITE: $elite$

numerical.f90

This module contains various numerical routines that are used within the code, regarding interpolation, integration, differentiation, matrix inversion, eigenvalue solvers, Fourier transforms, etc.

grid.f90

This module is responsible for generating the computational grid and equilibrium parameters as resulted from ELITE, and calculates other equilibrium parameters that are needed further on.

create_input_nc.f90

This module interpolates the sparse grid of the equilibrium parameters into a fine grid that the plasma response and stability are computed. In addition, it gathers information from ELITE output data regarding the linear plasma response and calculates information related to the plasma displacement.

equilibrium.f90

This module calculates the linear plasma response in terms of the plasma displacement, magnetic field, current density and pressure, for a given normal displacement that is provided from ELITE.

plasma_response.f90

This module calculates the plasma displacement, magnetic field, current density and pressure, for a given axisymmetric toroidal normal mode considering the axisymmetric and non-axisymmetric plasma equilibrium. This information is used in the 3D stability calculation.

matrix_elements.f90

This module calculates the axisymmetric stability, i.e. potential and kinetic energy, and the non-axisymmetric matrix elements. It computes the 3D growth rate and mode structure according to perturbation theory (also valid for a variational approach when no poloidal coupling is retained).

matrix_elements_poloidal.f90

This module calculates the axisymmetric potential and kinetic energy matrices and the non-axisymmetric matrices used in the variational approach. It computes the 3D growth rate and mode structure according to variational theory retaining the poloidal coupling.

B.2 Vacuum Field Code

The calculation of the magnetic field produced from a certain configuration of MP coils is numerically computed in this Fortran90 code. The code is divided in several modules that independently create the various required information. The main modules are:

1. Prameter initialisation
2. Grid points in (x, y, z) or (r, z, ϕ)
3. Coil configuration in (x, y, z)
4. Calculation of $\mathbf{B}_{MP}(x, y, z)$
5. Coordinate Transform:
    - Cylindrical Geometry (r, z, ϕ)
    - Orthogonal Toroidal Geometry (ψ, θ, ϕ)
    - Straight-Field Line Toroidal Geometry (ψ, θ^*, ϕ)

All data are saved in NetCDF format that ensures computational efficiency when a large number of 3D data is produced. The outputs are saved in different

files and contain the grid geometry, the coil geometry, the coil current, the magnetic field in cartesian (x, y, z), cylindrical (R, Z, ϕ) and toroidal (ψ, θ, ϕ) coordinates. The visualisation of the various information is performed using VisIt. In order for this program to read and create the required geometry, a different file format is needed. Python routines have been developed that read the NetCDF output and transform it to VTK format.

Code Structure

elite_rmp_drive.f90

The code is separated in different modules to facilitate the conceptual understanding of the inner working as well as the easier modification of the various parts. This part of the program is responsible for the connection of the various modules. Initially, the module reads the required input parameters. Then, the computational grid over which the magnetic field is map is created and the MP coil configuration. Finally, the magnetic field or magnetic potential is calculated and mapped to a straight field line poloidal angle and outputs the required boundary condition.

initiate.f90

This module is responsible for the definition of all the information used by the various modules. The variables are defined as global parameters such that all other modules can intrinsically get access to those values. Although, this means that every time the parameters have to change the code has to be recompiled. The list of the variables defined is given below:

- Grid resolution: $(nr, nphi, ntheta)$
- Lower wire: r_0, z_0
- Upper wire: r_1, z_1
- Coil set points: res
- Wire resolution: nc

- Number of coils: num
- Coil set parity: $parity$
- RMP toroidal mode: n
- Coil current amplitude: I
- Elongation: κ (optional)
- Triangularity: δ (optional)
- Major radius of tokamak plasma: R_0 (optional)
- Minor radius of tokamak plasma: a_0 (optional)

grid.f90

This module creates the computational mesh used for the calculation of the resultant MP field. It is optional to input a grid file containing the (r, z) cross-section or to create toroidal axisymmetric configurations. The module creates two coordinate systems, one cartesian (x, y, z) and one cylindrical (r, z, ϕ) and the calculation of the mesh positions are based on a toroidal coordinate system (r, θ, ϕ) assuming a major R and minor α radius of the tokamak. In addition, it accounts for plasma shaping effects in terms of elongation κ and triangularity angle $\theta_\delta = \theta + \sin^{-1}(\delta)\sin(\theta)$, where δ is the triangularity. The parametric equations linking (x, y, z) or (r, z, ϕ) to (r, θ, ϕ) are displayed in Eqn.(B.1) and Eqn.(B.2). An illustration of MAST and ITER like meshes are depicted in Fig.B.1 and Fig.B.2 respectively.

Cartesian Grid:

$$x = [R + \alpha\cos(\theta_\delta)]\cos(\phi) \tag{B.1a}$$

$$y = [R + \alpha\cos(\theta_\delta)]\sin(\phi) \tag{B.1b}$$

$$z = \kappa\alpha\sin(\theta) \tag{B.1c}$$

Cylindrical Grid:

$$r = R + \alpha\cos(\theta_\delta) \tag{B.2a}$$

$$z = \kappa\alpha\sin(\theta) \tag{B.2b}$$

$$\phi = \phi \tag{B.2c}$$

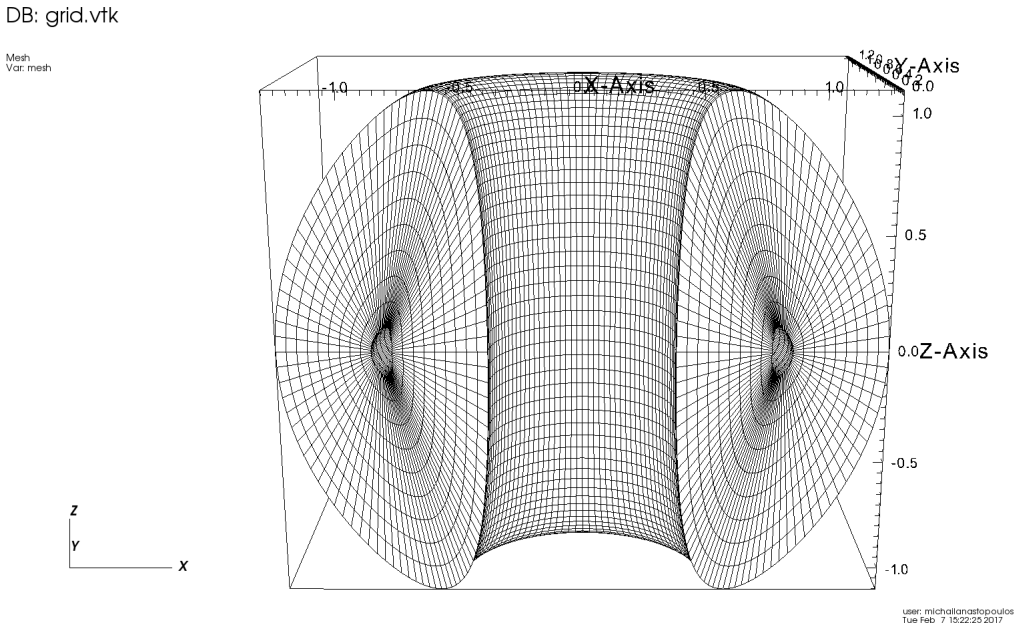

FIGURE B.1: MAST like geometry for a major radius $R = 0.85$m, minor radius $\alpha = 0.45$m, elongation $\kappa = 2.45$ and triangularity $\delta = 0.5$.

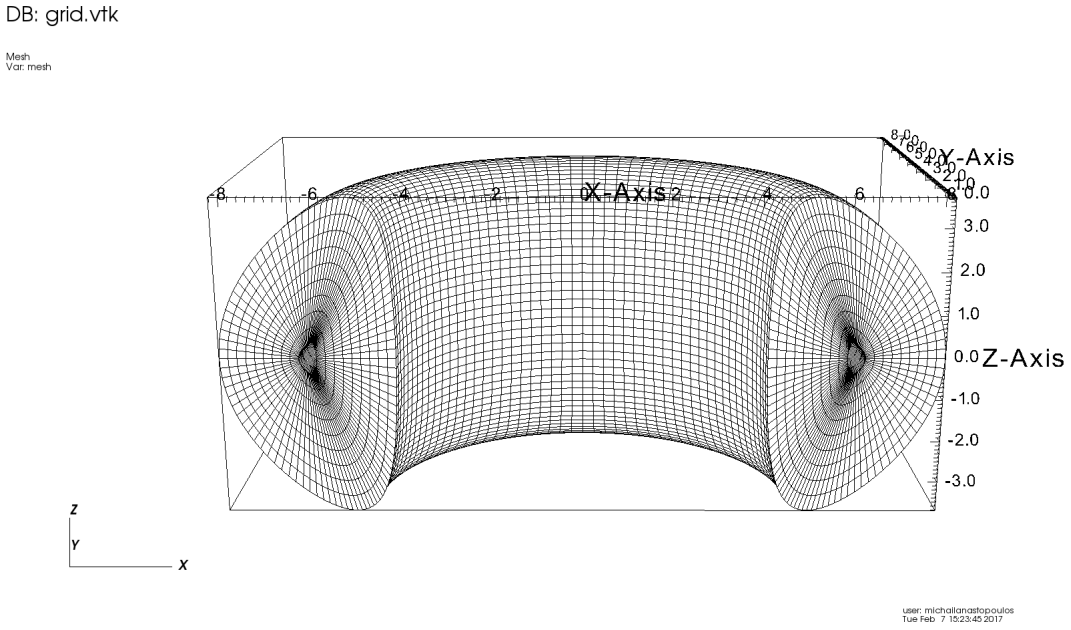

FIGURE B.2: ITER like geometry for a major radius $R = 6.2$m, minor radius $\alpha = 2.0$m, elongation $\kappa = 1.85$ and triangularity $\delta = 0.49$.

rmp_coils.f90

In this module the MP coil configuration is created in cartesian coordinates. The MP coils are usually rectangular boxes that are placed up and down the plasma mid-plane and Fig.[B.3] illustrates the coil configuration. The module requires as inputs the location of the corners (r_0, z_0) and (r_1, z_1) of the a single coil as depicted in Fig.[B.3].

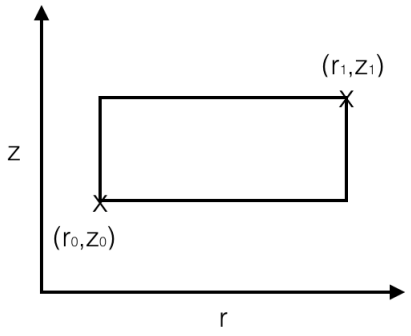

FIGURE B.3: Schematic of (r_0, z_0) and (r_1, z_1) input coil locations.

The creation of the whole set of MPs comes in two main parts. First, a single coil is centred at $\phi = 0$ and by knowing the total number of coils, the angular distance of the next coil is evaluated such that by a rotational transform,

$$R_z = \begin{pmatrix} \cos(\phi) & -\sin(\phi) & 0 \\ \sin(\phi) & \cos(\phi) & 0 \\ 0 & 0 & 1 \end{pmatrix} \tag{B.3}$$

around the z-axis can place the next coil according to the original one. In the end the module returns the position of the coils and the current vector depending on the input parameters as defined in **initiate.f90**.

An additional detail of this module is the variation of the distance between individual coils which is set by an angular distance $d\phi$. The calculation of the current vector $\boldsymbol{I}$ is based on a unit vector which is calculated from the location of the coil corners and its amplitude is defined by a constant factor. An example of MAST for an even $n = 3$ coil configuration is illustrated in Fig.[B.4].

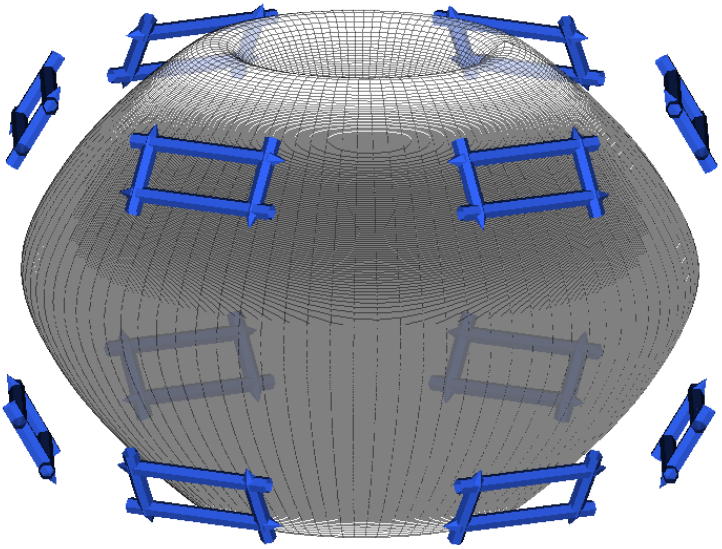

FIGURE B.4: MAST MP coils for an even $n = 3$ configuration.

magnetic_field.f90

The calculation of the magnetic field is based on the Biot-Savart Law,

$$\boldsymbol{B}_{MP}(\boldsymbol{r}) = \frac{\mu_0 I}{4\pi} \int_c \frac{\boldsymbol{dl} \times \boldsymbol{r}}{r^3} \tag{B.4}$$

The magnetic field depends on the distance vector $\boldsymbol{r}$ between the current-coil increment $\boldsymbol{dl}$ at $\boldsymbol{r}_{coil}$ and the grid location $\boldsymbol{r}_{grid}$, since $\boldsymbol{r} = \boldsymbol{r}_{grid} - \boldsymbol{r}_{coil}$. All the variables are provided to this module from the previous modules. The calculation of the integral is performed by summing over the contribution of each coil elements.

$$\boldsymbol{B}_{MP}(\boldsymbol{r}_j) \approx \frac{\mu_0 I}{4\pi} \sum_i \frac{\boldsymbol{dl}_i \times (\boldsymbol{r}_j - \boldsymbol{r}_i)}{(r_j - r_i)^3} \tag{B.5}$$

elite_bc.f90

This module is responsible for performing the Fourier analysis of the MP field in straight field line poloidal harmonics at the plasma surface, leading to the fixed boundary condition inserted in ELITE. The mapping of the straight field

angle to the poloidal angle is given by,

$$d\theta^* = \frac{f h_\theta}{q R^2 B_p} d\theta \tag{B.6}$$

where $h_\theta = \sqrt{(\partial_\theta R)^2 + (\partial_\theta Z)^2}$. The information regarding the equilibrium quantities can be obtained from an input grid file that is read in **grid.f90**.

Bibliography

[1] IEA. Key world energy statistics. 2017. URL http://www.iea.org/publications/freepublications/publication/keyworld2014.pdf.

[2] Malte Meinshausen, Nicolai Meinshausen, William Hare, Sarah C. B. Raper, Katja Frieler, Reto Knutti, David J. Frame, and Myles R. Allen. Greenhouse-gas emission targets for limiting global warming to 2 °c. *Nature*, 458:1158 EP –, 04 2009. URL https://doi.org/10.1038/nature08017.

[3] Shahriar Shafiee and Erkan Topal. When will fossil fuel reserves be diminished? *Energy Policy*, 37(1):181 – 189, 2009. ISSN 0301-4215. doi: https://doi.org/10.1016/j.enpol.2008.08.016. URL http://www.sciencedirect.com/science/article/pii/S0301421508004126.

[4] J. Rich J.L. Basdevant and M. Spiro. Fundamentals in nuclear physics, from nuclear structure to cosmology. *Springer*, 2005. URL http://www.springer.com/physics/particle+and+nuclear+physics/book/978-0-387-01672-6.

[5] J. Wesson. Tokomaks. *Oxford University Press*, 2011. URL http://ukcatalogue.oup.com/product/9780199592234.do.

[6] J. D. Lawson. Some criteria for a power producing thermonuclear reactor. *Proceedings of the Physical Society. Section B*, 70(1):6–10, jan 1957. doi: 10.1088/0370-1301/70/1/303. URL https://doi.org/10.1088%2F0370-1301%2F70%2F1%2F303.

[7] JET Team (prepared by M.L Watkins). Physics of high performance JET plasmas in DT. *Nuclear Fusion*, 39(9Y):1227–1244, sep 1999. doi:

10.1088/0029-5515/39/9y/302. URL https://doi.org/10.1088%2F0029-5515%2F39%2F9y%2F302.

[8] EUROfusion. 50 years of Lawson Criteria. 2005. URL https://www.euro-fusion.org/news/detail/detail/News/50-years-of-lawson-criteria/.

[9] F. Wagner, G. Becker, K. Behringer, D. Campbell, A. Eberhagen, W. Engelhardt, G. Fussmann, O. Gehre, J. Gernhardt, G. v. Gierke, G. Haas, M. Huang, F. Karger, M. Keilhacker, O. Klüber, M. Kornherr, K. Lackner, G. Lisitano, G. G. Lister, H. M. Mayer, D. Meisel, E. R. Müller, H. Murmann, H. Niedermeyer, W. Poschenrieder, H. Rapp, H. Röhr, F. Schneider, G. Siller, E. Speth, A. Stäbler, K. H. Steuer, G. Venus, O. Vollmer, and Z. Yü. Regime of improved confinement and high beta in neutral-beam-heated divertor discharges of the asdex tokamak. *Phys. Rev. Lett.*, 49:1408–1412, Nov 1982. doi: 10.1103/PhysRevLett.49.1408. URL http://link.aps.org/doi/10.1103/PhysRevLett.49.1408.

[10] F Wagner. A quarter-century of h-mode studies. *Plasma Physics and Controlled Fusion*, 49(12B):B1–B33, nov 2007. doi: 10.1088/0741-3335/49/12b/s01. URL https://doi.org/10.1088%2F0741-3335%2F49%2F12b%2Fs01.

[11] G R Tynan, I Cziegler, P H Diamond, M Malkov, A Hubbard, J W Hughes, J L Terry, and J H Irby. Recent progress towards a physics-based understanding of the h-mode transition. *Plasma Physics and Controlled Fusion*, 58(4):044003, jan 2016. doi: 10.1088/0741-3335/58/4/044003. URL https://doi.org/10.1088%2F0741-3335%2F58%2F4%2F044003.

[12] P. H. Diamond, Y.-M. Liang, B. A. Carreras, and P. W. Terry. Self-regulating shear flow turbulence: A paradigm for the l to h transition. *Phys. Rev. Lett.*, 72:2565–2568, Apr 1994. doi: 10.1103/PhysRevLett.72.2565. URL https://link.aps.org/doi/10.1103/PhysRevLett.72.2565.

[13] J Schirmer, G.D Conway, H Zohm, W Suttrop, and the ASDEX Upgrade Team. The radial electric field and its associated shear in the ASDEX upgrade tokamak. *Nuclear Fusion*, 46(9):S780–S791, aug 2006.

doi: 10.1088/0029-5515/46/9/s13. URL https://doi.org/10.1088%2F0029-5515%2F46%2F9%2Fs13.

[14] ITER Physics Basis Editors, ITER Physics Expert Group Chairs an Co-Chairs, ITER Joint Central Team, and Physics Unit. Chapter 1: Overview and summary. *Nuclear Fusion*, 39(12):2137–2174, dec 1999. doi: 10.1088/0029-5515/39/12/301. URL https://doi.org/10.1088%2F0029-5515%2F39%2F12%2F301.

[15] S. Shibaev. Software for fast cameras and image handling on mast. *Fusion Engineering and Design*, 83(4):667 – 671, 2008. ISSN 0920-3796. doi: https://doi.org/10.1016/j.fusengdes.2008.02.007. URL http://www.sciencedirect.com/science/article/pii/S092037960800032X.

[16] A. Loarte, G. Saibene, R. Sartori, T. Eich, A. Kallenbach, W. Suttrop, M. Kempenaars, M. Beurskens, M. de Baar, J. Lönnroth, P. J. Lomas, G. Matthews, W. Fundamenski, V. Parail, M. Becoulet, P. Monier-Garbet, E. de la Luna, B. Gonçalves, C. Silva, Y. Corre, and Contributors to the EFDA-JET Workprogramme. Characterization of pedestal parameters and edge localized mode energy losses in the joint european torus and predictions for the international thermonuclear experimental reactor. *Physics of Plasmas*, 11(5):2668–2678, 2004. doi: 10.1063/1.1707025. URL https://doi.org/10.1063/1.1707025.

[17] H Zohm. Edge localized modes (ELMs). *Plasma Physics and Controlled Fusion*, 38(2):105–128, feb 1996. doi: 10.1088/0741-3335/38/2/001. URL https://doi.org/10.1088%2F0741-3335%2F38%2F2%2F001.

[18] J W Connor. Edge-localized modes - physics and theory. *Plasma Physics and Controlled Fusion*, 40(5):531–542, may 1998. doi: 10.1088/0741-3335/40/5/002. URL https://doi.org/10.1088%2F0741-3335%2F40%2F5%2F002.

[19] W Suttrop. The physics of large and small edge localized modes. *Plasma Physics and Controlled Fusion*, 42(5A):A1–A14, may 2000. doi: 10.1088/0741-3335/42/5a/301. URL https://doi.org/10.1088%2F0741-3335%2F42%2F5a%2F301.

[20] C.P Perez, H.R Koslowski, G.T.A Huysmans, T.C Hender, P Smeulders, B Alper, E. de la Luna, R.J Hastie, L Meneses, M.F.F Nave, V Parail, M Zerbini, and JET-EFDA Contributors. Type-i ELM precursor modes in JET. *Nuclear Fusion*, 44(5):609–623, apr 2004. doi: 10.1088/0029-5515/44/5/005. URL https://doi.org/10.1088%2F0029-5515%2F44%2F5%2F005.

[21] A Loarte, M Becoulet, G Saibene, R Sartori, D J Campbell, T Eich, A Herrmann, M Laux, W Suttrop, B Alper, P J Lomas, G Matthews, S Jachmich, J Ongena, P Innocente, and EFDA-JET Workprogramme Collaborators. Characteristics and scaling of energy and particle losses during type i ELMs in JET h-modes. *Plasma Physics and Controlled Fusion*, 44(9):1815–1844, aug 2002. doi: 10.1088/0741-3335/44/9/303. URL https://doi.org/10.1088%2F0741-3335%2F44%2F9%2F303.

[22] T. Eich, B. Sieglin, A.J. Thornton, M. Faitsch, A. Kirk, A. Herrmann, and W. Suttrop. Elm divertor peak energy fluence scaling to iter with data from jet, mast and asdex upgrade. *Nuclear Materials and Energy*, 12:84 – 90, 2017. ISSN 2352-1791. doi: https://doi.org/10.1016/j.nme.2017.04.014. URL http://www.sciencedirect.com/science/article/pii/S2352179116302927. Proceedings of the 22nd International Conference on Plasma Surface Interactions 2016, 22nd PSI.

[23] R.A. Pitts, S. Carpentier, F. Escourbiac, T. Hirai, V. Komarov, S. Lisgo, A.S. Kukushkin, A. Loarte, M. Merola, A. Sashala Naik, R. Mitteau, M. Sugihara, B. Bazylev, and P.C. Stangeby. A full tungsten divertor for iter: Physics issues and design status. *Journal of Nuclear Materials*, 438:S48 – S56, 2013. ISSN 0022-3115. doi: https://doi.org/10.1016/j.jnucmat.2013.01.008. URL http://www.sciencedirect.com/science/article/pii/S0022311513000160. Proceedings of the 20th International Conference on Plasma-Surface Interactions in Controlled Fusion Devices.

[24] J Stober, M Maraschek, G.D Conway, O Gruber, A Herrmann, A.C.C Sips, W Treutterer, H Zohm, and ASDEX Upgrade Team. Type II ELMy h modes on ASDEX upgrade with good confinement at high density. *Nuclear Fusion*, 41(9):1123–1134, sep 2001. doi: 10.1088/0029-5515/41/9/301. URL https://doi.org/10.1088%2F0029-5515%2F41%2F9%2F301.

[25] K H Burrell, M E Austin, D P Brennan, J C DeBoo, E J Doyle, P Gohil, C M Greenfield, R J Groebner, L L Lao, T C Luce, M A Makowski, G R McKee, R A Moyer, T H Osborne, M Porkolab, T L Rhodes, J C Rost, M J Schaffer, B W Stallard, E J Strait, M R Wade, G Wang, J G Watkins, W P West, and L Zeng. Quiescent h-mode plasmas in the DIII-d tokamak. *Plasma Physics and Controlled Fusion*, 44(5A):A253–A263, apr 2002. doi: 10.1088/0741-3335/44/5a/325. URL https://doi.org/10.1088%2F0741-3335%2F44%2F5a%2F325.

[26] W Suttrop, V Hynönen, T Kurki-Suonio, P.T Lang, M Maraschek, R Neu, A Stäbler, G.D Conway, S Hacquin, M Kempenaars, P.J Lomas, M.F.F Nave, R.A Pitts, K.-D Zastrow, the ASDEX Upgrade team, and contributors to the JET-EFDA workprogramme. Studies of the 'quiescent h-mode' regime in ASDEX upgrade and JET. *Nuclear Fusion*, 45(7): 721–730, jul 2005. doi: 10.1088/0029-5515/45/7/021. URL https://doi.org/10.1088%2F0029-5515%2F45%2F7%2F021.

[27] Y Sakamoto, H Shirai, T Fujita, S Ide, T Takizuka, N Oyama, and Y Kamada. Impact of toroidal rotation on ELM behaviour in the h-mode on JT-60u. *Plasma Physics and Controlled Fusion*, 46(5A):A299–A304, apr 2004. doi: 10.1088/0741-3335/46/5a/033. URL https://doi.org/10.1088%2F0741-3335%2F46%2F5a%2F033.

[28] K.H. Burrell, T.H. Osborne, P.B. Snyder, W.P. West, M.E. Fenstermacher, R.J. Groebner, P. Gohil, A.W. Leonard, and W.M. Solomon. Edge pedestal control in quiescent h-mode discharges in DIII-d using co-plus counter-neutral beam injection. *Nuclear Fusion*, 49(8):085024, jul 2009. doi: 10.1088/0029-5515/49/8/085024. URL https://doi.org/10.1088%2F0029-5515%2F49%2F8%2F085024.

[29] M. Greenwald, R. Boivin, P. Bonoli, R. Budny, C. Fiore, J. Goetz, R. Granetz, A. Hubbard, I. Hutchinson, J. Irby, B. LaBombard, Y. Lin, B. Lipschultz, E. Marmar, A. Mazurenko, D. Mossessian, T. Sunn Pedersen, C. S. Pitcher, M. Porkolab, J. Rice, W. Rowan, J. Snipes, G. Schilling, Y. Takase, J. Terry, S. Wolfe, J. Weaver, B. Welch, and S. Wukitch. Characterization of enhanced D_α high-confinement modes in alcator c-mod. *Physics of Plasmas*, 6(5):1943–1949, 1999. doi: 10.1063/1.873451. URL https://doi.org/10.1063/1.873451.

[30] D.G. Whyte, A.E. Hubbard, J.W. Hughes, B. Lipschultz, J.E. Rice, E.S. Marmar, M. Greenwald, I. Cziegler, A. Dominguez, T. Golfinopoulos, N. Howard, L. Lin, R.M. McDermott, M. Porkolab, M.L. Reinke, J. Terry, N. Tsujii, S. Wolfe, S. Wukitch, and Y. Lin and. I-mode: an h-mode energy confinement regime with l-mode particle transport in alcator c-mod. *Nuclear Fusion*, 50(10):105005, aug 2010. doi: 10.1088/0029-5515/50/10/105005. URL https://doi.org/10.1088%2F0029-5515%2F50%2F10%2F105005.

[31] H. ALFVÉN. Existence of electromagnetic-hydrodynamic waves. *Nature*, 150(3805):405–406, 1942. doi: 10.1038/150405d0. URL https://doi.org/10.1038/150405d0.

[32] J. W. Connor, R. J. Hastie, H. R. Wilson, and R. L. Miller. Magnetohydrodynamic stability of tokamak edge plasmas. *Physics of Plasmas*, 5(7):2687–2700, 1998. doi: 10.1063/1.872956. URL https://doi.org/10.1063/1.872956.

[33] P. B. Snyder, H. R. Wilson, J. R. Ferron, L. L. Lao, A. W. Leonard, T. H. Osborne, A. D. Turnbull, D. Mossessian, M. Murakami, and X. Q. Xu. Edge localized modes and the pedestal: A model based on coupled peeling–ballooning modes. *Physics of Plasmas*, 9(5):2037–2043, 2002. doi: 10.1063/1.1449463. URL https://doi.org/10.1063/1.1449463.

[34] A Loarte, B Lipschultz, A.S Kukushkin, G.F Matthews, P.C Stangeby, N Asakura, G.F Counsell, G Federici, A Kallenbach, K Krieger, A Mahdavi, V Philipps, D Reiter, J Roth, J Strachan, D Whyte, R Doerner, T Eich, W Fundamenski, A Herrmann, M Fenstermacher, P Ghendrih, M Groth, A Kirschner, S Konoshima, B LaBombard, P Lang, A.W Leonard, P Monier-Garbet, R Neu, H Pacher, B Pegourie, R.A Pitts, S Takamura, J Terry, E Tsitrone, the ITPA Scrape-off Layer, and Diver Group. Chapter 4: Power and particle control. *Nuclear Fusion*, 47(6):S203–S263, jun 2007. doi: 10.1088/0029-5515/47/6/s04. URL https://doi.org/10.1088%2F0029-5515%2F47%2F6%2Fs04.

[35] M.N.A. Beurskens, G. Arnoux, A.S. Brezinsek, C.D. Challis, P.C. de Vries, C. Giroud, A. Huber, S. Jachmich, K. McCormick, R.A. Pitts, F.G. Rimini, A. Alfier, E. de la Luna, W. Fundamenski, S. Gerasimov, E. Giovannozzi, E. Joffrin, M. Kempenaars, X. Litaudon, T. Loarer, P. Lomas, J. Mailloux,

R. Pasqualotto, V. Pericoli-Ridolfini, R. Pugno, E. Rachlew, S. Saarelma, E. Solano, M. Walsh, L. Zabeo, and K.-D. Zastrow and. Pedestal and ELM response to impurity seeding in JET advanced scenario plasmas. *Nuclear Fusion*, 48(9):095004, aug 2008. doi: 10.1088/0029-5515/48/9/095004. URL https://doi.org/10.1088%2F0029-5515%2F48%2F9%2F095004.

[36] C. Giroud, G.P. Maddison, S. Jachmich, F. Rimini, M.N.A. Beurskens, I. Balboa, S. Brezinsek, R. Coelho, J.W. Coenen, L. Frassinetti, E. Joffrin, M. Oberkofler, M. Lehnen, Y. Liu, S. Marsen, K. McCormick, A. Meigs, R. Neu, B. Sieglin, G. van Rooij, G. Arnoux, P. Belo, M. Brix, M. Clever, I. Coffey, S. Devaux, D. Douai, T. Eich, J. Flanagan, S. Grünhagen, A. Huber, M. Kempenaars, U. Kruezi, K. Lawson, P. Lomas, C. Lowry, I. Nunes, A. Sirinnelli, A.C.C. Sips, M. Stamp, and S. Wiesen and. Impact of nitrogen seeding on confinement and power load control of a high-triangularity JET ELMy h-mode plasma with a metal wall. *Nuclear Fusion*, 53(11):113025, sep 2013. doi: 10.1088/0029-5515/53/11/113025. URL https://doi.org/10.1088%2F0029-5515%2F53%2F11%2F113025.

[37] A W Degeling, Y R Martin, J B Lister, L Villard, V N Dokouka, V E Lukash, and R R Khayrutdinov. Magnetic triggering of ELMs in TCV. *Plasma Physics and Controlled Fusion*, 45(9):1637–1655, aug 2003. doi: 10.1088/0741-3335/45/9/306. URL https://doi.org/10.1088%2F0741-3335%2F45%2F9%2F306.

[38] E. de la Luna, I.T. Chapman, F. Rimini, P.J. Lomas, G. Saibene, F. Koechl, R. Sartori, S. Saarelma, R. Albanese, J. Flanagan, F. Maviglia, V. Parail, A.C.C. Sips, and E.R. Solano and. Understanding the physics of ELM pacing via vertical kicks in JET in view of ITER. *Nuclear Fusion*, 56(2):026001, dec 2015. doi: 10.1088/0029-5515/56/2/026001. URL https://doi.org/10.1088%2F0029-5515%2F56%2F2%2F026001.

[39] S H Kim, M M Cavinato, V Dokuka, A A Ivanov, R R Khayrutdinov, P T Lang, J B Lister, V E Lukash, Y R Martin, S Yu Medvedev, and L Villard. Comparing magnetic triggering of ELMs in TCV and ASDEX upgrade. *Plasma Physics and Controlled Fusion*, 51(5):055021, apr 2009. doi: 10.1088/0741-3335/51/5/055021. URL https://doi.org/10.1088%2F0741-3335%2F51%2F5%2F055021.

[40] P.T. Lang, K. Lackner, M. Maraschek, B. Alper, E. Belonohy, K. Gál, J. Hobirk, A. Kallenbach, S. Kálvin, G. Kocsis, C.P. Perez von Thun, W. Suttrop, T. Szepesi, R. Wenninger, H. Zohm, and and. Investigation of pellet-triggered MHD events in ASDEX upgrade and JET. *Nuclear Fusion*, 48(9):095007, aug 2008. doi: 10.1088/0029-5515/48/9/095007. URL https://doi.org/10.1088%2F0029-5515%2F48%2F9%2F095007.

[41] L.R. Baylor, S.K. Combs, C.R. Foust, T.C. Jernigan, S.J. Meitner, P.B. Parks, J.B. Caughman, D.T. Fehling, S. Maruyama, A.L. Qualls, D.A. Rasmussen, and C.E. Thomas. Pellet fuelling, ELM pacing and disruption mitigation technology development for ITER. *Nuclear Fusion*, 49(8):085013, jul 2009. doi: 10.1088/0029-5515/49/8/085013. URL https://doi.org/10.1088%2F0029-5515%2F49%2F8%2F085013.

[42] D.K. Mansfield, A.L. Roquemore, T. Carroll, Z. Sun, J.S. Hu, L. Zhang, Y.F. Liang, X.Z. Gong, J.G. Li, H.Y. Guo, G.Z. Zuo, P. Parks, W. Wu, and R. Maingi. First observations of ELM triggering by injected lithium granules in EAST. *Nuclear Fusion*, 53(11):113023, sep 2013. doi: 10.1088/0029-5515/53/11/113023. URL https://doi.org/10.1088%2F0029-5515%2F53%2F11%2F113023.

[43] Todd E. Evans, Richard A. Moyer, Keith H. Burrell, Max E. Fenstermacher, Ilon Joseph, Anthony W. Leonard, Thomas H. Osborne, Gary D. Porter, Michael J. Schaffer, Philip B. Snyder, Paul R. Thomas, Jonathan G. Watkins, and William P. West. Edge stability and transport control with resonant magnetic perturbations in collisionless tokamak plasmas. *Nature Physics*, 2(6):419–423, 2006. doi: 10.1038/nphys312. URL https://doi.org/10.1038/nphys312.

[44] A Kirk, I T Chapman, J Harrison, Yueqiang Liu, E Nardon, S Saarelma, R Scannell, and A J Thornton and. Effect of resonant magnetic perturbations with toroidal mode numbers of 4 and 6 on edge-localized modes in single null h-mode plasmas in MAST. *Plasma Physics and Controlled Fusion*, 55(1):015006, dec 2012. doi: 10.1088/0741-3335/55/1/015006. URL https://doi.org/10.1088%2F0741-3335%2F55%2F1%2F015006.

[45] Y. Liang, P. Lomas, I. Nunes, M. Gryaznevich, M.N.A. Beurskens, S. Brezinsek, J.W. Coenen, P. Denner, Th. Eich, L. Frassinetti, S. Gerasimov,

D. Harting, S. Jachmich, A. Meigs, J. Pearson, M. Rack, S. Saarelma, B. Sieglin, Y. Yang, and L. Zeng and. Mitigation of type-i ELMs withn= 2 fields on JET with ITER-like wall. *Nuclear Fusion*, 53(7):073036, jun 2013. doi: 10.1088/0029-5515/53/7/073036. URL https://doi.org/10.1088%2F0029-5515%2F53%2F7%2F073036.

[46] W. Suttrop, T. Eich, J. C. Fuchs, S. Günter, A. Janzer, A. Herrmann, A. Kallenbach, P. T. Lang, T. Lunt, M. Maraschek, R. M. McDermott, A. Mlynek, T. Pütterich, M. Rott, T. Vierle, E. Wolfrum, Q. Yu, I. Zammuto, and H. Zohm. First observation of edge localized modes mitigation with resonant and nonresonant magnetic perturbations in asdex upgrade. *Phys. Rev. Lett.*, 106:225004, Jun 2011. doi: 10.1103/PhysRevLett.106.225004. URL https://link.aps.org/doi/10.1103/PhysRevLett.106.225004.

[47] T.E. Evans, M.E. Fenstermacher, R.A. Moyer, T.H. Osborne, J.G. Watkins, P. Gohil, I. Joseph, M.J. Schaffer, L.R. Baylor, M. Bécoulet, J.A. Boedo, K.H. Burrell, J.S. deGrassie, K.H. Finken, T. Jernigan, M.W. Jakubowski, C.J. Lasnier, M. Lehnen, A.W. Leonard, J. Lonnroth, E. Nardon, V. Parail, O. Schmitz, B. Unterberg, and W.P. West. RMP ELM suppression in DIII-d plasmas with ITER similar shapes and collisionalities. *Nuclear Fusion*, 48 (2):024002, jan 2008. doi: 10.1088/0029-5515/48/2/024002. URL https://doi.org/10.1088%2F0029-5515%2F48%2F2%2F024002.

[48] Y. Sun, Y. Liang, Y. Q. Liu, S. Gu, X. Yang, W. Guo, T. Shi, M. Jia, L. Wang, B. Lyu, C. Zhou, A. Liu, Q. Zang, H. Liu, N. Chu, H. H. Wang, T. Zhang, J. Qian, L. Xu, K. He, D. Chen, B. Shen, X. Gong, X. Ji, S. Wang, M. Qi, Y. Song, Q. Yuan, Z. Sheng, G. Gao, P. Fu, and B. Wan. Nonlinear transition from mitigation to suppression of the edge localized mode with resonant magnetic perturbations in the east tokamak. *Phys. Rev. Lett.*, 117: 115001, Sep 2016. doi: 10.1103/PhysRevLett.117.115001. URL https://link.aps.org/doi/10.1103/PhysRevLett.117.115001.

[49] Y. M. Jeon, J.-K. Park, S. W. Yoon, W. H. Ko, S. G. Lee, K. D. Lee, G. S. Yun, Y. U. Nam, W. C. Kim, Jong-Gu Kwak, K. S. Lee, H. K. Kim, and H. L. Yang. Suppression of edge localized modes in high-confinement kstar plasmas by nonaxisymmetric magnetic perturbations. *Phys. Rev. Lett.*, 109:035004, Jul 2012. doi: 10.1103/PhysRevLett.109.035004. URL https://link.aps.org/doi/10.1103/PhysRevLett.109.035004.

[50] W. Suttrop, A. Kirk, V. Bobkov, M. Cavedon, M. Dunne, R.M. McDermott, H. Meyer, R. Nazikian, C. Paz-Soldan, D.A. Ryan, E. Viezzer, M. Willensdorfer, and and. Experimental conditions to suppress edge localised modes by magnetic perturbations in the ASDEX upgrade tokamak. *Nuclear Fusion*, 58(9):096031, jul 2018. doi: 10.1088/1741-4326/aace93. URL https://doi.org/10.1088%2F1741-4326%2Faace93.

[51] J.M. Canik, A.C. Sontag, R. Maingi, R. Bell, D.A. Gates, S.P. Gerhardt, H.W. Kugel, B.P. LeBlanc, J. Menard, S. Paul, S. Sabbagh, and V.A. Soukhanovskii. Progress in the development of ELM pace-making with non-axisymmetric magnetic perturbations in NSTX. *Nuclear Fusion*, 50(6): 064016, may 2010. doi: 10.1088/0029-5515/50/6/064016. URL https://doi.org/10.1088%2F0029-5515%2F50%2F6%2F064016.

[52] T.E. Evans, R.A. Moyer, J.G. Watkins, P.R. Thomas, T.H. Osborne, J.A. Boedo, M.E. Fenstermacher, K.H. Finken, R.J. Groebner, M. Groth, J. Harris, G.L. Jackson, R.J. La Haye, C.J. Lasnier, M.J. Schaffer, G. Wang, and L. Zeng. Suppression of large edge localized modes in high confinement diii-d plasmas with a stochastic magnetic boundary. *Journal of Nuclear Materials*, 337-339:691 – 696, 2005. ISSN 0022-3115. doi: https://doi.org/10.1016/j.jnucmat.2004.10.062. URL http://www.sciencedirect.com/science/article/pii/S0022311504008323. PSI-16.

[53] C. Paz-Soldan, R. Nazikian, L. Cui, B.C. Lyons, D.M. Orlov, A. Kirk, N.C. Logan, T.H. Osborne, W. Suttrop, and D.B. Weisberg. The effect of plasma shape and neutral beam mix on the rotation threshold for RMP-ELM suppression. *Nuclear Fusion*, 59(5):056012, mar 2019. doi: 10.1088/1741-4326/ab04c0. URL https://doi.org/10.1088%2F1741-4326%2Fab04c0.

[54] A. Kirk, E. Nardon, R. Akers, M. Bécoulet, G. De Temmerman, B. Dudson, B. Hnat, Y.Q. Liu, R. Martin, P. Tamain, and D. Taylor and. Resonant magnetic perturbation experiments on MAST using external and internal coils for ELM control. *Nuclear Fusion*, 50(3):034008, feb 2010. doi: 10.1088/0029-5515/50/3/034008. URL https://doi.org/10.1088%2F0029-5515%2F50%2F3%2F034008.

[55] Yunfeng LIANG, Hans-Rudolf KOSLOWSKI, Stefan JACHMICH, Alberto ALFIER, Christopher G. GIMBLETT, Eric NARDON, Philippa K. BROWNING, Peter DEVOY, Thomas EICH, Carine GIROUD, Geoffrey MADDISON, Peter T. LANG, Mikhail P. GRYAZNEVICH, Derek HARTING, Martin HEYN, Samuli SAARELMA, Youwen SUN, Ronald WENNINGER, Christopher WIEGMANN, Tao ZHANG, and JET-EFDA Contributors. Overview of elm control by low n magnetic perturbations on jet. *Plasma and Fusion Research*, 5:S2018–S2018, 2010. doi: 10.1585/pfr.5.S2018.

[56] W. Zhu, S. A. Sabbagh, R. E. Bell, J. M. Bialek, M. G. Bell, B. P. LeBlanc, S. M. Kaye, F. M. Levinton, J. E. Menard, K. C. Shaing, A. C. Sontag, and H. Yuh. Observation of plasma toroidal-momentum dissipation by neoclassical toroidal viscosity. *Phys. Rev. Lett.*, 96:225002, Jun 2006. doi: 10.1103/PhysRevLett.96.225002. URL https://link.aps.org/doi/10.1103/PhysRevLett.96.225002.

[57] A. M. Garofalo, K. H. Burrell, J. C. DeBoo, J. S. deGrassie, G. L. Jackson, M. Lanctot, H. Reimerdes, M. J. Schaffer, W. M. Solomon, and E. J. Strait. Observation of plasma rotation driven by static nonaxisymmetric magnetic fields in a tokamak. *Phys. Rev. Lett.*, 101:195005, Nov 2008. doi: 10.1103/PhysRevLett.101.195005. URL https://link.aps.org/doi/10.1103/PhysRevLett.101.195005.

[58] V. Igochine. Physics of resistive wall modes. *Nuclear Fusion*, 52(7):074010, jul 2012. doi: 10.1088/0029-5515/52/7/074010. URL https://doi.org/10.1088%2F0029-5515%2F52%2F7%2F074010.

[59] R J Buttery, S Günter, G Giruzzi, T C Hender, D Howell, G Huysmans, R J La Haye, M Maraschek, H Reimerdes, O Sauter, C D Warrick, H R Wilson, and H Zohm. Neoclassical tearing modes. *Plasma Physics and Controlled Fusion*, 42(12B):B61–B73, dec 2000. doi: 10.1088/0741-3335/42/12b/306. URL https://doi.org/10.1088%2F0741-3335%2F42%2F12b%2F306.

[60] V.A. Izzo and I. Joseph. RMP enhanced transport and rotational screening in simulations of DIII-d plasmas. *Nuclear Fusion*, 48(11):115004, sep 2008. doi: 10.1088/0029-5515/48/11/115004. URL https://doi.org/10.1088%2F0029-5515%2F48%2F11%2F115004.

[61] R. Hager, N. Ferraro, C.-S. Chang, and R. Nazikian. Understanding the RMP and density pump-out physics from a coupled gyrokinetic-MHD simulation. In *APS Meeting Abstracts*, page NP11.067, 2018.

[62] S.X. Wang, H.Q. Liu, Y.X. Jie, W.X. Ding, L. Zeng, Y.W. Sun, H. Lian, X. Zhu, Z.Y. Zou, B. Lyu, Y.Y. Li, Q. Zang, H.F. Du, C. Zhou, A.D. Liu, T. Zhang, W. Gao, and X. Gao and. Investigation of RMP induced density pump-out on EAST. *Nuclear Fusion*, 58(11):112013, oct 2018. doi: 10.1088/1741-4326/aae15a. URL https://doi.org/10.1088%2F1741-4326%2Faae15a.

[63] G.R. McKee, Z. Yan, C. Holland, R.J. Buttery, T.E. Evans, R.A. Moyer, S. Mordijck, R. Nazikian, T.L. Rhodes, O. Schmitz, and M.R. Wade. Increase of turbulence and transport with resonant magnetic perturbations in ELM-suppressed plasmas on DIII-d. *Nuclear Fusion*, 53(11):113011, sep 2013. doi: 10.1088/0029-5515/53/11/113011. URL https://doi.org/10.1088%2F0029-5515%2F53%2F11%2F113011.

[64] Jaehyun Lee, Gunsu S. Yun, Minjun J. Choi, Jae-Min Kwon, Young-Mu Jeon, Woochang Lee, Neville C. Luhmann, and Hyeon K. Park. Nonlinear interaction of edge-localized modes and turbulent eddies in toroidal plasma under $n = 1$ magnetic perturbation. *Phys. Rev. Lett.*, 117:075001, Aug 2016. doi: 10.1103/PhysRevLett.117.075001. URL https://link.aps.org/doi/10.1103/PhysRevLett.117.075001.

[65] J.L Luxon, M.J Schaffer, G.L Jackson, J.A Leuer, A Nagy, J.T Scoville, and E.J Strait. Anomalies in the applied magnetic fields in DIII-d and their implications for the understanding of stability experiments. *Nuclear Fusion*, 43(12):1813–1828, dec 2003. doi: 10.1088/0029-5515/43/12/024. URL https://doi.org/10.1088%2F0029-5515%2F43%2F12%2F024.

[66] F.L. Waelbroeck. Theory and observations of magnetic islands. *Nuclear Fusion*, 49(10):104025, sep 2009. doi: 10.1088/0029-5515/49/10/104025. URL https://doi.org/10.1088%2F0029-5515%2F49%2F10%2F104025.

[67] Richard Fitzpatrick. Nonlinear neoclassical two-fluid theory of response of tokamak plasma to resonant error-field. *Physics of Plasmas*, 25(8):

082513, 2018. doi: 10.1063/1.5043203. URL https://doi.org/10.1063/1.5043203.

[68] Richard Fitzpatrick. Two-fluid nonlinear theory of response of tokamak plasma to resonant magnetic perturbation. *Physics of Plasmas*, 25(11): 112505, 2018. doi: 10.1063/1.5053804. URL https://doi.org/10.1063/1.5053804.

[69] C. C. Hegna and S. R. Hudson. Loss of second-ballooning stability in three-dimensional equilibria. *Phys. Rev. Lett.*, 87:035001, Jun 2001. doi: 10.1103/PhysRevLett.87.035001. URL https://link.aps.org/doi/10.1103/PhysRevLett.87.035001.

[70] M. Willensdorfer, T. B. Cote, C. C. Hegna, W. Suttrop, H. Zohm, M. Dunne, E. Strumberger, G. Birkenmeier, S. S. Denk, F. Mink, B. Vanovac, and L. C. Luhmann. Field-line localized destabilization of ballooning modes in three-dimensional tokamaks. *Phys. Rev. Lett.*, 119: 085002, Aug 2017. doi: 10.1103/PhysRevLett.119.085002. URL https://link.aps.org/doi/10.1103/PhysRevLett.119.085002.

[71] T.B. Cote, C.C. Hegna, M. Willensdorfer, E. Strumberger, W. Suttrop, and H. Zohm and. Helically localized ballooning instabilities in three-dimensional tokamak pedestals. *Nuclear Fusion*, 59(1):016015, dec 2018. doi: 10.1088/1741-4326/aaf01d. URL https://doi.org/10.1088%2F1741-4326%2Faaf01d.

[72] M. Bécoulet, F. Orain, G. T. A. Huijsmans, S. Pamela, P. Cahyna, M. Hoelzl, X. Garbet, E. Franck, E. Sonnendrücker, G. Dif-Pradalier, C. Passeron, G. Latu, J. Morales, E. Nardon, A. Fil, B. Nkonga, A. Ratnani, and V. Grandgirard. Mechanism of edge localized mode mitigation by resonant magnetic perturbations. *Phys. Rev. Lett.*, 113:115001, Sep 2014. doi: 10.1103/PhysRevLett.113.115001. URL https://link.aps.org/doi/10.1103/PhysRevLett.113.115001.

[73] F. Orain, M. Hoelzl, F. Mink, M. Willensdorfer, M. Bécoulet, M. Dunne, S. Günter, G. Huijsmans, K. Lackner, S. Pamela, W. Suttrop, and E. Viezzer. Non-linear modeling of the threshold between elm mitigation and elm suppression by resonant magnetic perturbations in asdex upgrade. *Physics of Plasmas*, 26(4):042503, 2019. doi: 10.1063/1.5091843. URL https://doi.org/10.1063/1.5091843.

[74] S K Kim, S. Pamela, O Kwon, Marina Becoulet, G Hujismans, Y In, M Hoelzl, J H Lee, M Kim, G Y Park, H S Kim, Y H Lee, G J Choi, C Y Lee, and Y.-S Na. Nonlinear Modeling of the Effect of n=2 Resonant Magnetic Field Perturbation on Peeling-Ballooning Mode in KSTAR. working paper or preprint, July 2019. URL https://hal.archives-ouvertes.fr/hal-02184637.

[75] D. Chandra, A. Thyagaraja, A. Sen, and P. Kaw. Nonlinear simulation of ELM dynamics in the presence of resonant magnetic perturbations. *Nuclear Fusion*, 57(7):076001, may 2017. doi: 10.1088/1741-4326/aa6dca. URL https://doi.org/10.1088%2F1741-4326%2Faa6dca.

[76] C. C. Hegna. Effects of a weakly 3-d equilibrium on ideal magnetohydrodynamic instabilities. *Physics of Plasmas*, 21(7):072502, 2014. doi: 10.1063/1.4887008. URL https://doi.org/10.1063/1.4887008.

[77] David Anthony Ryan, Mike G Dunne, Andrew Kirk, Samuli Saarelma, Wolfgang Suttrop, Christopher J Ham, Yueqiang Liu, and Matthias Willensdorfer. Numerical survey of predicted peeling response in elm mitigated and suppressed phases on asdex upgrade. *Plasma Physics and Controlled Fusion*, 2019. URL http://iopscience.iop.org/10.1088/1361-6587/ab32fa.

[78] D.V. Anderson, W.A. Cooper, R. Gruber, S. Merazzi, and U. Schwenn. Methods for the efficient calculation of the (mhd) magnetohydrodynamic stability properties of magnetically confined fusion plasmas. *The International Journal of Supercomputing Applications*, 4(3):34–47, 1990. doi: 10.1177/109434209000400305. URL https://doi.org/10.1177/109434209000400305.

[79] Carolin Nührenberg. Global ideal magnetohydrodynamic stability analysis for the configurational space of wendelstein 7–x. *Physics of Plasmas*, 3(6):2401–2410, 1996. doi: 10.1063/1.871924. URL https://doi.org/10.1063/1.871924.

[80] E. Strumberger and S. Günter. CASTOR3d: linear stability studies for 2d and 3d tokamak equilibria. *Nuclear Fusion*, 57(1):016032, nov 2016. doi: 10.1088/0029-5515/57/1/016032. URL https://doi.org/10.1088%2F0029-5515%2F57%2F1%2F016032.

[81] T. Weyens, R. Sánchez, G. Huijsmans, A. Loarte, and L. García. Pb3d: A new code for edge 3-d ideal linear peeling-ballooning stability. *Journal of Computational Physics*, 330:997 – 1009, 2017. ISSN 0021-9991. doi: https://doi.org/10.1016/j.jcp.2016.10.054. URL http://www.sciencedirect.com/science/article/pii/S0021999116305629.

[82] H. R. Wilson, P. B. Snyder, G. T. A. Huysmans, and R. L. Miller. Numerical studies of edge localized instabilities in tokamaks. *Physics of Plasmas*, 9(4): 1277–1286, 2002. doi: 10.1063/1.1459058. URL https://doi.org/10.1063/1.1459058.

[83] A. E. Lunniss. Modelling eruptions and edge stability in tokamak plasmas. *University of York*, PhD Thesis, 2016. URL http://etheses.whiterose.ac.uk/id/eprint/16638.

[84] B.D. Dudson, M.V. Umansky, X.Q. Xu, P.B. Snyder, and H.R. Wilson. Bout++: A framework for parallel plasma fluid simulations. *Computer Physics Communications*, 180(9):1467 – 1480, 2009. ISSN 0010-4655. doi: https://doi.org/10.1016/j.cpc.2009.03.008. URL http://www.sciencedirect.com/science/article/pii/S0010465509001040.

[85] Yueqiang Liu, A. Kirk, and E. Nardon. Full toroidal plasma response to externally applied nonaxisymmetric magnetic fields. *Physics of Plasmas*, 17(12):122502, 2010. doi: 10.1063/1.3526677. URL https://doi.org/10.1063/1.3526677.

[86] J. Hajdu. R. balescu: Equilibrium and nonequilibrium statistical mechanics. john wiley & sons, chichester, new york, sydney, toronto 1975, 742 seiten, preis: £ 16.20. *Berichte der Bunsengesellschaft für physikalische Chemie*, 81(2):240–241, 1977. doi: 10.1002/bbpc.19770810244. URL https://onlinelibrary.wiley.com/doi/abs/10.1002/bbpc.19770810244.

[87] D. Biskamp. Nonlinear Magnetohydrodynamics. *Cambridge Monographs on Plasma Physics*, 1997. doi: www.cambridge.org/9780521599184. URL https://www.cambridge.org/gb/academic/subjects/physics/astrophysics/nonlinear-magnetohydrodynamics?format=PB&isbn=9780521599184.

[88] Z. Li and D. Livescu. High-order two-fluid plasma solver for direct numerical simulations of plasma flows with full transport phenomena. *Physics of Plasmas*, 26(1):012109, 2019. doi: 10.1063/1.5082190. URL https://doi.org/10.1063/1.5082190.

[89] J. P. Hans Goedbloed and Stefaan Poedts. *Principles of Magnetohydrodynamics: With Applications to Laboratory and Astrophysical Plasmas*. Cambridge University Press, 2004. doi: 10.1017/CBO9780511616945.

[90] I. B. Bernstein, E. A. Frieman, Martin David Kruskal, R. M. Kulsrud, and Subrahmanyan Chandrasekhar. An energy principle for hydromagnetic stability problems. *Proceedings of the Royal Society of London. Series A. Mathematical and Physical Sciences*, 244(1236):17–40, 1958. doi: 10.1098/rspa.1958.0023. URL https://royalsocietypublishing.org/doi/abs/10.1098/rspa.1958.0023.

[91] A. H. Glasser, J. M. Greene, and J. L. Johnson. Resistive instabilities in a tokamak. *The Physics of Fluids*, 19(4):567–574, 1976. doi: 10.1063/1.861490. URL https://aip.scitation.org/doi/abs/10.1063/1.861490.

[92] C. C. Hegna and S. R. Hudson. Ideal magnetohydrodynamic ballooning stability boundaries in three-dimensional equilibria. *Physics of Plasmas*, 9 (5):2014–2019, 2002. doi: 10.1063/1.1446037. URL https://doi.org/10.1063/1.1446037.

[93] J. W. Connor, R. J. Hastie, and J. B. Taylor. Shear, periodicity, and plasma ballooning modes. *Phys. Rev. Lett.*, 40:396–399, Feb 1978. doi: 10.1103/PhysRevLett.40.396. URL https://link.aps.org/doi/10.1103/PhysRevLett.40.396.

[94] J.P. Freidberg. Ideal MHD. *Cambridge University Press*, 2014. doi: www.cambridge.org/9781107006256. URL https://www.cambridge.org/gb/academic/subjects/physics/plasma-physics-and-fusion-physics/ideal-mhd?format=HB&isbn=9781107006256.

[95] R. L. Dewar and A. H. Glasser. Ballooning mode spectrum in general toroidal systems. *The Physics of Fluids*, 26(10):3038–3052, 1983. doi: 10.

1063/1.864028. URL https://aip.scitation.org/doi/abs/10.1063/1.864028.

[96] O. A. Hurricane, B. D. G. Chandran, and S. C. Cowley. Internal kink stability of large aspect ratio tokamaks. *Physics of Plasmas*, 7 (10):4043–4051, 2000. doi: 10.1063/1.1288489. URL https://aip.scitation.org/doi/abs/10.1063/1.1288489.

[97] T H Osborne, J R Ferron, R J Groebner, L L Lao, A W Leonard, M A Mahdavi, R Maingi, R L Miller, A D Turnbull, M Wade, and J Watkins. The effect of plasma shape on h-mode pedestal characteristics on DIII-d. *Plasma Physics and Controlled Fusion*, 42(5A):A175–A184, may 2000. doi: 10.1088/0741-3335/42/5a/319. URL https://doi.org/10.1088%2F0741-3335%2F42%2F5a%2F319.

[98] D A Mossessian, P B Snyder, M Greenwald, J W Hughes, Y Lin, A Mazurenko, S Medvedev, H R Wilson, and S Wolfe. H-mode pedestal characteristics and MHD stability of the edge plasma in alcator c-mod. *Plasma Physics and Controlled Fusion*, 44(4):423–437, mar 2002. doi: 10.1088/0741-3335/44/4/303. URL https://doi.org/10.1088%2F0741-3335%2F44%2F4%2F303.

[99] C. Perez von Thun, L. Frassinetti, L. Horvath, S. Saarelma, L. Meneses, E. de la Luna, M. Beurskens, J. Boom, J. Flanagan, J.C. Hillesheim, C.F. Maggi, S.J.P. Pamela, and E.R. Solano and. Long-lived coupled peeling ballooning modes preceding ELMs on JET. *Nuclear Fusion*, 59(5):056004, mar 2019. doi: 10.1088/1741-4326/ab0031. URL https://doi.org/10.1088%2F1741-4326%2Fab0031.

[100] P.B. Snyder, N. Aiba, M. Beurskens, R.J. Groebner, L.D. Horton, A.E. Hubbard, J.W. Hughes, G.T.A. Huysmans, Y. Kamada, A. Kirk, C. Konz, A.W. Leonard, J. Lönnroth, C.F. Maggi, R. Maingi, T.H. Osborne, N. Oyama, A. Pankin, S. Saarelma, G. Saibene, J.L. Terry, H. Urano, and H.R. Wilson. Pedestal stability comparison and ITER pedestal prediction. *Nuclear Fusion*, 49(8):085035, jul 2009. doi: 10.1088/0029-5515/49/8/085035. URL https://doi.org/10.1088%2F0029-5515%2F49%2F8%2F085035.

[101] P. B. Snyder, R. J. Groebner, A. W. Leonard, T. H. Osborne, and H. R. Wilson. Development and validation of a predictive model for the

pedestal height. *Physics of Plasmas*, 16(5):056118, 2009. doi: 10.1063/1.3122146. URL https://doi.org/10.1063/1.3122146.

[102] P.B. Snyder, R.J. Groebner, J.W. Hughes, T.H. Osborne, M. Beurskens, A.W. Leonard, H.R. Wilson, and X.Q. Xu. A first-principles predictive model of the pedestal height and width: development, testing and ITER optimization with the EPED model. *Nuclear Fusion*, 51(10):103016, aug 2011. doi: 10.1088/0029-5515/51/10/103016. URL https://doi.org/10.1088%2F0029-5515%2F51%2F10%2F103016.

[103] T. Weyens, R. Sánchez, L. García, A. Loarte, and G. Huijsmans. Three-dimensional linear peeling-ballooning theory in magnetic fusion devices. *Physics of Plasmas*, 21(4):042507, 2014. doi: 10.1063/1.4871859. URL https://doi.org/10.1063/1.4871859.

[104] R. L. Miller, M. S. Chu, J. M. Greene, Y. R. Lin-Liu, and R. E. Waltz. Noncircular, finite aspect ratio, local equilibrium model. *Physics of Plasmas*, 5(4):973–978, 1998. doi: 10.1063/1.872666. URL https://doi.org/10.1063/1.872666.

[105] Carolin Schwab. Ideal magnetohydrodynamics: Global mode analysis of three-dimensional plasma configurations. *Physics of Fluids B: Plasma Physics*, 5(9):3195–3206, 1993. doi: 10.1063/1.860656. URL https://doi.org/10.1063/1.860656.

[106] P. Helander and S. L. Newton. Ideal magnetohydrodynamic stability of configurations without nested flux surfaces. *Physics of Plasmas*, 20(6):062504, 2013. doi: 10.1063/1.4812194. URL https://doi.org/10.1063/1.4812194.

[107] Allen H. Boozer and Carolin Nührenberg. Perturbed plasma equilibria. *Physics of Plasmas*, 13(10):102501, 2006. doi: 10.1063/1.2353903. URL https://doi.org/10.1063/1.2353903.

[108] Per Helander. Theory of plasma confinement in non-axisymmetric magnetic fields. *Reports on Progress in Physics*, 77(8):087001, jul 2014. doi: 10.1088/0034-4885/77/8/087001. URL https://doi.org/10.1088%2F0034-4885%2F77%2F8%2F087001.

[109] S.P. Hirshman, W.I. van RIJ, and P. Merkel. Three-dimensional free boundary calculations using a spectral green's function method.

Computer Physics Communications, 43(1):143 – 155, 1986. ISSN 0010-4655. doi: https://doi.org/10.1016/0010-4655(86)90058-5. URL http://www.sciencedirect.com/science/article/pii/0010465586900585.

[110] Jong-kyu Park, Allen H. Boozer, and Alan H. Glasser. Computation of three-dimensional tokamak and spherical torus equilibria. *Physics of Plasmas*, 14(5):052110, 2007. doi: 10.1063/1.2732170. URL https://doi.org/10.1063/1.2732170.

[111] J. Loizu, S. R. Hudson, A. Bhattacharjee, S. Lazerson, and P. Helander. Existence of three-dimensional ideal-magnetohydrodynamic equilibria with current sheets. *Physics of Plasmas*, 22(9):090704, 2015. doi: 10.1063/1.4931094. URL https://doi.org/10.1063/1.4931094.

[112] Samuel A. Lazerson, Joaquim Loizu, Steven Hirshman, and Stuart R. Hudson. Verification of the ideal magnetohydrodynamic response at rational surfaces in the vmec code. *Physics of Plasmas*, 23(1):012507, 2016. doi: 10.1063/1.4939881. URL https://doi.org/10.1063/1.4939881.

[113] J. Loizu, S. R. Hudson, P. Helander, S. A. Lazerson, and A. Bhattacharjee. Pressure-driven amplification and penetration of resonant magnetic perturbations. *Physics of Plasmas*, 23(5):055703, 2016. doi: 10.1063/1.4944818. URL https://doi.org/10.1063/1.4944818.

[114] Dmitry A. Maslovsky and Allen H. Boozer. Effective plasma inductance computation. *Physics of Plasmas*, 12(4):042108, 2005. doi: 10.1063/1.1877516. URL https://doi.org/10.1063/1.1877516.

[115] Yueqiang Liu, A Kirk, and A J Thornton and. Modelling intrinsic error field correction experiments in MAST. *Plasma Physics and Controlled Fusion*, 56(10):104002, aug 2014. doi: 10.1088/0741-3335/56/10/104002. URL https://doi.org/10.1088%2F0741-3335%2F56%2F10%2F104002.

[116] E. Nardon, M. Bécoulet, G. Huysmans, O. Czarny, P.R. Thomas, M. Lipa, R.A. Moyer, T.E. Evans, G. Federici, Y. Gribov, A. Polevoi, G. Saibene, A. Portone, and A. Loarte. Edge localized modes control by resonant magnetic perturbations. *Journal of Nuclear Materials*, 363-365:1071 – 1075,

2007. ISSN 0022-3115. doi: https://doi.org/10.1016/j.jnucmat.2007.01.189. URL http://www.sciencedirect.com/science/article/pii/S0022311507002188. Plasma-Surface Interactions-17.

[117] A. D. Turnbull, N. M. Ferraro, V. A. Izzo, E. A. Lazarus, J.-K. Park, W. A. Cooper, S. P. Hirshman, L. L. Lao, M. J. Lanctot, S. Lazerson, Y. Q. Liu, A. Reiman, and F. Turco. Comparisons of linear and nonlinear plasma response models for non-axisymmetric perturbations. *Physics of Plasmas*, 20(5):056114, 2013. doi: 10.1063/1.4805087. URL https://doi.org/10.1063/1.4805087.

[118] M Willensdorfer, T B Cote, M Griener, D A Ryan, E Strumberger, W Suttrop, N Wang, M Cavedon, S S Denk, M Dunne, R Fischer, J Galdon-Quiroga, C J Ham, C C Hegna, M Hoelzl, A Kirk, M Maraschek, F Mink, N Leuthold, F Orain, E P Seliunin, H Zohm, and and. Dynamics of ideal modes and subsequent ELM crashes in 3d tokamak geometry from external magnetic perturbations. *Plasma Physics and Controlled Fusion*, 61(1):014019, nov 2018. doi: 10.1088/1361-6587/aadc39. URL https://doi.org/10.1088%2F1361-6587%2Faadc39.

[119] A. H. Glasser and M. S. Chance. Determination of Free Boundary Ideal MHD Stability with DCON and VACUUM. In *APS Meeting Abstracts*, page dMopP102, November 1997.